Universidade de Aveiro
Departamento de
Eletrónica, Telecomunicações e Informática
2014

Helder Vasconcelos
Graça Reis

ANTENA INTELIGENTE PARA APLICAÇÕES RFID

SMART ANTENNA FOR RFID APPLICATIONS

Helder Vasconcelos
Graça Reis

ANTENA INTELIGENTE PARA APLICAÇÕES RFID

SMART ANTENNA FOR RFID APPLICATIONS

Dissertação apresentada à Universidade de Aveiro para cumprimento dos requesitos necessários à obtenção do grau de Mestre em Engenharia Electrónica e Telecomunicaçoes, realizada sob a orientação científica do Professor Doutor João Nuno Pimentel da Silva Matos (orientador), Professor do Departamento de Electrónica, Telecomunicações e Informática da Universidade de Aveiro e do Professor Doutor Arnaldo Silva Rodrigues de Oliveira (co-orientador), Professor do Departamento de Electrónica, Telecomunicações e Informática da Universidade de Aveiro

o júri / the jury

presidente / president

Prof. Doutor Armando Carlos Domingues da Rocha

Professor Auxiliar da Universidade de Aveiro

vogais / examiners committee

Prof. Doutor João Nuno Pimentel da Silva Matos

Professor Associado da Universidade de Aveiro (orientador)

Prof. Doutor Pedro Renato Tavares de Pinho

Professor Adjunto da Área Departamental de Engenharia de Eletrónica e Telecomunicações e de Computadores do Instituto Superior de Engenharia de Lisboa

agradecimentos / acknowledgements

Um agradecimento aos meus pais, avós e restante família pelo suporte incondicionável que me têm dado ao longo do meu percurso académico, que só com apoio deles consegui reunir forças para chegar até aqui.

Um agradecimento sentido a todos os meus colegas, por todos os momentos de alegria passados, pelo apoio e verdadeira amizade que não deixei de sentir ao longo de todo este percurso. Aos meus orientadores, professor João Nuno Matos e professor Arnaldo Oliveira, pelo constante apoio e disponibilidade prestados no decorrer desta dissertação.

Gostaria ainda de agrader ao Instituto de Telecomunicações pelo apoio prestado durante o desenvolvimento desta dissertação, assim como a todos que de algum modo me suportaram e ajudaram a atingir esta etapa determinante da minha vida.

Palavras-chave RFID, Antena microstrip, agregagdo de antenas , Direcionamento de feixe, DOA, Formação de lóbulos, Directividade, UHF

Resumo

A adoção e proliferação de sistemas de informaçao em várias indústrias e atividades pessoais são responsáveis pela crescente necessidade de identifcar e rastrear itens e serviços. Sistemas de identificação por rádiofrequência (RFID) foram desenvolvidos de modo a responder às crescentes necessidades tanto de particulares como de empresas quanto à utilização de sistemas de identificaçao e de transmissão de dados sem fios, permitindo a redução de despesas e o aumento de receitas a várias empresas.

De modo a melhorar a eficiência de empresas a uma escala global, sistemas de antenas inteligentes foram introduzidos nas suas linhas de manufatura e de prestação de serviços como um componente central, abrirando o caminho para esquemas de comunicação sem fios inovadores e robustos, baseados em RFID, facultando processos de captura e processamento de sinal avançados capazes de fornecer melhorias em aplicações de rastreamento e automação de processos. Antenas inteligentes podem ser instaladas em leitores RFID, permitindo um melhor processamento de sinais transmitidos pelas etiquetas, dando origem a um método de identificação mais eficiente. A arquitectura de leitores RFID com uma rede de antenas inteligentes embutida garante melhorias na taxa de transferência e na rapidez de leitura de informação assim como na deteção de itens etiquetados.

Um circuito baseado em sistemas de antenas inteligentes é proposto neste trabalho para localização assistida dispositivos RFID e para direccionamento de feixe através da utilizaçao de um agregado linear e uniforme de antenas *microstrip* diretivas. Várias técnicas de direcionamento de feixe e de estimativa de angulo de chegada foram utilizados, de modo a analisar o desempenho e a resolução de cada algoritmo de acordo com a carga computacional, modulação utilizada e o ambiente em que o sistema de antenas inteligentes poderá ser implementado.

Key words RFID, Microstrip antenna, Antenna array, Beam steering, DOA, beamforming, Directivity, UHF

Abstract The adoption and proliferation of information systems in many business and personal activities leads to the need of tagging and tracking items and services. Radio frequency identification (RFID) systems were developed as an effort to answer the increasing needs of particulars and enterprises alike for wireless identification of objects and data exchange services, enabling a large number of businesses to reduce costs and increase revenue.

As to further develop the efficiency provided by businesses worldwide, smart antenna systems were introduced as core component in their production and service providing lines, opening the path for innovative and robust wireless RFID based communication schemes, providing advanced signal capturing, processing characteristics and enhanced tracking and process automation. Smart antennas can be installed within RFID readers, enabling them to more efficiently process returned echoes by the tags and therefore improving the identification mechanism. RFID reader architectures with an embedded smart antenna network reliably improve the throughput, the reading speed and position detection of tagged items.

A smart antenna based circuit is proposed here for RFID assisted localization and for beam steering applications using a uniform linear array of microstrip directional antennas. Several beamforming and direction of arrival estimation methods were employed in order to analyze their performance and resolution based on the computational load, modulation, and the overall environment in which the smart anetnna system may be deployed.

Contents

List of Figures

List of Tables

List of Acronyms

ASIC	Application-Specific Integrated Circuits
CM	Constant Modulus
CSI	Channel State Information
DOA	Direction of Arrival
EIRP	Isotropically Radiated Pwer
EPC	Electronic Product Code
ESPRIT	Estimation of Signal Parameters Via Rotational Invariance Techniques
FM	Frequency Modulation
FNBW	First-Null Beamwidth
FPGA	Field programmable gate arrays
FSK	Frequency-shift Keying
HPBW	Half-Power Beamwidth
LMS	Least Mean-Square
LSCM	Least Sqaure Constant Modulus
MUSIC	Multiple Signal Classification
PSK	Phase-shift Keying
QAM	Quandrature Amplitude Modulation
RFID	Radio Frequency Identification
SIR	Signal to Noise Ratio
SNOI	Signal Not of Interest
SOI	Signal of Interest
UHF	Ultra High Frequency
ULA	Uniform Linear Array

Chapter 1

Introduction

1.1 Motivations and Objectives

Over the last years wireless communication systems have become one of the most active areas of technology development, constantly changing and adapting to the needs of particulars and enterprises alike. As the demand for consumables and services rises, industries try to keep an efficient and an economically viable environment in order to hold a competitive edge. Identification is a powerful capability, essential to many aspects of modern life, including manufacturing, logistics of distribution, and the various stages of supply chains, scaling from the individual consumer to that of global trade. The ever rising strain imposed on industries worldwide to meet the demands of a constantly growing market leads to the pursuit for a better alternative to the widely used, but very old, bar-code label system. Albeit being very cheap, bar-code labels are being found to be inadequate in an increasing number of cases, since their low storage capacity and inability to be reprogrammed greatly hinders the establishment of a dynamic and versatile business environment desired by enterprises.

Radio frequency identification (RFID) is technology focused on object identification by reading a unique characteristic of the object (such as a unique number stored on a silicon chip attached to the object) using electromasgnetic waves. This technology offers greater efficiency and accuracy when compared with previous technologies. RFID is already widely used as a cost-effective alternative to the still widely used bar code system, providing line of sight detection even when there are several of objects tightly packed together[14].

All these advantages can be complemented, and even enhanced, by the use of smart antenna systems. These systems are used to improve the capacity of a stationary transmitter by focusing the radiated electromagnetic energy on transmit, while improving the gain pattern on receive by the RFID tag. By spatially steering signals towards the intended receivers and by dynamically tuning out interferences, smart antenna systems gained considerable attention from enterprises trying to get an edge over the competition, using these systems to automatize custom processes, by dynamically managing their inventory, with minimal external input, and by providing efficient and cost-effective services, consequence of a better resource management.

According to the intended application, smart antenna systems may be tailored according the user's needs, by selecting control algorithms with a predefined criteria, providing unique abilities to alter the radiation pattern characteristics (such as nulls, side lobe level, main beam direction and beam width).

The flexibility provided by smart antenna systems is based on their capability of performing

space-time processing, a technique that greatly improves the performance of communication systems functioning within wireless networks by using multiple antennas. By operating simultaneously on multiple sensors, space-time receivers process signal samples in both time and space, thereby improving resolution, interference suppression, service quality, considerable system capacity and data rate increases, which ultimately lead to increased spectral efficiency.

The commercial introduction of theses systems show great promise and the dramatic growth of the RFID industry are a result of this new found market opportunity. By deploying smart antennas within the reader's architecture and network, there may be considerable improvement in throughput, high-speed data reading and accurate position detection of tagged items. Smart antennas can even be used in hand-held RFID readers, making the communication process more efficient and long range, granting added value for mobile applications.

The main objective of this work was to design a system capable of performing beam steering, emulating the functionality found on smart antenna systems. The circuit developed was to be compact, fully-programmable, inexpensive and and fully compliant with american EPCGlobal standards.

Understanding the underlying functionality of smart antenna systems and the core principles on which beamforming and direction of arrival estimation algorithms are based was of fundamental importance in order to design a suitable smart antenna based structure and circuitry. At this stage, the main objective was to construct a suitable array of antennas designed to offer high directivity and a circuit capable of shifting the phase of an UHF signal according the information provided by software routines. As the overall systems was verified to be highly dependent on working frequency of the system, the design and construction of the system was subjected to various simulation tests.

The actual practical implementation of the beam steering circuit was then carried out and a prototype was built. Once all the objectives were accomplished, several tests were performed, giving way for further development of the initial system implementation. The resulting boards were independently optimized for transmission and reception applications and were thoroughly tested, so that theoretical assumptions could be compared to experimental data.

1.2 Thesis Structure

This thesis is divided into 7 chapters:

- Chapter 1 "Introduction" contains a brief introduction about the overall motivation behind the development and creation of a smart antenna system tailored for RFID applications, as it briefly summarizes some of the most important logical steps taken.
- Chapter 2 "Smart Antennas Principles" presents an overview on the basics of smart antenna systems, main case uses and their underlying architecture. The basic principles of beamforming and direction of arrival techniques are presented, offering an in depth explanation of some fundamental concepts necessary to implement and understand the functional principles
- Chapter 3 "Antenna and Array Design" introduces basic notions and parameters necessary for antenna development, emphasizing the design methodology required for microstrip antenna design. Further information related to antenna polarization and feeding methods is contained within this chapter, finalizing with an overview on antenna array theory.

- Chapter 4 "RFID Systems" offers an introduction to RFID based systems, applications and commercial viability. A comprehensive look on the different types of RFID transponders, focused on their main practical uses and characteristics, was taken in order to better understand the inherent fundamentals of these systems. This chapter also briefly presents RFID standards and protocols employed by specialized standardization bodies, such as EPCGlobal and ISO.

- Chapter 5 "Hardware Development" outlines the vision behind the development and construction of the antennas and boards used throughout this work. The antenna development was centred on the construction and enhacement of a microstrip patch antenna and, ultimately, the deployment of a antenna array. Similarly, each board represented a milestone of the developed work, enhancing hardware capabilities and integration and improving results according to the intended use of each board.

- Chapter 6 "Smart Antenna System Results" shows all the intermediate and final results, simulated and measured, throughout this work. These results are compared and discussed as to offer a better perspective of the overall work developed.

- Chapter 7 "Conclusion and Future Work" marks the end of this thesis with a summary of the work developed and presents some propositions for possible future works.

Chapter 2

Smart Antennas Principles

2.1 Introduction

Throughout the decades, communication technology has been growing at a formidable rate, creating new and innovative services at lower costs and expanding its accessibility worldwide. As mobile communications continuouslly show technological advancements, the need for better coverage, improved capacity and higher transmission quality rises, as well as the need to support the increasing number of users that require constant access to base stations. Current wireless communication systems face some challenges [1]:

- Communication devices lack capacity due to spectrum allocation restrictions;
- Increase of signal fading and spreading (in time, space and frequency), as a consequence of the radio propagation environment and the mobile communication devices that operate in said environments;
- Power constraints, as a result of limited battery life;
- Communications systems must be impervious to interference, created by frequency reuse.

In order to solve these fundamental limitations imposed by current mobile communication services, a more efficient use of the radio spectrum is imperative. One of the most practical solutions to these new found challenges is the use of spatial processing techniques, the technological core of adaptative antennas, or smart-antenna systems. Smart antennas are capable of efficiently utilizing the radio spectrum and achieving reliable and robust high-data-rate transmission.

The development of smart systems dates back to World War II, fueled by the strategic use of military applications, such as countermeasures for electronic jamming. Nowadays, with the advent of powerful low-cost digital signal processors (and ASICs - Application-Specific Integrated Circuits) and innovative software-based signal-processing techniques, adaptative systems have received great interest, becoming gradually commercial available worldwide [1].

2.2 Benefits and Drawbacks

Smart antennas offer a many of ways to improve wireless system performance. The potential to provide enhanced range and reduced infrastructure costs, enhanced link performance

and increased long-term system capacity are some of the strong points of smart antenna deployments[15]. As the industry grows, the benefits of smart antennas gradually become more apparent. Currently, the demand for smart antennas is fuelled mainly by two major reasons. First, the very fast growth of high speed analog-to-digital converters and high speed digital signal processing in communication applications, makes it possible to perform high resolution digital signal processing at very high data rates. As such, signal processing is mostly software defined near the front end of the receiver, via direct digitalizing of RF signals,supported by high speed parallel processing field programmable gate arrays (FPGA). Second, with the growing demand for all forms of wireless communication and sensing, smart antennas are the most appropriate tool to create a custom built solution, ideal for a wide array of applications, such as mobile wireless communications, software-defined radios, wireless local and metropolitan loops and area networks, mobile Internet, mobile and ad-hoc networks, high data rate communications, satellite communications, multiple-in-multiple-out (MIMO) systems, waveform diversity systems, etc. [16].

By deploying smart antenna systems, mobile wireless applications are provided with enhanced capacity and range, achieved by directing narrow beams towards the source signals of interest (SOI), while nulling the signals not of interest (SNOI). In densely populated areas, where the inter-user interference is the main source of noise, smart antenna deployments allow for higher signal-to-interference ratios and lower power levels per link, thus. By employing smart antennas within CDMA systems, it is possible to reduce multiple access interference and, consequently, increase the number of supported subscribers per cell. This allows greater frequency reuse within the same cell, leading to a large capacity increase since more carriers can be allocated per cell. This may allow a more frequent reuse frequency channels by FDM and TDMA system than when using conventional fixed antennas, since the carrier-to-interference ratio is greatly enhanced.

Spatial separation of signals is core functionality provided by smart antenna systems, achieved by focusing energy towards intended users of wasting it in other directions. This spatial filtering process allows the sharing of spectral resources and, as consequence, base stations can be placed further apart, which may lead to more cost-effective deployments. This concept is known as Space Division Multiple Access (SDMA) and allows multiple users to operate in the same cell, on the same frequency/time slot provided, using smart antennas to separate the signals. In wireless communications deployments most base stations sectorize each cell onto three 120^{o} swats, allowing the system capacity to, theoretically, triple within a single cell, since this approach allows more users to be supported within a limited spectrum allocation when compared to conventional antennas. [16]. Moreover, by directing the beams towards points of interest, the multipath and the inter-symbol-interference present in mobile radio environments are attenuated. This can be accomplished by implementing a constant modulus based algorithms, which will be discussed further ahead, to null multipath signals, allowing the system to achieve higher data rates by simultaneously reducing both co-channel interference and multipath fading. This is important in MIMO communications systems and in waveform diverse MIMO radar systems, where correlation between the various signals at each array element can be exploited, improving performance and array resolution, and mitigating signal distortion and interference.

Finally, security is another fundamental advantage of smart antennas. Information security is better guaranteed since the intruder must be placed in the same direction as the user as "seen" from the base station in order to access the communication link.

Albeit the advantages of deploying smart antenna systems are significant, some consider-

ations must be taken into account. The complexity of the smart antenna transceiver is much greater than that of one found in a conventional base station. Another challenge is the need to create new resource and mobility management solutions for communication networks. In SDMA, when the angle of two user using the same physical communication channel in the same cell collide, one of them must be immediately switched to another channel, so that the connection doesn't break.

Another problem imposed by the deployment of smart antennas is the gain of the antenna array. This may prove to be a challenge for lower frequencies, resulting in very large arrays, incompatible with today's growing demand for less visible hardware, and for higher frequencies, where the size of the array is not a problem, but the gain provided is not ideal for practical applications[1].

2.3 Smart Antenna Systems Architecture

All wireless communication systems are comprised of reception and transmission sections, essential for creating a sustainable, interchangeable information link between sender and receiver. The term smart antennas incorporates all situations in which a system uses an antenna array capable of dynamically adjusting its radiation pattern as required by the surrounding environment or imposed by the system. Thus, a framework employing smart antenna technology is enabled to process signals induced on a sensor array and can differentiate the desired signals from unwanted interferences. These advanced features are highly dependent on the reception and the transmission sections of these systems. An overall look of these two crucial parts is presented below.

2.3.1 Receiver

As wireless communications systems evolved, the introduction of multiple antennas at the receiver unit, from wireless points to mobile terminals, changed from a purely theoretical concept to a reality. Besides the antennas themselves, wireless systems employing a smart antennas are composed of a radio unit, a beamforming unit and a signal processing unit. The deployment of multiple receiver antennas can be exploited for diversity, multiplexing or coherence gains in order to increase data transmission rates and reception quality. In addition to simply increasing the dimension of the signal space, multiple antennas are directly related to spatial directivity, responsible for linking the radiating elements of the array to the physical environment.

However, as the number of antennas increases within the array, the number of parameters that need to be estimated and processed rise dramatically, making the design of powerful and efficient receivers a challenge.

Depending on the application, antenna arrays can have multiple dimensions, depending on the space one wants to access or the complexity of the system one wants to employ/create.

The signal received from these antennas is fed to the radio unit, for demodulation, which consists of down-conversion chains, one for each array element, and analog-to-digital converters. Each of captured signals is then combined into one, and decoded.

The signal processing unit, based on the received signal, calculates the complex weights $\omega 1$, $\omega 2$,... with which the received signals from each of the array's elements is multiplied, determining the antenna array's pattern in the uplink direction. These weights can be optimized depending if the application prioritizes the maximization of the power of the received signal

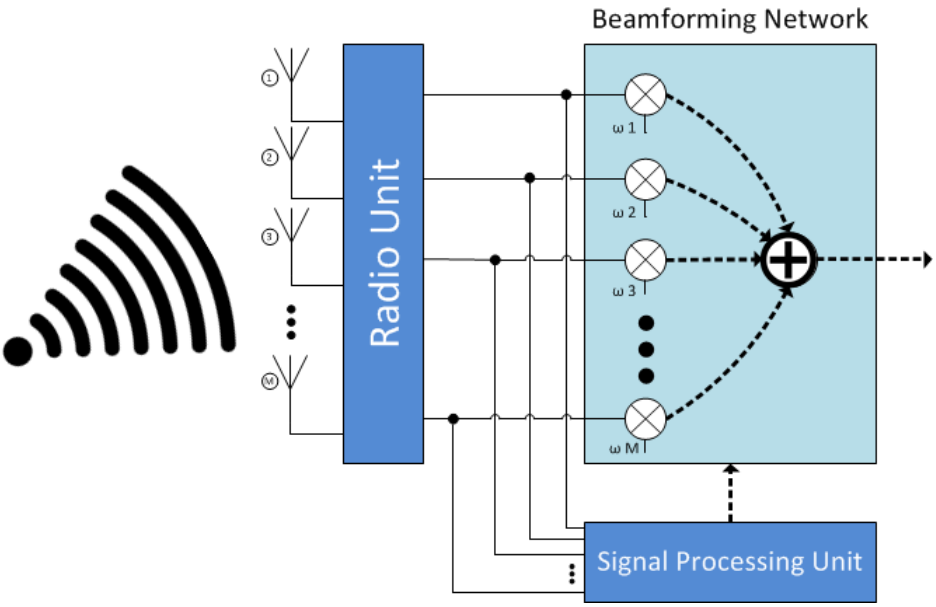

Figure 2.1: Reception sector of a smart antenna

from the desired user or if it requires the maximization of the SIR by suppressing the signal received from the interference sources.

2.3.2 Transmitter

Normally the adaptative process is only applied to the uplink/reception since the mobile unit consumes less transmission power and thus its operational time increases[1].

The transmission section of the smart antenna is very similar to its reception part.

The signal is fed to the beamforming network and is split into M branches, which are weighted by the weights $\omega 1$, $\omega 2$,... in the beamforming unit. The signal processing unit is responsible for calculating the weights, which can be extrapolated from the information given by the direction of arrival from the uplink, thus forming the radiation pattern in the downlink direction. Once split and weighted, the signal must be modulated in the radio unit, which consists of digital-to-analog converters and chains of up-converters.

Current wireless communication systems do not equip mobile devices with smart antenna systems, thus there is limited knowledge of the Channel State information (CSI) available. Consequently, optimum beamforming in downlink, as well as stable performance at the uplink cannot be guaranteed[1]. Little effort has been put in order to equip mobile stations with smart antenna systems due to some practical difficulties:

- The mobile device has limited space, thus limiting the possibility of implementing an antenna array with the necessary number of elements for efficient spatial signal processing. Also, coupling between two antennas in proximity may reduce the overall quality of the system due to coupling;

- The cost and complexity necessary to equip a mobile device with smart antenna are much greater than its implementation at a stationary station;

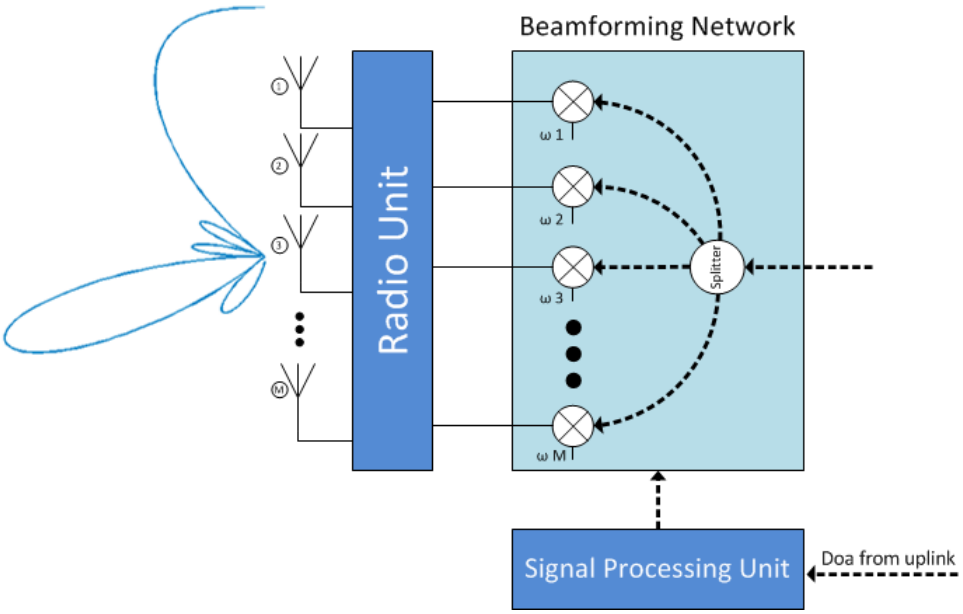

Figure 2.2: Transmission sector of a smart antenna

- The movement of mobile devices require a constant-changing radiation pattern from its smart antenna, making it essential to equip these devices with expensive, complex and power consuming processors.

In order to overcome these limitations the performance gain should be large enough to offset additional costs and power consumption of these mobile devices. Technical limitations such as these create problems for deploying digital beamforming antennas in both satellites, land-fixed and mobile units, therefore constituting a barrier that must be overcome in order to reach a new level in worldwide satellite communication systems[1].

2.4 Beamforming and DOA Techniques

Next is presented the theoretical basis necessary for the development of beamforming and DOA estimation solutions for smart antenna systems. These subsections are based on documents [17] and [1].

2.4.1 Propagation Delays and Angle Estimation

The functional principles of smart antenna systems are deeply dependent on the configuration of its array of sensors, influencing not only the complexity of the system and its basic weighting calculation algorithm, but also determining the spatial dimension one wants to access.

Being $s(t)$ a signal generated by a source in the far-field of a smart antenna system employing a uniform linear array of N sensors, the propagating wave of $s(t)$ would be approximately an uniform plane wave when captured by the array. At each sensor of the array, $s(t)$ is received with a different phase, measured with respect to the phase of the signal captured at given element of the array, serving as the reference. The phase difference measured relatively

to the time difference at which the signal $s(t)$ arrives at the reference element and the time it arrives at element k. The time delay of arrival can be calculated as follows

$$\triangle\tau_k = \frac{kd\sin\theta_s}{c} \tag{2.1}$$

where d is the spacing between each element and c is the speed of light. Similarly, knowing d and measuring the time delay $\triangle\tau_k$, the angle of arrival θ_s, can be written as

$$\theta_s = \sin^{-1}\left[\frac{c\triangle\tau_k}{kd}\right] \tag{2.2}$$

Considering that the signal $s(t)$ is a narrowband signal, with low pass equivalent $s_l(t)$, carrier frequency f_c and symbol period T, $s(t)$ is received by the k^{th} element as

$$x_k(t) = s_l(t - \triangle\tau_k)e^{-j2\pi f_c\triangle\tau_k} \tag{2.3}$$

In this case it is possible to draw a connection between the time delay $\triangle\tau_k$ and the phase shift $\triangle\psi$ of the received signal at each element of the array as

$$\triangle\psi = 2\pi\frac{kd\sin\theta_s}{\lambda_c} \tag{2.4}$$

where λ_c is the wave length corresponding to the carrier frequency. An incoming signal from a direction perpendicular to the array has time delay, and correspondent phase shift, of zero, thus it is transmitted by a source located at $\theta_s = 0^{\text{o}}$. Other angles can be established using this method, forming the basis of the algorithm's structure employed by smart antenna systems equipped with uniform linear arrays.

2.4.2 Eigenstrucuture of the Array Correlation Matrix

The signal $s(t)$ received by a smart antenna system is sampled with period T much greater than each of the propagation delays across the array, that is $T >> \triangle\tau_k$. For each k element of the array, being the n^{th} symbol of the i^{th} signal denoted as $s_i[n]$ for $i = 0, 1, 2..., r-1$ and being r the number of existing signals, the base-band signal can be expressed as

$$x_k[n] \approx \sum_{i=0}^{r-1} s_i[n]a(\theta_i) \tag{2.5}$$

Considering all the array elements, Equation 2.5 can be written in a matrix form, shown below

$$\begin{bmatrix} x_0[n] \\ x_1[n] \\ \vdots \\ x_{N-1}[n] \end{bmatrix} = \begin{bmatrix} a_0(\theta_0) & a_0(\theta_1) & \cdots & a_0(\theta_{r-1}) \\ a_1(\theta_0) & \ddots & & \vdots \\ \vdots & & \ddots & \vdots \\ a_{N-1}(\theta_0) & \cdots & \cdots & a_{N-1}(\theta_{r-1}) \end{bmatrix} \begin{bmatrix} s_0[n] \\ s_1[n] \\ \vdots \\ s_{r-1}[n] \end{bmatrix} + \begin{bmatrix} v_o[n] \\ v_1[n] \\ \vdots \\ v_{N-1}[n] \end{bmatrix} \tag{2.6}$$

being $v_k[n]$ the additive noise at each element. The compact matrix notation as is the following

$$x_n = [\ a(\theta_0) \quad a(\theta_1) \quad \cdots \quad a(\theta_{r-1})\ ]s_n + v_n = As_n + v_n \tag{2.7}$$

The columns of the matrix A, denoted by $a(\theta_i)$, are called the steering vectors of the signal $s_i(t)$ which, for a N-element ULA with spacing d between adjacent elements, are given by

$$a(\theta) = [\ 1 \quad e^{-j\frac{2\pi d}{\lambda}\sin\theta_s} \quad \cdots \quad e^{-j(N-1)\frac{2\pi d}{\lambda}\sin\theta_s}\ ] \tag{2.8}$$

and form a linearly independent set, given that the angle of arrival of each of the r signals is different. The vector v_n represents the uncorrelated noise present at each element of the array.

Once the steering vector for an array antenna is derived, the autocovariance matrix can be computed. Assuming that the v_n and s_n are uncorrelated and v_n is a vector of Gaussian white noise with zero mean and correlation matrix $\sigma^2 I$, the array correlation matrix (or covariance matrix) of the received signal can be written as

$$R_{xx} = E[x_n x_n^H] = AR_{ss}A^H + \sigma^2 I_{N\times N} \tag{2.9}$$

The autocovariance matrix R_{xx} is Hermitian (complex conjugate transpose) and, as such, can be unitarily decomposed and has real eigenvalues. Also, assuming that $N > r$, any vector q_n which is orthogonal to the columns of A is an eigenvector of $R_{xx}$with the corresponding eigenvalue of σ^2, as shown below

$$R_{xx}q_n = (AR_{ss}A^H + \sigma^2 I)q_n = \sigma^2 q_n \tag{2.10}$$

Because A has dimension of $N \times r$ there exist $N - r$ linearly independent eigenvectors, whose eigenvalues are equal to σ^2, which span a space known as noise subspace. On the other hand, if q_s is an eignevector of $AR_{ss}A$, then

$$R_{xx}q_s = (AR_{ss}A^H + \sigma^2 I)q_s = (\sigma_s^2 + \sigma^2)q_s \tag{2.11}$$

where σ_s^2 is the eigenvalue of $AR_{ss}A^H$. The eigenvector q_s lies in the column-space of A ,since the vector $AR_{ss}A^Hq_s$ is a linear combination of the columns of A. There are r such linearly independent eigenvectors of R_{xx}, which span a space known as the signal subspace.

Finally, once determined the covariance matrix it can be eigendecomposed as

$$R_{xx} = QDQ^H = [\ Q_s \quad Q_n\ ] \begin{bmatrix} D_s & 0 \\ 0 & \sigma^2 I \end{bmatrix} [\ Q_s \quad Q_n\ ]^H \tag{2.12}$$

The matrix Q is partitioned into matrix Q_s, of dimension $N \times r$, whose columns are the r eigenvectors corresponding to the signal subspace, and a $N \times (N - r)$ matrix Q_n whose columns correspond to the "noise" eigenvectors. The diagonal matrix D has as its diagonal elements the eigenvalues of R_{xx} and is partitioned into a $r \times r$ diagonal matrix D_s whose diagonal elements are the "signal" eigenvalues and an $(N-r)\times(N-r)$ scaled identity matrix $\sigma^2 I_{N\times N}$ whose diagonal elements are the $N \times r$ "noise" eigenvalues.

Changes in the weather, reflective and absorptive bodies in the nearby surrounding environment, and antenna location, do not allow, however, a precise estimation of array response and noise covariance. Calibrations must be done frequently and are subject to phase and gain errors due to some factors, like misaligned elements of the array. Since the matrix R_{xx} is never exactly known it must be estimated from the signal data collected by the system. Normally an

estimator is used to estimate the correlation matrix, known as the sample spatial covariance matrix, which can be obtained by averaging rank-one data matrices of the form $(x_n x_n^H)$ as

$$R_{xx} = \frac{1}{K} \sum_{i=0}^{K-1} x_n x_n^H \tag{2.13}$$

being K the total number of snapshots of data available from the sensors of the array.

The eigendecomposition of the covariance matrix of the received signal is the basis for subspace DOA estimation algorithms that characterize smart antenna systems. This chapter presents various DOA estimation algorithms, enumerating the most significant properties of each method depending on the application and the surrounding environment.

2.4.3 Beamforming Fundamentals

With the direction of incoming signals known or estimated, the next step is to use spatial processing techniques to improve reception performance of the receiving antenna array based on the collected information. Beamforming techniques place the radiation pattern's maximum towards the signal-of-interest (SOI) and, ideally, steer nulls towards directions of interfering signals or signals-not-of-interest(SNOI). This is a dynamic process that continually changes in order to accommodate the incoming SOIs and SNOIs by adjusting the weight vector $w = [w_1, w_2, ..., w_N]^T$ according to the information collected by the system. If a weighted linear combination of the output of each element is taken, the array output can be computed by

$$y[n] = \sum_{k=0}^{N-1} w_k x_k[n] \tag{2.14}$$

which can be represented in vector notation as

$$y[n] = w^H x_n \tag{2.15}$$

where the $N \times 1$ complex vector w contains the beamformer weights w_k, $k = 0, 1, ..., N$.

By controlling the complex weight vector w, the response of the antenna array can be altered by adjusting the elements of the array, since the magnitude and phase of the beamformer determine the pattern and directivity of the antenna. This process is known as spatial filtering, or beamforming, existing various methods capable of achieving a desired beampattern, which can be written in vector notation as

$$W(\theta_0) = \frac{1}{N} \sum_{n=0}^{N-1} w_n e^{-ejn\omega} = w^H a(\theta) \qquad \omega = 2\pi d \sin(\theta) \tag{2.16}$$

where w is the vector that contains the beamformer weights, and is given by

$$w = \frac{1}{N} [\ w_0^* \quad w_1^* \quad \cdots \quad w_{N-1}^*\ ]^T \tag{2.17}$$

and $a(\theta)$ is the steering vector represented by Equation 2.8. The beamformer output can be written as the vector of inner product of the weight vector w and the steering vector $a(\theta)$ given by

$$y[n] = \frac{1}{N} \sum_{k=0}^{N-1} w_k x_k[n] = s_0[k] W(\theta_0) \tag{2.18}$$

If the vector w and $a(\theta)$ are orthogonal the signal is canceled out, since $w^H a(\theta) = 0$. This can be useful to filter interfering signals that arrive at the smart antenna and is one of the core strengths of these systems. This chapter presents various beamforming algorithms and enumerates the advantages and disadvantages of each one depending on the intended application or surrounding environment.

2.4.4 Direction of Arrival Estimation Algorithms

Direction of arrival methods are next analyzed. The methods studied are Multiple Signal Classification (MUSIC), Root-MUSIC and Estimation of Signal Parameters via Rotational Invariance Techniques (ESPRIT), being each of these methods thoroughly explanied, based on the documents [15], [1] and [16]

2.4.4.1 Multiple Signal Classification Algorithm

The multiple signal classification (MUSIC) method is a relatively simple and efficient high resolution eigenstrucuture variant of DOA estimation methods. Of the signal-subspace algorithms, MUSIC is, perhaps, the most studied, in large part due to its generality and its promise to provide unbiased estimates of the number of signals, angles of arrival and strength of the waveforms via simple matricial calculations. The MUSIC method estimates the noise subspace from available samples by assuming that the noise in each channel is uncorrelated and that the incoming signals are somewhat correlated. However, in order to utilize the MUSIC algorithm, it is necessary to know, or determine by searching the eigenvalues, the number of incoming signals. The array correlation matrix of the emitter, for the algorithm to be applicable, must be full-rank, meaning $r' = r$, and can be calculated using the mathematical expression shown in Equation 2.13. Once the eigenvalues and eigenvectors of R_{xx} are found, it is possible to produce D (being D the number of incident signals) eigenvectors associated to the signals and $M - D$ (being M the number of array elements) eigenvectors associated with the noise, both associated with the smallest eigenvalues. A $M \times (M - D)$ dimensional subspace spanned by white noise can then be constructed such as

$$E_N = [e_1 \quad e_2 \quad \dots \quad e_{M-D}] \tag{2.19}$$

The noise subspace eigenvectors can be assumed to be orthogonal to the array steering vector at the D angles of arrival, making it possible to apply the Euclidean distance $d^2 = a(\theta)^H E_N E_N^H a(\theta)$ for each of the incoming signal's angles. The angle of arrival of the desired signals can now be estimated by calculating the MUSIC spatial spectrum over the region of interest:

$$P_{MU}(\theta) = \frac{1}{a(\theta)^H E_N E_N^H a(\theta)} \tag{2.20}$$

However, even though the MUSIC algorithm shows significant performance advantages, the incurred computational and storage costs are high, since it is necessary to calibrate and store the array response of the system according to all known combinations of the source

parameters. Another fundamental disadvantage is the substantial performance reduction of the MUSIC algorithm when used in low SNR environments. To overcome these shortcomings, alternative DOA methods may be employed, which will be discussed next.

2.4.4.2 Root-MUSIC Algorithm

The MUSIC algorithm, discussed previously, is arranged in such a way that it can be applied to any arbitrary array, regardless of the position of the array elements. This method can be simplified for the case when the antenna is an ULA, limiting the algorithm to simply finding roots of a polynomial, as opposed to plotting the pseudo-spectrum and searching for its peaks. The Root-MUSIC algorithm is as a specific tailored version of the MUSIC algorithm for ULA, where by rearranging the pseudo-spectrum given by the MUSIC algorithm

$$P_{MU}(\theta) = \frac{1}{a(\theta)^H E_N E_N^H a(\theta)} \tag{2.21}$$

into one where the denominator expression is simplified by defining the matrix $C = E_N E_N^H$, which is Hermitian, leads to the RLS pseudo-spectrum expression, given by

$$P_{RMU}(\theta) = \frac{1}{|a(\theta)^H C a(\theta)|} \tag{2.22}$$

Considering Equation 2.22, the denominator of Equation 2.22 can be written as

$$a(\theta)^H C a(\theta) = \sum_{m=1}^{M}\sum_{n=1}^{M} e^{-jkd(m-1)sin(\theta)} C_{mn} e^{jkd(n-1)sin(\theta)} = \sum_{l=-M+1}^{M-1} c_l e^{jkdlsin(\theta)} \tag{2.23}$$

being c_l the sum of the diagonal elements of C along the l^{th} diagonal.

In order to simplify Equation 2.23 to the form of a polynomial whose coefficients are c_l, the following equality can be used

$$D(z) = \sum_{l=-M+1}^{M-1} c_l z^l \tag{2.24}$$

where $z^l = e^{-jkdsin(\theta)}$. The roots of $D(z)$ that are closest to the unitary circle correspond to the poles of the MUSIC pseudo-spectrum. Each root can be complex since Equation 2.24 is of order $2(M-1)$ and thus has roots of $z_1, z_2, ..., z_{2(M-1)}$, being $\arg(z_i)$ the phase of the angle of z_i. This implies that the exact zeros in $D(z)$ exist when the root magnitudes $|z_i|$=1 and that the DOA can be calculated by comparing $e^{jarg(z_i)}$ to $e^{jkdsin(\theta_i)}$ in order to get

$$\theta_i = -\sin^{-1}(\frac{1}{kd}\arg(z_i)) \tag{2.25}$$

Through various simulations, Barabell demonstrated that the Root-MUSIC algorithm has better resolution that the standard MUSIC method when employed in low SNR envirtonments.

2.4.4.3 Estimation of Signal Parameters via Rotational Invariance Techniques Algorithm

Estimation of signal parameters via rotational invariance techniques, or ESPRIT, is a computationally efficient and robust method of DOA estimation. As the name implies, this technique aims to exploit the rotational invariance in the signal subspace which is created by two arrays with a translational invariance structure. ESPRIT assumes that the N-element array is composed of two identical translated N'-element sub-arrays, being $N' < N \leqslant 2N'$, in the sense that the array elements need to form matched pairs (known as doublets) with an identical displacement vector (that is, the second element of each pair ought to be displaced by the same distance and in the same direction relative to the first element) as shown in Figure 2.3. As such, the sub-arrays may overlap, like in Figure 2.3a), meaning an array element may be a member of both sub-arrays ($N < 2N'$) or may not share elements ($N = 2N'$), as shown in Figure 2.3b).

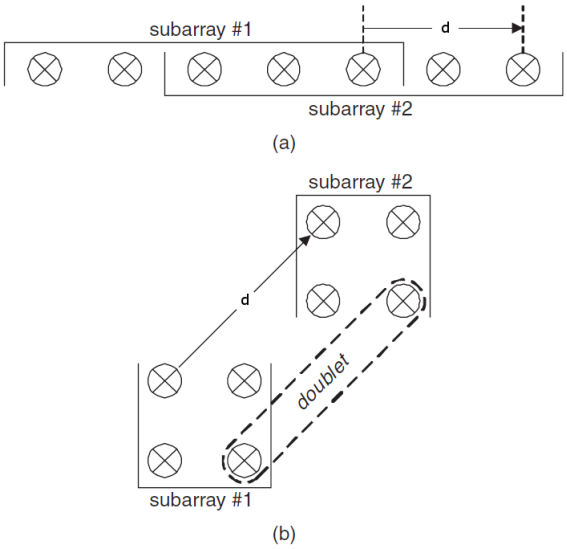

Figure 2.3: ESPRIT antenna array geometry example: (a) array consists of two overlapping arrays, (b) consists of two identical and disjoint arrays [1]

As with MUSIC, ESPRIT assumes that there are less narrow-band sources centered at the center frequency f_0 than radiating elements of the antenna array.

Assuming the rotational invariance of the ESPRIT's sub-arrays and considering the configuration illustrated in Figure 2.3 as an example, the signal induced at the each doublet can be expressed as

$$x_1(k) = [a_1(\theta_1) \quad a_1(\theta_2) \quad \dots \quad a_1(\theta_D)] \cdot \begin{bmatrix} s_1(k) \\ s_2(k) \\ \vdots \\ s_D(k) \end{bmatrix} + n_1(k) = A_1.s_D(k) + n_1(k) \tag{2.26}$$

and

$$x_2(k) = A_2.\Phi.s_D(k) + n_2(k) \tag{2.27}$$

being A_i the Vandermonde matrix of steering vectors for the given doublet, n_i the noise collected by each sub-array andΦ the diagonal of a DxD unitary matrix with phase shifts between the doublets for each angle of arrival, given by $diag\left\{e^{jkd\sin\theta_1}, e^{jkd\sin\theta_2}, \ldots, e^{jkd\sin\theta_D}\right\}$.

As such, the received signal by the array, given the contribution of both doublets, can be be mathmatically expressed as

$$x(k) = \begin{bmatrix} x_1(k) \\ x_2(k) \end{bmatrix} = \begin{bmatrix} A_1 \\ A_1.\Phi \end{bmatrix}.s(k) + \begin{bmatrix} n_1(k) \\ n_2(k) \end{bmatrix} \tag{2.28}$$

Known the received signal, the correlation matrix can be calculated for the complete array, given by

$$R_{xx} = E[x.x^H] = AR_{SS}A^H + \sigma_n^2 I \tag{2.29}$$

and for the two sub-arrays, each containing a set of eigenvectors corresponding to the D signals present, given by

$$R_{11} = E[x_1.x_1^H] = AR_{SS}A^H + \sigma_n^2 I \tag{2.30}$$

and

$$\bar{R}_{22} = E[x_2.x_2^H] = A\Phi R_{SS}\Phi^H A^H + \sigma_n^2 I \tag{2.31}$$

Each of the covariance matrices presented by Equations 2.30 and 2.31 is full rank and has a set of eigenvectors that correspond to the number os signals present. The signal subspace for the two doublets can be constructed, resulting in two matrices, E_1 and E_2, that, because of the invariance structure of the array, are the decompositions of the overall signal subspace given by E_x. Both the E_1 and $E_2$are $M \times D$ matrices, being their columns comprised of D eigenvectors, corresponding to the greatest eigenvalues of R_{11} and R_{22}, which are realated by a non-singular transformation matrix, Ψ, such that

$$E_2 = E_1 T^{-1}\Phi T = E_1\Psi \tag{2.32}$$

where $\Psi = T^{-1}\Phi T$, or $\Phi = T^{-1}\Psi T$. Thus, the eigenvalues of Ψ must be equal to the diagonal elements of Φ such that $\lambda_1 = e^{jkd\sin\theta_1}$, $\lambda_2 = e^{jkd\sin\theta_2}$,... ,$\lambda_D = e^{jkd\sin\theta_D}$ and the columns of T must be the eigenvectors of Ψ. This relationship is the base for the development of the ESPRIT method and its properties. The rotation operator, Ψ, maps the signal subspace E_1 into the signal subspace E_2 and must now be estimated. Such can be accomplished, using the total least-squares criterion. For a smart antenna systems employing an ULA antenna, E_1 and E_2 can constructed by selecting the first and last $\frac{M}{2}+1$ rows ($\frac{M+1}{2}+1$ for odd arays), repectively. This allows the construction of the $2D\times 2D$ matrix

$$C = \begin{bmatrix} E_1^H \\ E_2^H \end{bmatrix} \begin{bmatrix} E_1 & E_2 \end{bmatrix} = E_C \Lambda E_C^H \tag{2.33}$$

being $\Lambda = diag\{\lambda_1, ..., \lambda_{2D}\}$ and E_C is the result of the eigendecomposition of C, which can partition into four $D \times D$ submatrices in the form of

$$E_C = \begin{bmatrix} E_{11} & E_{12} \\ E_{21} & E_{22} \end{bmatrix} \tag{2.34}$$

which is used to estimate the rotational operator Ψ in following fashion

$$\Psi = -E_{12}E_{22}^{-1} \tag{2.35}$$

After calculating the eigen values of Ψ it is then possible to estimate the angle of arrival of the received signal by

$$\theta_i = \sin^{-1}\left(\frac{\arg(\lambda_i)}{kd}\right) \qquad d = 1, 2, \ldots, D \tag{2.36}$$

where ψ_i represents the eigenvalues of Ψ. This result is independent of the actual value $A(\Theta)$ (as long as remains full-rank), thus making unnecessary for the array to be calibrated in order to estimate the angle of arrival from the sources.

The previously presented DOA estimation algorithms were tested, being the results obtained disclosed in Chapter 6 and subjected to a critical analysis based on their signal position estimation accuracy.

2.4.5 Adaptative Beamforming Algorithms

Adaptative beamforming techniques for smart antenna systems are next analyzed. The methods studied are Least Mean-Square (LMS), Recursive Least-Squares (RLS), Constant Modulus (CM) and Least-Squares Constant Modulus (LSCM), being each of these methods thoroughly explanied, based on the documents [1], [16] and [2].

2.4.5.1 Least Mean-Square Algorithm

The Least Mean-Square (LMS) algorithm is a robust, low-complexity adaptative filtering technique that is widely employed by several communications systems. The LMS method updates the weights necessary to introduce into the system by iteratively minimizing the mean-square error by changing the weights along the estimated gradient based on the negative steepest descent method. The performance surface, also known as cost function, of this algorithm can be established by finding the mean-square-error, demonstrated in Figure 2.4, by:

$$\varepsilon(k) = d(k) - \omega^H(k)x(k) \tag{2.37}$$

where $\bar{\omega}^H(k)\bar{x}(k)$ is the array output, $y(k)$, and the signal $d(k)$ is the reference signal that, preferably, must be identical, or highly correlated, with $s(k)$. Alternatively, $d(k)$ may also be highly uncorrelated with the interfering signals $i_n(k)$. Through simple mathematical operations, it can be shown that the mean square error is calculated as

$$|\varepsilon(k)|^2 = |d(k) - \omega^H(k)x(k)|^2 \tag{2.38}$$

Which can be simplified into, by supressing the time notation dependence k, and thus resulting in the cost function, also known as performance surface,

$$E[|e|^2] = E[|d|^2] - 2\omega^H r + \omega^H R_{xx}\bar{\omega} \tag{2.39}$$

To locate the minimum, the gradient method is used. The minimum occurs when the gradient is zero.

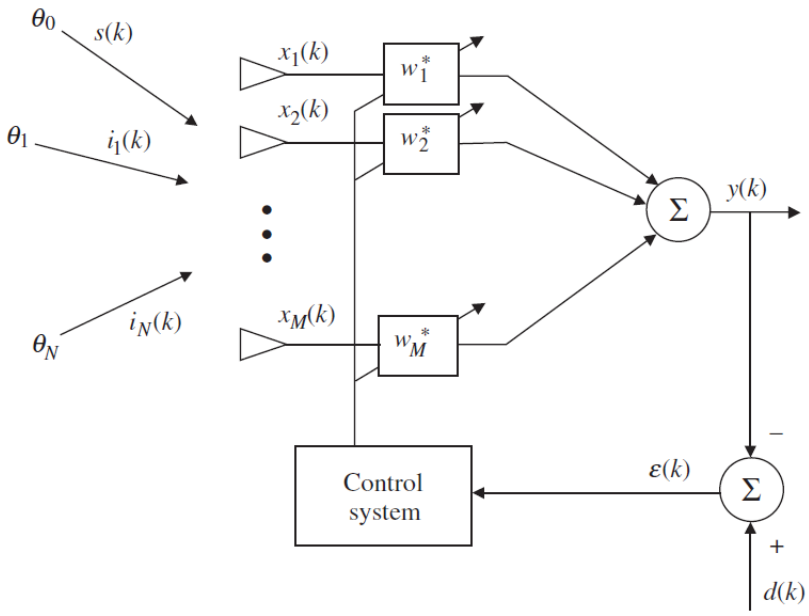

Figure 2.4: Minimum square error adaptative system [2]

$$\nabla_\omega(J(\omega)) = 2R_{xx}\omega - 2r \tag{2.40}$$

where $r = \varepsilon\{xd^*\}$ is the reference signal covariance vector. The optimum weight solution is

$$\omega_{opt} = R_{xx}^{-1}r \tag{2.41}$$

In order to calculate the optimum solution, the array correlation matrix (R_{xx}) and the signal correlation vector (r) must be calculated, which requires sufficient knowledge of the desired signal statistics. However, acquiring this knowledge can be a very expensive and time consuming process for wireless communication systems, mainly for fast-fading scenarios. Instead, a estimate of such values can be obtained, over a range of snapshots for each instant in time, given as

$$R_{xx}(k) \approx x(k)x^H(k) \tag{2.42}$$

and

$$r(k) \approx d^*(k)x(k) \tag{2.43}$$

where R_{xx} is the autocovariance matrix and $r(k)$ is the signal correlation vector. Calculated the weights, the iterative method of steepest descent is used to approximate the gradient of the cost function, which is given by

$$\omega(k+1) = \omega(k) - \frac{1}{2}\mu\nabla_\omega(J(\omega(k))) \tag{2.44}$$

being μ the step-size parameter and ∇_ω the gradient of the performance surface. By substituting the instantaneous correlation approximations, the LMS algorithm updates the weight vectors according to

$$\omega(k+1) = \omega(k) - \mu[R_{xx}\omega - r] = \omega(k) + \mu e*(k)x(k) \tag{2.45}$$

The step-size parameters is scalar constant that controls the rate of convergence and stability of the algorithm. Some considerations must be taken into account in order to estimate the adequate step-size of the system. If $\mu$is too small the convergence is slow and the system will be affected by overdamp, making the adaptative array unable to acquire the signal of interest fast enough to dynamically track the signal. On the other hand, if $\mu$is too large, the algorithm will overshoot the optimum weights of interest due to the overly fast convergence of the system, making the weights oscillate around the optimum weight but never accurately track the desired solution. The stability of the systems is guaranteed by restricting the step size parameter in the interval

$$0 < \mu < \frac{2}{\lambda_{max}} \tag{2.46}$$

A satisfactory condition for solution convergence of the mean of the LMS weight vector can be written as

$$0 < \mu < \frac{2}{\sum_{i=1}^{N} \varepsilon\{x_i^2\}} \tag{2.47}$$

Assuming that all interfering signals are noise and there is only one signal of interest, the following approximation can be used alternatively to the one presented by Equation (2.47):

$$0 < \mu < \frac{1}{2\sum_{i=1}^{N} \varepsilon\{x_i^2\}} \tag{2.48}$$

Therefore it is possible to extrapolate that the eigenstrucuture of the array correlation matrix $\hat{R}_{xx}$ greatly influences the convergence characteristics of the algorithm. This dependency is responsible for the slow convergence of the LMS algorithm for colored noise input signals, a fundamental problem that worsens as the eigenvalues progressively deviate from each other. Depending on the eigenvalue spread, the convergence time can be very long and highly data dependent, with the possibility to even degenerate to the point which the LMS algorithm may not have the necessary iteration time to guarantee the convergence of the weight vector towards the optimum solution, thus not guaranteeing the adaptation of the system to its dynamic operational environment . To circumvent this problem, the algorithms discussed below may be utilized as suitable alternatives.

2.4.5.2 Recursive Least-Squares Algorithm

The RLS beamformer is a method that, unlike the LMS algorithm, which uses the method of steepest descent to update the weight vector by minimizing the ensemble average of the error squares, approximates the solution directly using the method of least squares to adjust the weight vector. The method of least squares bypasses the additional burden of approximating an optimization procedure since the weight vector is chosen as to minimize a cost function based on the sum of error squares over a time window, meaning that the solution is minimized recursively. The recursions for the most common version of the RLS algorithm are a result of the weighted least-squares (WLS) cost function,

$$J_{w,w*} = \sum_{i=1}^{k} \lambda^{k-1} |e(i)|^2 \tag{2.49}$$

being $e(i)$ the error signal, and $0 < \lambda \leq 1$ an exponential scaling factor known as forgetting factor or exponential weighting factor. The forgetting factor is used to deemphazise the earliest data samples and emphasize the most recent ones, which is important for dynamic environments where signal sources can change or slowly move with time. By differentiating the cost function $J_{w,w*}$with respect to $w*$ and solving for the minimum, it can be shown that

$$\left[\sum_{i=1}^{k} \lambda^{k-1} x(i) x^H(i)\right] w(k) = \sum_{i=1}^{k} \lambda^{k-1} x(i) d*(i) \tag{2.50}$$

The weight can be obtained by defining the quantities

$$R_{xx}(k) = \sum_{i=1}^{k} \lambda^{k-1} x(i) x^H(i) \tag{2.51}$$

and

$$r(k) = \sum_{i=1}^{k} \lambda^{k-1} x(i) d*(i) \tag{2.52}$$

being k the data block length and last time sample k and $R_{xx}(k)$, $r(k)$ the last k time samples of the correlation estimates. The summations in Equation 2.51 and Equation 2.52 can be broken into two terms: the summations for values up to $i = k - 1$ and last term form $i = k$

$$\hat{R}_{xx}(k) = \lambda \sum_{i=1}^{k-1} \lambda^{k-1-i} x(i) x^H(i) + x(k) x^H(k) = \lambda \hat{R}_{xx}(k-1) + x(k) x^H(k) \tag{2.53}$$

$$\hat{r}(k) = \lambda \sum_{i=1}^{k-1} \lambda^{k-1-i} x(i) d*(i) + x(k) d*(k) = \lambda \hat{r}(k-1) + x(k) d*(k) \tag{2.54}$$

Thus, future values for the array correlation estimate and the vector correlation estimate can be found recursively using previous values and, by using Equation 2.53, it is possible to derive a recursion relationship for the inverse of the correlation matrix. The inverse of Equation 2.53 can be found via the Sherman Morrison-Woodbury theorem, resulting in the recursion formula:

$$\hat{R}_{xx}^{-1}(k) = \lambda^{-1} \hat{R}_{xx}^{-1}(k-1) - \lambda^{-1} g(k) x^H(k) \hat{R}_{xx}^{-1}(k-1) \tag{2.55}$$

by defining the gain vector $g(k)$ as

$$g(k) = \left[\lambda^{-1} \hat{R}_{xx}^{-1}(k-1) - \lambda^{-1} g(k) x^H(k) \hat{R}_{xx}^{-1}(k-1)\right] x(k) = \hat{R}_{xx}^{-1}(k) x(k) \tag{2.56}$$

The optimum solution, in terms of iteration number k, is represented as

$$w(k) = w(k-1) + g(k)\left[d*(k) - x^H(k)w(k-1)\right] \tag{2.57}$$

The RLS algorithm deviates from LMS algorithm as it utilizes information contained within the signal's input data, extending back to the time instance the algorithm initiated. This important feature allows the RLS algorithm to converge much faster than the ordinary LMS method. This performance improvement is, however, achieved at the expense of a large increase in computational complexity by requiring greater complex multiplications per iteration. Also, the RLS method may present divergent behavior in a finite-precision environment and also stability problems, usually as a consequence of the loss of symmetry and positive definiteness of the matrix $R^{-1}(k)$.

2.4.5.3 Constant Modulus Algorithm

The constant modulus algorithm was created as an adaptative filtering technique with the intent to correct multipath and interference based degadations in constant envelope waveforms, such as the ones used by wireless and radar systems which use signal modulation schemes such as FM, PSK, FSK, QAM and polyphase. These signals share a common property, called constant modulus, av their amplitude is, in ideal conditions, constant. The constant modulus algorithm takes advantage of the prior knowledge of the modulation's characteristics of the incoming signal and achieves a viable steady state response from the array via optimization techniques "blind" to the contents of the signal. However, in fading channels, since the received signal is a composite of multipath terms, the magnitude of that signal varies, and, in frequency selective channels, the constant modulus property can be lost. These limitations can be overcome by indirectly measuring the quality of the filtered signal and estimating its original amplitude, thus guaranteeing the convergence of the algorithm and the acquisition of satisfactory weight vectors. Constant modulus algorithm calculates beamform weight vectors that minimize the following cost function, also known as dispersion function of order p:

$$J(k) = E[(|y(k)|^p - R_p)^q] \tag{2.58}$$

The coefficients p and q, both positive integers, influence the convergence of the algorithm, creating a specific cost function named (p,q) CM cost function. The CM algorithm shows that the gradient of the dispersion function is zero when R_p is defined by

$$R_p = \frac{E[|s(k)|^{2p}]}{E[|s(k)|^p]} \tag{2.59}$$

being $s(k)$ the zero-memory estimate of $y(k)$. The resulting error signal is as shown

$$e(k) = y(k)|y(k)|^{p-2}(R_p - |y(k)|^p) \tag{2.60}$$

The traditional error signal, used by the LMS algorithm, can be replaced by the one above. The resulting weight vector is given by

$$\omega(k+1) = \omega(k) + \mu e^*(k)x(k) \tag{2.61}$$

The cost function can be reduced, if the p coefficient is equal to 1, to the form

$$J(k) = E[(|y(k)| - R_1)^2] \tag{2.62}$$

being $R1$ presented as

$$R_1 = \frac{E[|s(k)|^2]}{E[|s(k)|]} \tag{2.63}$$

thus altering the weight function to

$$\omega(k+1) = \omega(k) + \mu(1 - \frac{1}{|y(k)|})y^*(k)x(k) \tag{2.64}$$

Mathematical tests prove that the p coefficient provides a faster convergence when it is equal to unity. According to the equations and methods utilized throughout the CM algorithm, it is possible to find some similarities to the LMS algorithm. The desired signal used in the LMS code, $d(k)$, is in the CM replaced by the term $\frac{y(k)}{|y(k)|}$, although $d(k)$ requires a previous knowledge of its characteristics by the system and must be sent from the transmitter to the receiver, something that is not required by the CM method. One important disadvantage of the constant modulus algorithm is its slow convergence speed, which may constitute a severe problem when used in dynamic environments, in which signals must be captured quickly, or when the channel conditions change rapidly. The LSCM algorithm is next presented as a possible solution for this problem, retaining all the advantages CM algorithms already discussed previously.

2.4.5.4 Least Square Constant Modulus Algorithm

Contrary to both the LMS and CM algorithms, which are based on the method of steepest descent, which functions by taking the gradient of the cost function displayed by Equation 2.58, the LSCM algorithm uses the method of non-linear least-squares, also known as the Gauss method, in which a cost function is defined by the weighted sum of the error squares or the total error energy of a finite sample set. This technique confers the LSCM algorithm the ability to converge significantly faster than the previous algorithm. The cost function is as follows

$$C(\omega) = \sum_{k=1}^{K} |\phi_k(\omega)|^2 = ||\Phi(\omega)||_2^2 \tag{2.65}$$

where $\phi_k(\omega)$ is the k^{th} error data sample, $\Phi(\omega)$ is the transpose of the array of all $\phi_k(\omega)$ error data samples and K is the number of data samples of the error energy in one block. The cost function has a partial Taylor-series expansion with a sum-of-squares form, as shown below

$$C(\omega + \Delta) \approx ||\Phi(\omega) + J^H(\omega)\Delta||_2^2 \tag{2.66}$$

where Δ the offset responsible for updating the weights. This offset must be calculated in a way that the sum of squared errors is minimized, which can be accomplished by setting Equation 2.66 to zero, defined as

$$\Delta = -[J(\omega)J^H(\omega)]^{-1}J(\omega)\Phi(\omega) \tag{2.67}$$

By applying the least squares method, the cost function can be rewritten as

$$C(\omega) = \sum_{k=1}^{K} |\phi_k(\omega)|^2 = C(\omega) = \sum_{k=1}^{K} ||y(k)| - 1|^2 \tag{2.68}$$

being $y(k) = \omega^H x(k)$ the array output at k^{th} time sample. In order to guarantee that the system keeps its consisternсy in a dynamic signal environment, normally it is recommended to update the data blocks for each iteration. As such, the ϕ_k error data values can be written as a vector such that

$$\phi(\omega) = \begin{bmatrix} |y(1) - 1| \\ |y(2) - 1| \\ \vdots \\ |y(K) - 1| \end{bmatrix} \tag{2.69}$$

and the Jacobian of the error vector can now be defined as

$$J(\omega) = \begin{bmatrix} x(1)\dfrac{y^*(1)}{|y(1)|} & x(2)\dfrac{y^*(2)}{|y(2)|} & \dots & x(K)\dfrac{y^*(K)}{|y(K)|} \end{bmatrix} = XY_{CM} \tag{2.70}$$

where

$$X = [x(1 + nK) \quad x(2 + nK) \quad \dots \quad x(K + nK)] \tag{2.71}$$

and

$$Y_{CM} = \begin{bmatrix} \frac{y^*(1)}{|y(1)|} & 0 & \cdots & 0 \\ 0 & \frac{y^*(2)}{|y(2)|} & & 0 \\ \vdots & & \ddots & \vdots \\ 0 & 0 & \cdots & \frac{y^*(K)}{|y(K)|} \end{bmatrix} \tag{2.72}$$

Multiplying the Jacobian times its Hermitian transpose is given by

$$J(\omega)J^H(\omega) = XY_{CM}Y_{CM}^H X^H = XX^H \tag{2.73}$$

and the product of the Jacobian times the energy matrix is

$$J(\bar{\omega})\Phi(\bar{\omega}) = XY_{CM} \begin{bmatrix} |y(1) - 1| \\ |y(2) - 1| \\ \vdots \\ |y(K) - 1| \end{bmatrix} = \bar{X} \begin{bmatrix} y^*(1) - \frac{y^*(1)}{|y(1)|} \\ y^*(2) - \frac{y^*(2)}{|y(2)|} \\ \vdots \\ y^*(K) - \frac{y^*(K)}{|y(K)|} \end{bmatrix} = X(y - r)^* \tag{2.74}$$

where r is a hard-limiter acting on y. The weight vector can now be written, as

$$\omega(n + 1) = \omega(n) - [X(n)X^H(n)]^{-1}X(y(n) - r(n))* = [X(n)X^H(n)]^{-1}X(n)r^*(n) \tag{2.75}$$

where

$$r*(n) = \left[\frac{\omega^H(n)x(1+nK)}{|\omega^H(n)x(1+nK)|} \quad \frac{\omega^H(n)x(2+nK)}{|\omega^H(n)x(2+nK)|} \quad \cdots \quad \frac{\omega^H(n)x(K+nK)}{|\omega^H(n)x(K+nK)|} \right]^H \tag{2.76}$$

The initial weights $\omega(1)$ are chosen, followed by the calculation of the complex-limited output data vector $r^*(1)$, continuing to the next weight $\omega(2)$, and so on. This process is repeated throughout n iteration values, until satisfactory convergence is achieved. Further simplification can be applied to Equation 2.75 by defining the array correlation matrix and the correlation vector as

$$\hat{R}_{xx}(n) = \frac{X(n)X^H(n)}{K} \tag{2.77}$$

and

$$\hat{\rho}_{xr}(n) = \frac{X(n)r^*(n)}{K} \tag{2.78}$$

being now the dynamic LSCM weights defined as

$$\omega(n+1) = \hat{R}_{xx}^{-1}(n)\hat{\rho}_{xr}(n) \tag{2.79}$$

The previously presented beamforming algorithms were tested, being the results obtained disclosed in Chapter 6 and subjected to a critical analysis based on their accuracy, convergence speed. Additionally, the hability to track and hold a composite signal afflicted by multipath will be analyzed for the CM and LSCM methods.

Chapter 3

Antenna and Array Design

3.1 Introduction

Antennas are essential devices for any wireless communication system, as these core components are responsible for transmitting and receiving elctromagnetic waves throughout the surrounding environment. Antennas are widely used, ranging from radio and television systems to modern satellite and radar communication systems.

In free space electromagnetic waves travel at the speed of light, experiencing minor losses. However, in environments populated by materials or elements that interact electromagnetically between themselves, waves can suffer reflections, refractions, diffractions or be absorbed. The characteristics of the environment influences speed of which the wave is propagated.

Depending on the intended application antennas can take various forms as to better perform according to the system's requisites. This flexibility is exploited in various scenarios, such as in the automobile industry (monopoles), television reception (Yagi), parabolic antennas, etc. All these various types of antennas can be grouped in three categories: antennas that are constituted by an electric currrent conductive strip, antennas that have embedded apertures that present a specific distribuion of the electric field and, finally, printed antennas that are based on the modification of printed copper lines.

Antennas can also be characterized by their main paramaters, such as radiation pattern, gain, efficiency, directivity, input impedance and bandwidth.

3.2 Essential Antenna Parameters

Radiation Pattern

The radiation pattern of an antenna, also known as antenna pattern, is a graphical representation of the radiation properties of the antenna as a function of space coordinates [3], meaning it offers a concise way to represent how the antenna distributes power over its surrounding area.

Depending on the type of antenna used, radiation patterns can show an isotropic behaviour, characterized by an equal power distribution over the surrounding area of the antenna; omnidirectional traits by having a non directional pattern in a given plane and a directional pattern in any orthogonal plane; and, finally, in cases where the power radiated, or received, by the antenna is more effective in some directions than in others, the radiation pattern is

said to be directive.

In order to accurately characterize the radiation pattern of an antenna it is fundamental to introduce two crucial planes in which said radiation is represented: the horizontal plane ($\theta = 90^{\text{o}}, 0^{\text{o}} \leq \phi \leq 360^{\text{o}}$) and the vertical plane ($\phi = const., 0 \leq \theta \leq 180^{\text{o}}$).

With today's computational tools it is easy to visualize the radiation pattern of an antenna, being even possible to create three dimensional representations, for a more accurate study of the antenna's behavior.

Once defined, the radiation pattern allows the identification of one or multiple main lobes, associated with the directions in which the signal achieves maximum radiation, and also secondary lobes, which, as a way to minimize wasted energy by the system, are best kept to a minimum.

Associated with the pattern of the antenna there is also a parameter that defines the angular separation between two identical points on the opposite sides of the pattern maximum, designated beamwidth. One of the most widely used beamwidths is the Half-Power Beamwidth (HPBW), which is the angle between the two different directions in which the radiation intensity is one-half value of the beam, in a plane containing the direction of the maximum of said beam. Another commonly used beamwidth is the separation between the first nulls of the pattern, referred as First-Null Beamwidth (FNBW).

Directivity

Directivity is a parameter that describes the way an antenna radiates energy, or, in other words, it describes the concentration of radiated energy in a specific direction. An antenna with high directivity concentrates most of its radiated power towards a specific angle. The ratio of the radiation intensity in a given direction provided by a nonisotropic source over that of an isotropic one is known as the directivity of that nonisotropic antenna. This can be expressed mathematically by defining the radiation intensity (U) of an antenna and the radiation intensity of an isotropic antenna (U_0)[3]

$$U(\theta, \phi) = r^2 W_{rad} \tag{3.1}$$

$$U_0 = \frac{P_{rad}}{4\pi} \tag{3.2}$$

where r is the distance, W_{rad} is the radiation intensity and P_{rad} is total irradiated power. Known these parameters, the directivity can be calculated:

$$D(\theta, \phi) = \frac{U(\theta, \phi)}{U_0} = \frac{4\pi U(\theta, \phi)}{P_{rad}} \tag{3.3}$$

If the direction is not specified, the direction of maximum radiation intensity, or maximum directivity, is expressed as

$$D(\theta, \phi) = \frac{U(\theta, \phi)}{U_0} = \frac{4\pi U(\theta, \phi)}{P_{in}} \tag{3.4}$$

Gain

The performance of an antenna is measured by its gain. Gain is the ratio of the intensity of said antenna, in a determined direction, to the ratio intensity obtained if the radiating antenna was isotropic. The radiation intensity provided by an isotropic radiator is equal to the power accepted by it divided by 4π[3]. This can be expressed mathematically as

$$G(\theta, \phi) = \frac{4\pi U(\theta, \phi)}{P_{in}} \tag{3.5}$$

The gain of the antenna is relates closely to the directivty of the antenna, taking also into account its efficiency and directional capabilities.

Antenna Efficiency

In order to estimate the total efficiency of an antenna one must take into account the antenna's losses at its iinput terminals and within its structure, as shown by Figure 3.1.

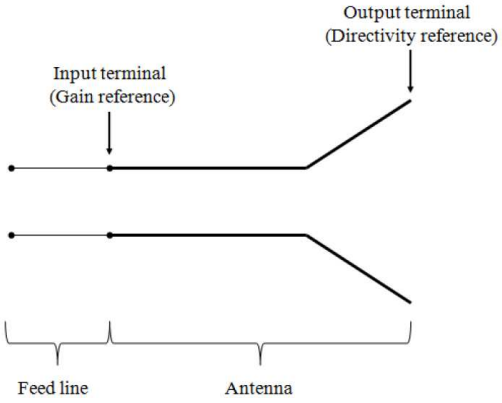

(a) Antenna reference terminals

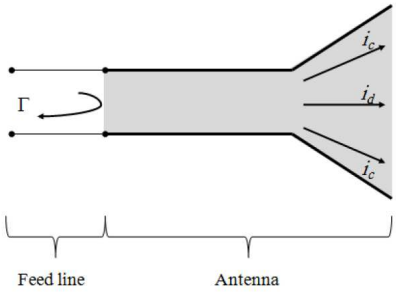

b) reflection, conduction and dielectric losses

Figure 3.1: Reference terminals and antenna losses [3]

Such losses may be due to reflections caused by the mismatch between the field line and the antenna, or may be caused by the conductor or the dielectric material of the antenna. The efficiency of an antenna, η, is represented by:

$$G(\theta, \phi) = \eta D(\theta, \phi) \tag{3.6}$$

meaning it can be calculated by the following relation,

$$\eta = \frac{P_{rad}}{P_{in}} \qquad 0 \leq \eta \leq 1 \tag{3.7}$$

Input Impedance

Input impedance is one of the intrinsic characteristics of an antenna as it is dependent on its geometry, surrounding environment and frequency of operation, since the optimum input impedance can only be achieved for a set frequency range. Since the input impedance of an antenna is highly influenced by such parameters, it can only be determined by simulations or by extensive experimental trials.

The ratio of the voltage to current at the antenna's terminals, with no load attached, defines the impedance of the antenna as

$$Z_A = R_A + jX_A \tag{3.8}$$

The antenna resistance at its terminals,R_A, consists of two components,

$$R_A = R_R + R_L \tag{3.9}$$

being R_A the radiation resistance of the antenna and R_L the loss resistance of the antenna.

Bandwidth

The bandwidth of an antenna is the range of frequencies within which the antenna achieves performance values considered acceptable for a given application or standard[3]. As with all the antenna's frequency dependent characteristics stated previously, the bandwidth can be defined based on these parameters are within an acceptable deviation around the centre frequency. For this thesis the bandwidth is considered as the frequency range for which the return loss (S_{11}) parameter is below -10 dB.

3.3 Types of Antennas

Next are presented the types of antennas developed in this work. Additionally, further information is given regarding their structural and electromagnetic characteristics that served as baisis for the development of said antennas.

3.3.1 Dipole Antennas

Dipoles are one of the simplest, least expensive and most versatile antennas, easily deployable in most applications. These antennas are widely used on their own but can also be incorporated into other antenna designs, being capable of providing a radiating or driven element for the resulting antenna. A dipole antenna can be easily constructed using two metal conductor wires, oriented in parallel and collinear with each, with a center-fed driven element. The frequency current, and the associated voltage, that flows within the two parallel wires along their length vary in a sinusoidal manner, causing an electromagnetic, or radio signal, to be radiated. As such, depending on the length of the radiating element, other peaks and troughs can be created, meaning that many important properties of the dipole antenna (such as impedance, resonant frequency, etc.) are highly dependent on the length of the dipole.

Dipole antennas can be directly fed by a signal source or feed energy that has been picked up by the receiver, transferring this energy to, and/or from, the antenna directly, or remotely, to the commuication device employed. This versatility leaves considerable room for a variety of different antenna formats, depending on the intended application.

3.3.2 Microstrip Antennas

In high-spec wireless communication applications where precise parameters, such as weight, cost, performance and ease of installation, are constraints, the deployment of low-profile antennas is necessary. One such antenna that adapts very well to the demands of the industry is the microstrip antenna. These antennas are low-profile, simple, inexpensive and conformable to planar and non-planar surfaces. Additionaly, microstrip antennas are mechanically robust and very versatile in terms of resonant frequency, polarization, pattern and impedance, which can be tunned by adding loads between the patch and the ground plane, such as pins and varactor diodes.

However, microstrip antennas have considerable operational shortcomings, such as their very low efficiency and power, high Q, poor polarization scan performance, spurious feed radiation and very low frequency bandwidth. In order to overcome of these disadvantages, microstrip antennas may be grouped in clusters, known as arrays[15].

Nowadays microstrip antennas are mainly employed in applications such as mobile communication base stations, space-borne satellite communication systems and mobile communication handset terminals.

3.3.2.1 Substrate

The selection of a proper substrate material is an important task in microstrip antenna design, as it does not only serve as a physical support but it is also directly related to the antenna's core functionality. Selecting a proper substrate is of critical importance as it may allow to overcome some of the microstrip antenna's intrinsic limitations (such as low gain, low efficiency and high return loss) since the permittivity of the substrate is an essential parameter for controlling its bandwidth, efficiency and radiation pattern. In microstrip antenna design thicker substrates with low dielectric constant are preferred, as they provide better efficiency and larger bandwidth.

There exist numerous substrates with many widths and dielectric constants, each suited for very specific applications. In this paper, a substrate of a width of 1.58mm (h), a dielectric constant (ϵ_r) of 2.15 and a tangent loss ($tg\delta$) of 0.0009 was used.

3.3.2.2 Feeding Methods

Various techniques can be employed to feed or excite a microstrip antenna, each with their own advantages and disadvantages depending on the application in which they are used. In this paper only the microstrip line and coaxial probe methods are presented,

Microstrip Line

One excitation method that may be employed for a microstrip patch antenna is the microstripline-line fed, or edge-fed, technique. Typically, the microstrip line feed line comes

in contact with one of the radiating edges of the patch, although there exist cases where the contact is located along its width.

Edge feeding techniques offer so me advantages as it is easy to fabricate, is simple to adjust the antenna's inout impedance, by controlling the inset position, and is a very simple technique to model, if an electrically thin material is used. However, if thicker substrate is used, the modelling of the antenna's performance is not as straightforward since this leads to the increase of surface waves and spurious feed radiation increases, thus limiting the bandwidth[3].

Other widely used method to accurately match an antenna's input impedance is the inset-fed method, in which the feeding line is recessed a determined distance from the patch. This method is used mainly to overcome the high input impedance that the typical microstrip-feed method wields, by introducing the feed line closer to centre of the patch.

Coaxial Probe

Probe feeding a microstrip patch antenna is another excitation method in which a probe, with a determined radius, extends through the ground plane and is connected to the patch, normally soldered to it. The position of the probe provides impedance matching, in a similar fashion as the feed in the microstrip-line fed patch.

Probe-fed patches offer some advantages, namely the fact that antenna's feed network, where integrated circuits that may be employed, are isolated from the radiating elements via ground plane. Also, provides an efficient feed mechanism, since the probe is in direct contact with the antenna and is isolated from the patch, minimizing spurious radiation [15]. However, coaxial probe feeding techniques suffer from problems similar to the ones experienced in microstrip-line feeding ones, since they are more difficult to model and implement and the bandwidth provided is small and difficult to assess, especially for thick substrates where the coupling power can generate relatively high cross-polarized fields.

3.3.2.3 Design Considerations

Microstrip antennas, due to their finite dimension, undergo fringing at the edges of the patch. Fringing is a function of the length of the patch, L, and the height,, h, frequency and the dielectric constant ε_r of the substrate, being it responsible for making the microstrip line look wider electrically when compared to its real physical dimensions[3]. The introduction of variables known as effective dielectric constant (ε_{reff}), effective width (W_{eff}) and effective length (L_{eff}) are used to account for fringing and wave propagation within the line. By definition, the effective dielectric constant is the dielectric constant of the uniform dielectric material immerse in an homogeneous environment so that identical electrical characteristics, particularly propagation constant, can be found on the actual line immerse in a non-homogeneous environment. For most cases, the value of ε_{reff} will be closer to the value of the substarte's actual dielectric constant if ε_r is much greater than unity ($\varepsilon_r >> 1$).

For low frequency values (up to 10GHz) the effective dielectric constant is relatively constant, given by

$$\varepsilon_{reff} = \frac{\varepsilon_r + 1}{2} + \frac{\varepsilon_r - 1}{2}\left[1 + 12\frac{h}{W}\right]^{-1/2} \tag{3.10}$$

where the values W_{eff} and L_{eff} are the electrical width and electrical length of the antenna, respectively.

The physical length of the antenna can be obtained by taking into account the fringing effects, meaning the electric length (L_{eff}) has been extended on each end by a distance of $\triangle L$, which is a function of ε_{reff} and the width-to-height ratio ($\frac{W}{h}$). The physical length is given by [3]

$$L = L_{eff} - 2\triangle L \tag{3.11}$$

and the distance $\triangle L$ can be determined by

$$\triangle L = \frac{(\varepsilon_{reff} + 0.3)(\frac{W}{h} + 0.264)}{(\varepsilon_{reff} - 0.258)(\frac{W}{h} + 0.8)} \tag{3.12}$$

For efficient radiation, the rectangular microstrip patch width is approximately

$$W = \frac{c}{2f_r}\sqrt{\frac{2}{\varepsilon_r + 1}} \tag{3.13}$$

where f_r is the resonant frequency, and c the speed of light.

A microstrip antenna can have multiple functional modes. However, for the dominant TM^x_{010} mode, the resonant frequency of the antenna is a function of its length, normally given by

$$fr = \frac{c}{2L_{eff}\sqrt{\varepsilon_{reff}}} \tag{3.14}$$

which already takes into account fringing.

The input impedance of a microstrip antenna can be approximated by

$$Z_{in} = \frac{60\lambda_0}{W} \tag{3.15}$$

The input impedance of a microstrip antenna, apart from the width W, depends on the point where the antenna is fed. The input impedance Z_{in} is not strongly dependent upon the substrate's height, but it greatly varies along the length of the antenna, since the edges of the antenna function as an open circuit, meaning that the impedance at the edges reaches its maximum, and towards the center of the patch the impedance decreases, reaching a null value (short-circuit).

In order to achieve proper matching between the patch and the microstrip feed line it is necessary to know the point y_0 in which the antenna has a fixed input impedance Z'_{in}, which can be determined by

$$Z'_{in} = Z_{in}\cos^2(\frac{\pi y}{L}) \tag{3.16}$$

3.4 Polarization

Electromagnetic waves are comprised of two, interdependent fields: the electric field and the magnetic field, each orthogonal relative to each other and with varying phases. These fields can propagate through any dielectric at a set velocity, which, in vacuum, corresponds to the speed of light.

Polarization, also referred to as wave polarization, is represented as expression of the orientation electric flux's lines in an electromagnetic field. For wireless communication systems, short-ranged communications achieve better performance when the transmitting and receiving antennas have the same polarization, as the maximum power transfer can be achieved. The least efficient short-range communications usually take place when the two antennas do not have similar polarizations, resulting in partial signal loss and, in extreme cases where the source and destination have orthogonal polarizations relative to each other, can even result in the total loss of the signal.

The polarization of a wave is the polarization of said wave, radiated towards a specified direction in the far field, and having a given power flux density, resulting in maximum available power at the antenna terminals [3].

For cases where the polarization of the receiving antenna is not the same as the polarization of the incoming wave a phenomenon known as polarization mismatch occurs. Due to polarization loss the amount of power extracted by the antenna from the incoming signal is not optimal.

Polarization can be constant, meaning that it retains a particular orientation at all times, or it can rotate with each wave cycle. Thus, polarization schemes can be classified as linear, circular or elliptical.

Linear polarization occurs when the vector that describes the electric field at a point in space as a function of time is always directed along a line. In general, however, the figure that the electric field traces is an ellipse, and the field is said to be elliptically polarized, meaning that linear polarization is a special case in which the ellipse becomes a straight line. The same can be said for circular polarization, when the ellipse becomes a circle. Along with these different polarization schemes, the electric field can be traced in a clockwise (CW), also known as right-hand polarization, or in a counterclockwise (CW) sense, known as left-hand polarization.

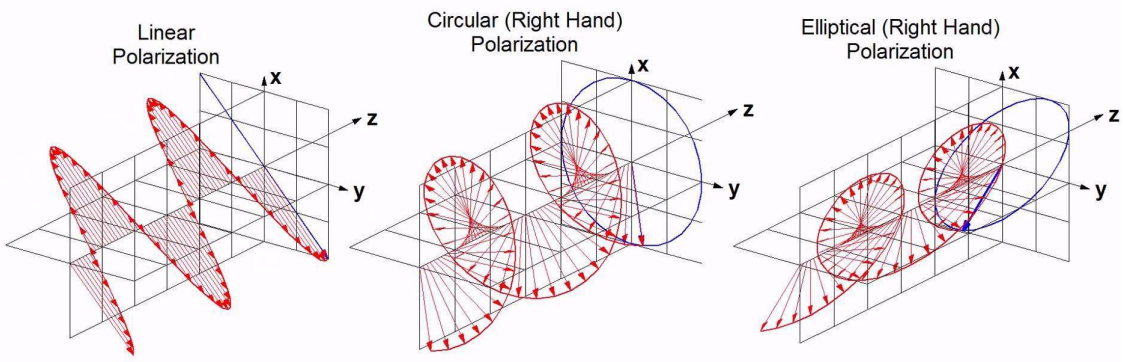

Figure 3.2: Polarization schemes [4]

Linear polarization can be achieved if a wave's electric (or magnetic) field vector is always oriented along a straight line at every instant of time at that point, which can only be accomplished if the field possesses one component, or two orthogonal linear components in time phased or 180^{o}, or multiples of 180^{o}, out-of-phase. Circular polarization can only be achieved if the field vector has two orthogonal linear components with similar amplitude. Additionally, these components must have a time-phase difference of odd multiples of 90^{o} [3].

As referred above, both linear and circular polarizations are particular cases of elliptical

polarization, which can be produced if the tip of the field vector traces an elliptical locus in space and if some necessary conditions that share some similarities to the above polarization schemes are demonstrated: the field must have two orthogonal linear components, with not necessarily the same magnitudes. If the the two components do not share a common magnitude, the time.phase difference between them must not be null or multiples of 180^{o} (violating this criteria would make wave have linear polarization). If the components have equal magnitude, the time-phase difference between them must not be odd multiples of 90^{o} (or the wave would have circular polarization).

3.4.1 Wave Polarization Expressions

The instantaneous field of a plane wave is comprised of two components along $\hat{a}_x$ and $\hat{a_y}$. It can be mathmetically written as[3]

$$\overrightarrow{E}(z,t) = \hat{a}_x E_x(z;t) + \hat{a_y} E_y(z;t) \tag{3.17}$$

being $\hat{a}_x$ and $\hat{a_y}$ the components of the electric (or magnetic) field vector. E_x and E_y are represented by the following expressions:

$$\begin{cases} E_x(z,t) = E_{xo}\cos(wt + kz + \phi_x) \\ E_y(z,t) = E_{yo}\cos(wt + kz + \phi_y) \end{cases} \tag{3.18}$$

where ϕ_x and ϕ_y are the corresponding phases, and E_{xo} and E_{yo} are, respectively, the maximum magnitudes of the x and y components, represented by the complex values

$$\begin{cases} \overrightarrow{E_x} = E_{xo}e^{j\phi_x} \\ \overrightarrow{E_y} = E_{yo}e^{j\phi_y} \end{cases} \tag{3.19}$$

These complex magnitudes can be used to determine the polarization ratio, given as

$$P = \frac{\overrightarrow{E_y}}{\overrightarrow{E_x}} = \frac{E_{yo}}{E_{xo}}e^{j(\phi_y - \phi_x)} = \frac{E_{yo}}{E_{xo}}e^{j\Delta\phi} \tag{3.20}$$

The time-phase difference between the two components, $\Delta\phi$, it is possible to determine both the wave's polarization and the rotation of said polarization, via a simple mathematical equation

$$\begin{cases} \Delta\phi < 0 & \text{Right-hand, or clockwise, polarization} \\ \Delta\phi > 0 & \text{Left-hand, or counterclockwise, polarization} \end{cases} \tag{3.21}$$

In order for a wave to have linear polarization it is necessary, as referred above, that the time-phase difference between the two components be null or multiples of 180^{o}, represented as

$$\Delta\phi = \phi_y - \phi_x = n\pi, \quad n = 0, 1, 2, ... \tag{3.22}$$

thus resulting in a purely real polarization ratio$P = const.$

On the other hand, circular polarization can only be achieved when the magnitudes of the two components are similar ($|E_x| = |E_y|$) and the time-phase difference between them is odd multiples of $\frac{\pi}{2}$, meaning

$$\Delta\phi = \begin{cases} +(\frac{1}{2}+2n)\pi, & n=0,1,2... \quad \text{for clockwise polarization} \\ -(\frac{1}{2}+2n)\pi, & n=0,1,2... \quad \text{for counterclockwise polarization} \end{cases} \tag{3.23}$$

resulting in a purely imaginary polarization ratio given by $P = e^{\pm j\frac{\pi}{2}} = \pm j$.

For cases when none of the conditions mentioned above are met, the wave has elliptical polarization.

3.4.2 Axial Ratio

The axial ratio is another fundamental parameter used to characterize the polarization of the waves radiated by an antenna. Although it cannot analyze the shape traced by the field, axial ratio is an important parameter, essential to deduce some important polarization characteristics. Axial ratio can be defined as the ratio of the orthogonal components of a field (electric or magnetic), represented as[3]

$$AR = \frac{\text{major axis}}{\text{minor axis}} = \frac{\text{OA}}{\text{OB}}, \qquad 1 \leq AR \leq \infty \tag{3.24}$$

$$AR = \begin{cases} 1 & \text{Circular polarization} \\ \infty & \text{Linear polarization} \\ \textit{other} & \text{Elliptical polarization} \end{cases}$$

The quality of a wave's polarization is commonly quantified by the axial ratio, which is normally expressed in dB as

$$AR_{dB} = 20\log(AR) \tag{3.25}$$

In order to achieve acceptable circular polarization it is necessary, for most applications, to have an axial ratio below 3dB. In order to achieve optimum circular polarization, the axial ratio value should be 0dB.

3.4.3 Circular Polarization

Linear polarization, albeit being easy to implement, is normally discarded in favor of circular polarization in several radar and satellite communication systems, as the latter is able to overcome propagation anomalies, ground reflections and the effects caused by the spinning motion of satellites[18].

Circular polarization is achieved if two orthogonal modes are excited with a 90^{o} time-phase difference between them. Patch antennas offer great design flexibility and a myriad of design techniques that can be employed in order to obtain circular polarization, such as adjusting their physical dimensions and by using one, or several, feeds. Among the multiple feed designs, the patch antenna driven through power dividers and through 90^{o} hybrids are particularly relevant.

To overcome the complexities inherent in multiple feed arrangements, circular polarization can also be achieved with a single feed. One way to accomplish this is to feed the patch at a single point to excite two orthogonal degenerate modes (of some resonant frequency) of ideally equal amplitudes and forcing a 90^{o} phase difference between these two modes by introducing proper asymmetry in the patch antenna's structure.

3.5 Antenna Arrays

Normally the radiation pattern of a single element is relatively wide, and each element provides low values of directivity and gain. In many applications it is necessary to design antennas with very directive characteristics to meet the requirements imposed by long distance communication systems. One way to accomplish this is to increase the electrical size of the antenna. This increase may be done directly to one element or can be achieved bygrouping a set of radiating elements in an electrical and geometrical configuration, referred to as an array, comprised of, normally, identical elements. This method is normally preferred as it is often more convenient, simpler and more practical, giving a finer control over the radiation pattern of the antenna.

The total field of the array is determined by the addition the fields vectors radiated by each individual antenna, assuming that the current supplied to each radiating element is the same as that of an isolated element. This characteristic normally depends on the separation between the elements, in order to provide very directive patterns, being necessary that the fields from the array interfere constructively in the desired directions and destructively in the remaining space. The resulting radiation pattern of the antenna array is dependent on some factors such as the geometrical configuration of the overall array (linear, circular, rectangular, spherical,...), the relative displacement between the elements, the excitation amplitude, phase and pattern of each of the individual elements that constitute the array[3].

3.5.1 Uniform Linear Array

An uniform linear array is comprised of an array of identical, evenly spaced elements, arranged in a linear manner, all of identical magnitude and each with progressive phase.

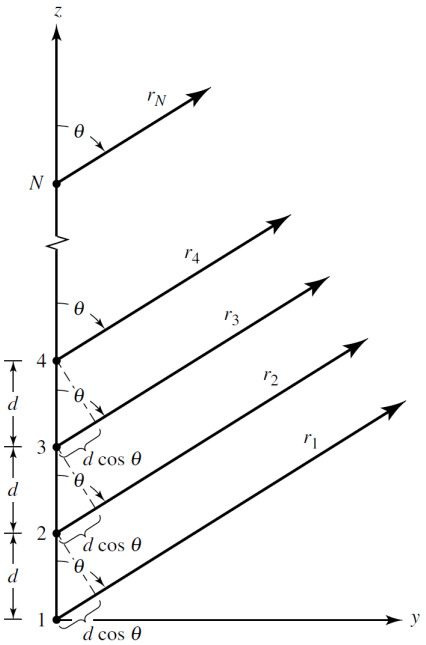

Figure 3.3: N-element uniform linear array positioned along the zz axis[3]

The array factor of an uniform linear array can be obtained by considering the elements of the array as isotropic point sources. If the elements are not isotropic sources, the total field can be formed by multiplying their corresponding array factor by the field of a single element. This pattern multiplication can only be applied for arrays of identical elements and is used to determine the overall array pattern of the linear array.

When a isotropic source is excited by a current $\mathbf{I}$ it radiates an field E, represented by

$$E = I\frac{e^{-j\beta r}}{4\pi r} \qquad \mathbf{I} = Ie^{j\phi} \tag{3.26}$$

For the particular case where a uniform linear array is used, the current of each radiating element is represented as

$$\mathbf{I}_1 = Ie^{j\phi_1}; \quad \mathbf{I}_2 = Ie^{j\phi_2}; \ldots \mathbf{I}_{N-1} = Ie^{j\phi_{N-1}}; \quad \mathbf{I}_N = Ie^{j\phi N}$$

with the relation

$$(\phi_2 - \phi_1) = (\phi_3 - \phi_2) = \ldots = (\phi_N - \phi_{N-1}) = \alpha$$

For each element of the array, the radiated field is given by

$$E_1 = Ie^{j\phi_1}\frac{e^{-j\beta r1_1}}{4\pi r_1}; \quad E_2 = Ie^{j\phi_2}\frac{e^{-j\beta r_2}}{4\pi r_2}; \ldots E_N = Ie^{j\phi_N}\frac{e^{-j\beta r_N}}{4\pi r_N}; \tag{3.27}$$

Simplifying

$$\phi_2 = \phi_1 + \alpha;$$

$$\phi_3 = \phi_2 + \alpha = \phi_1 + 2\alpha;$$

$$\phi_N = \phi_{N-1} + \alpha = \phi_1 + (N-1)\alpha$$

For far-field radiation, where $r >> d$, assuming a near planar wave front, the phase of the N radiating elements is given by

$$\theta \cong \theta_1 \cong \theta_2 \cong \ldots \cong \theta_N$$

and the respective amplitude is represented as

$$r_2 = r_1 - d\cos\theta$$

$$r_3 = r_2 - d\cos\theta = r_1 - 2d\cos\theta$$

$$r_N = r_{N-1} - d\cos\theta = r_1 - (N-1)d\cos\theta$$

thus corroborating that

$$r_1 \cong r_2 \cong \ldots \cong r_N$$

As referred above, the resulting field of the antenna array is the superposition of the various fields generated by each individual element, meaning

$$E_T = \sum_{n=1}^{N} E_n \tag{3.28}$$

Finally, by integrating the elements of Equation 3.27 into Equation 3.28, the mathematical expression takes the following form

$$E_T = Ie^{j\phi_1}\frac{e^{-j\beta r_1}}{4\pi r_1}[1 + e^{j(\beta d\cos\theta+\alpha)} + \ldots + e^{j(n-1)(\beta d\cos\theta+\alpha)} + \ldots + e^{j(N-1)(\beta d\cos\theta+\alpha)}] \tag{3.29}$$

where $Ie^{j\phi_1}\frac{e^{-j\beta r_1}}{4\pi r_1}$ is the element factor and the sum of the exponential values is the array factor.

This proves that the element factor is the radiation pattern of an isotropic source and that the array factor is a function of the number of the N elements that constitute the array, the distance between them and the relative phase α.

In a more condensed form, the array factor can written as

$$AF = \sum_{n=1}^{N} e^{j(n-1)(\beta d\,\cos\theta+\alpha)} \tag{3.30}$$

or, since the array factor is a geometric progression of N elements, by simplifying and normalizing, so that the maximum value is equal unity, can be written as

$$|AF|_n = \frac{1}{N}\left[\frac{\sin(\frac{N}{2}\psi)}{\sin(\frac{\psi}{2})}\right] \qquad \psi = (\beta d\,\cos\theta + \alpha) \tag{3.31}$$

or it can even be written relatively to the radiation pattern's main lobe, meaning for low values of ψ, as

$$|AF|_n = \frac{\sin(\frac{N}{2}\psi)}{N\frac{\psi}{2}} \qquad \psi = (\beta d\,\cos\theta + \alpha) \tag{3.32}$$

Array Factor Characteristics

The array factor, besides varying with the radiating elements separation and relative phase, also changes according to the number of radiating elements present in the array. As the number of elements increases:

- The main lobe narrows, making the radiation pattern more directive;
- The number of lobes increases;
- The number of secondary lobes decreases.

Maxima The main lobe maximum in Equation 3.32 occurs when the denominator term $\frac{\psi}{2} = 0$. Thus

$$\beta d \cos\theta_{max} + \alpha = \pm 2m\pi \Rightarrow \theta_{max} = \pm cos^{-1}\left(\frac{\lambda\beta}{2\pi d}\right) \quad m = 0, 1, 2, ... \tag{3.33}$$

which the observation angle that makes $\psi = 0$.

The sidelobe maxima occurs approximately when the numerator is a maximum. This occurs when the numerator argument is $\frac{N\psi}{2} = \pm(2n+1)\frac{\pi}{2}$. Thus

$$\theta_s = \pm\frac{\pi}{2} - sin^{-1}\left\{\frac{\lambda}{2\pi d}\left[-\beta \pm \left(\frac{2s+1}{N}\right)\pi\right]\right\} \qquad s = 1, 2, 3, ... \tag{3.34}$$

Nulls From Equation(3.32), the array nulls occur when the numerator argument is $\frac{N\psi}{2} = \pm n\pi$. Thus, the array nulls are given when

$$\theta_{null} = \frac{\pi}{2} - sin^{-1}\left(\frac{1}{2\pi d}\left(\pm\frac{2n\pi}{N} - \beta\right)\right) \qquad n = 1, 2, 3, ... \tag{3.35}$$

Since the $\sin(\theta_{null}) \leq 1$, for real angles, the argument in Equation 3.35 must be ≤ 1. Thus, only a finite set of n values will satisfy the equality.

Beamwidth The beamwidth of a linear array is determined by the angular distance between the half-power points of the main lobe. The two half power points are found when the array factor is -3dB. By using the array approximation presented by Equation 3.32, the calculation of the beamwidth can be simplified and given by

$$\theta_{-3dB} = \frac{\pi}{2} - sin^{-1}\left(\frac{1}{2\pi d}\left(\frac{\pm 2.782}{N} - \beta\right)\right) \tag{3.36}$$

The half-power beamwidth can be found once the angles of the first maximum (θ_m) and the half-power point (θ_h) are determined. For a symmetrical pattern

$$HPBW = 2|\theta_m - \theta_h| \tag{3.37}$$

where θ_m is given by Equation 3.33, or simply

$$HPBW = |\theta_2 - \theta_1| \tag{3.38}$$

where θ_2 and θ_1 are the two half-power points, given by Equation 3.36.

Chapter 4

RFID Systems

4.1 Introduction

RFID (or Radio Frequency Identification) systems employ a technology capable of non-contact or line-of-sight reading of data from electronic labels, wirelessly. The link between these labels and the RFID transceiver is achieved using electromagnetic signals, thus making these systems particularly useful for tracking and tagging applications, such as in manufacture halls, where bar code labels may not retain their integrity, due to the harsh environment, or even in cases where there is no physical contact or line-of-sight between the tag and the transceiver. RFID is today one of the most employed technologies in automated data collection, identification and analysis systems worldwide, steadily reaching new development milestones in areas such as reading range, larger memory capacity and data transmission security [19, 6].

4.2 History and Genesis of RFID

RFID technology, even though it generated great interest for research purposes throughout recent years, started its development around the World War II period, based on the radio detection and ranging system, known as RADAR, projected by a Scottish physicist named Robert Alexander Watson, in 1935. The main purpose of radar systems was to pinpoint the range, altitude, direction or speed of both moving and fixed objects via the use of electromagnetic waves, and it was used primarily to identify incoming airplanes by Germans, Americans, Japanese and the English. Albeit being a reliable asset, there was major shortcoming of this approach: the impossibility of distinguishing friendly from enemy aircraft. The Germans discovered that a secret handshake could be established if their planes rolled as they were approaching their base, by modulating the reflected radar signal, that could be used to identify incoming units. This marked a major milestone in tagging and tracking development, being this considered the very first passive RFID system. The first active Identify Friend or Foe system was created by the British, with close collaboration with Robert Alexander Watson-Watt. Resorting to transmitters installed on every British plane, it was possible, upon detecting a radar signal, to broadcast back a signal capable of identifying friendly units. The same principle is employed by most recent RFID systems. The reader (interrogator) sends a signal to a transponder (tag) which reflects back the received signal (passive RFID) or broadcasts a signal back to the reader (active RFID) [20]. The research and interest put on this technology led, from early on, to new milestones, being some of the most notable the following:

- James Clark Maxwell, a Scottish physicist, originated, in 1864, the concept of electromagnetic radiation, as its field equations, which led Albert Einstein to develop his theory of relativity;
- In 1887, a German physicist, named Heinrich Rudolf Hertz, derived the Maxwell's equations by a new method, casting them in the modern form used today. Hertz demonstrated also that the nature of the reflection and refraction of electromagnetic waves obeyed Maxwell's equations;
- In 1896, Italian physicist Guglielmo Marconi was granted a patent for a successful system of radio telegraphy, which led to the very first transatlantic wireless communication;
- Harry Stockman, in 1948, published a paper entitled *"Communication by Means of Reflected Power"* which introduced the reflected power-coded communication concept;

Major advancements in the RFID technology field occurred during the 50's, mainly with the contributionsof F.L. Vernan and D. B. Harris, as the first patent was lodged for passive transponders and, in 1973, a "passive radio transponder with memory" was created by Mario Cardullo, the first true ancestor of the modern RFID systems. In 1979 RFID technology was already vastly adopted and used commercially for animal tracking in the United States, followed by motor vehicle toll collection in Norway, in 1987, and by RFID tracking of the US rail cars, in 1994. Another boost was given to RFID, in 1999, at the Massachusetts Institute of Technology that, in 2003, with the creation of an Auto ID centre, marking the birth of the EPC system, designed to replace bar-codes (UPC) [19].

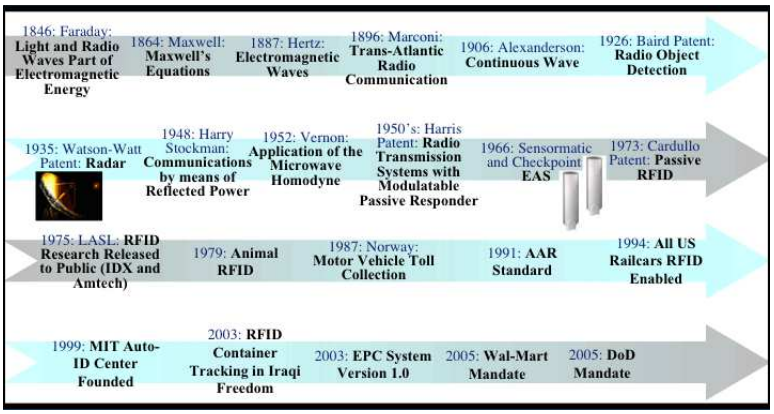

Figure 4.1: Evolution of RFID [5]

RFID technology reached a relatively matured and reliable stage. It is, though, constantly evolving, reinforcing the need to continue its development in order to achieve better, more cost-effective deployments of these systems worldwide.

4.3 Basic Components

RFID systems are comprised of three basic components, as listed bellow[7]:

- **A tag**, also known as transponder, which is located on the object to be identified and represents the data-carrying device of the system. It is comprised by a semi-conductor

chip, (where the data may be stored, read from and, sometimes, written, in addition to some important circuitry), an antenna and, sometimes, a battery;

- **An interrogator**, or reader, which, depending upon the design and the technology used, may be a read or write/read device. It is composed of an antenna, an RF electronics module (transmitter and receiver), a control module and a coupling element to the transponder. Additionally, many readers are equipped with additional an interface (RS 232, RS 485, etc.) to enable them to forward the received information to another system (PC, robot control, system, etc.) [19];

- **A controller**, or host, in form of a PC or a workstation, that runs database and control software (middleware).

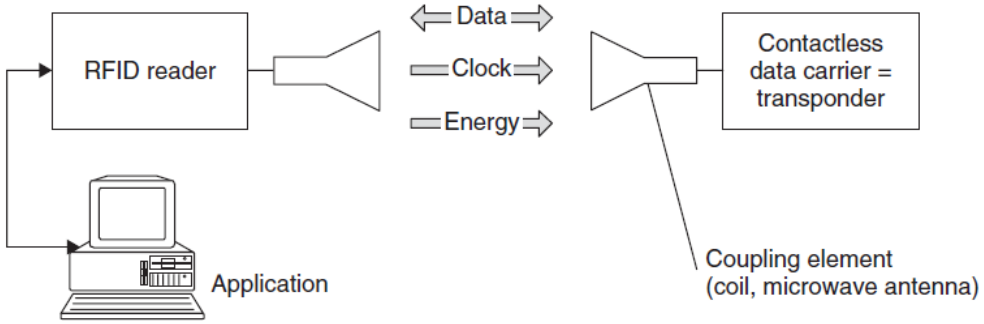

Figure 4.2: Main components of a RFID system [6].

A RFID system may consist of numerous interrogators, spread across various areas such as warehouse facilities and along assembly lines, capable of establishing a communication link with a tag when it enters the interrogator's read zone, via EM waves. The read zone is defined by the radiation pattern, polarization and gain of the reader's antenna, which is crucial for the correct functioning of the interrogator[19]. Various types of information can be exchanged within this systems, as tags can hold the tagged object's serial number, time stamp, configuration instructions, only referring a few: Depending of the configuration of the transponder, the established link can be described as being passive or active. Further characteristics and parameters related to RFID systems will be addressed moving forward.

4.4 Applications, Security and Commercial viability

In modern days, RFID systems have raised interest in the industry as a cost-effective technology, largely due to extensive use and deployment by Wal-Mart and the american Department of Defense. In 2003, aiming to enable pallet-level tracking of inventory, Walmart issued, to its top 100 suppliers, the tagging of all pallets and cases by January 1st, 2005, with Electronic Product Code (EPC) labels, practice quickly followed by Department of Defense[7]. The early transition towards "silent commerce" adopted by these two companies represent the future of the industry on a global scale, in which Auto ID technologies would be widely deployed. Auto ID is a preprogrammed, high efficiency, low cost data collection system, developed to relay data received from objects to a database management systems, with minimal

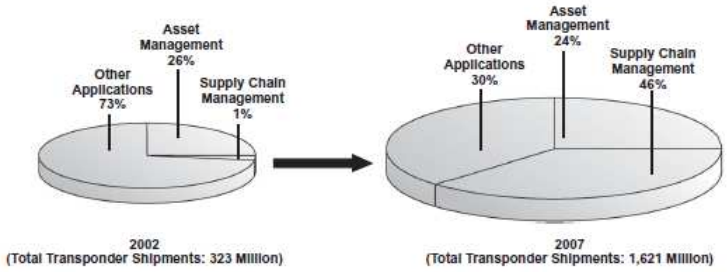

Figure 4.3: RFID Transponder Shipments, 2002 vs 2007 [7]

human intervention. This autonomous, self-sufficient systems are attractive to different business applications and attracted a lot of attention in recent decades[19].

One of the most used Auto ID deployments throughout the world is the bar-code. In contrast to RFID tags, in which a small radio-power microchip is embedded, bar-coded labels are pieces of paper with varying thicknesses of black lines. The recent shift of interest of the industry to RFID is due to, mainly, the limited memory storage capacity and subpar "line-of-sight" operations provided by the bar-code approach. Other advantages offered by RFID technology is its the reliability in moisture, noisy, or dirty environments, providing greater tag reading flexibility in a wider scanning area. However, though RFID tags remove the "line-of-sight" barrier and, thus, removing human interaction in the reading process, these tags require a silicon chip to store data, making the cost of implementation in the Auto ID market much more expensive.

Different forms of Auto ID are developed in order to ensure that each and every item can be tracked in any process, such as manufacturing, supply chain, logistics, quality control, inventory management, among many other applications. Health care and pharmaceutical, document management, sports, livestock, baggage handling, finance, and access control are only some the various possible applications in which this technology can be found[19]. To stay competitive in a global market, manufacturers need react quickly to changes to their business environments, which are accelerated through new trends, and must adapt their supply chain accordingly. Costumers increasingly ask for more individualized products, incentivizing trends towards mass customization and smaller lot sizes, pushing manufacturers to permanently innovate and rethink their services. On the other hand, manufacturers depend heavily on their supply network and need to foresee and prevent any eventual delays in the delivery of their supply parts.

This dependence has steadily increased during the last years due to the pressure for cost reduction and lean manufacturing, prohibiting large warehouses that could buffer delays. To keep pace with the highly dynamic environment of the manufacturers, IT systems and application software had to become more flexible and less monolithic as it once was, which made service-oriented architectures the standard for businesses worldwide.[21]. These changes gave RFID momentum, bringing potential to change the way planning and scheduling was done[8]:

- The high level of control, as well as the improved information handling and automation within manufacturing plants given by RFID systems, is almost unlimited. The ability to have manufacturing plant and supply chain wide visibility of objects identified with tags allows for large amounts executable instructions and information to be assigned to an object. The tagged item can be traced and scanned, along the production line,

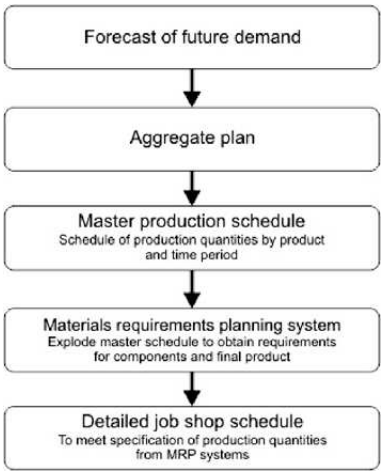

Figure 4.4: Hierarchy of Production Decisions [8]

downloading precise instructions from databases into computer numeric control machines automatically, facilitating the production of custom products;

- The capability of handling a continuous flow of data, autonomously and permanently, is another major achievement by RFID, and is crucial to give businesses a competitive edge. This improved sensing capability provides critical subsystems with the possibility to apply real-time, advanced algorithms, such as math programming and heuristics. This allows businesses to overcome an important weakness, transitioning from large amounts of hours of manual production balancing to relying upon advanced, self-sufficient system to achieve maximum production capacity.

The repetitive writing and retrieval of data originates an information ecosystem with minimal human intervention, ideal for the industry worldwide. RFID technology thus provides ease of use and great application flexibility, rising as a major topic of research in these current years.

The growth of this tracking and tagging methodology developed not without the rise of some importance ethic concerns. Abusive and/or malicious uses of these systems can compromise individual privacy via sensitive data probing, making those involved in information technology security concentrate on the reinforcement of protective classified data. Secure solutions for RFID systems normally give primary importance to physical assets instead to the actual data, since organizations can suffer tremendous losses, even though the data may not be affected. Duplication of RFID cards is another major concern as it does not affect the database, but the same access and privileges are assigned to the counterfeit card as the original card holder. These attacks may take several forms and serve many purposes, from stealing a single object to prevent sales at a store, or at a chain of stores, or to place misinformation in a competitor's backend database. All this can be accomplished by the manipulating data on the tag, manipulating middleware data, and attacking the data at the backend[22].

These threats can not, however, overstate the importance that RFID plays in our current life style and, even though this technology carries an inherent risk, the prevention of abusive and, sometimes, criminal use of these systems ultimately fall upon the moral and ethical conduct of the community, and how it wishes to prepare itself for the future challenges presented by new technologies.

4.5 RFID Platform Structure

RFID systems classifications presented cover only a small portion of a very vast array of existent parameters and guide lines intrinsic to this technology.

4.5.1 RFID Transponders

Tags can be classified into passive, active and semi-passive depending on their the built-in power source.

4.5.1.1 Passive tags

Passive tags do not have an embedded power source for operating the IC. Instead, they harvest the energy needed from electromagnetic field generated by their internal circuits, meaning that when there is no communication between reader and tag the circuit is "off". The power transmitted by the interrogator starts the communication process and is utilized for both powering the tag's IC and to communicate back to the reader. This communication method negatively impact the system's reading range when the tag's energy cost is high, thus creating the necessity to develop tags with simple, low consumption circuitry. Passive tags are chosen primarily for their long usable lifetimes, that normally ends with the lifetime of the item, reduced dimensions and cheap deployment costs, being the trade-off the limited data storage capacity[19].

Figure 4.5: Common use of passive tags [9]

The principal components of passive tags are a microchip and an antenna. This microchip has an embedded power rectifier that converts the RF signal from the transponder to DC power. The tag also integrates a clock extractor, a modulator, a logic unit, responsible for the implementation of communication protocols between reader and tag, and an internal memory, for data storage. The antenna, besides the basic functions of transmitting and receiving data, feeds the tag with the energy extracted from the reader's signal, and is the component that dictates the tag's dimension, as it can assume several formats depending on the application, carrier frequency, etc. of the system.

4.5.1.2 Semi-Passive tags

Also called battery assisted tags (BATs), semi-passive tags have an on-board power source, used to keep the IC functioning, but not to assist in radio signal transmission. The commu-

nication between reader and tag are made by backscatter coupling. These tags do not have active transmitters, thus not contributing to any radio noise. Semi-passive tags have increased data storage capacity over passive tags, however they are bigger, more expensive, heavier and have a considerable shorter life span, depending on the size and quality of the battery, that, under harsh environments, may fail, rendering the tag useless.

Figure 4.6: Semi-passive tags used in automobile circulation [10]

4.5.1.3 Active tags

Active tags have an on-board battery, that supplies power to both the IC, and the transmitter. When the tag needs to exchange data with the interrogator, it uses its battery to power up the circuitry responsible for transmission process, circumventing the interrogator reliance problem, experienced by the other transponders, to transmit its data by backscatter coupling. These tags can also act as a interrogator and have ICs capable of data processing and on-board environmental sensors, as well as the highest memory capacity among the three tag groups. Because of these characteristics, active tags can communicate with less powerful interrogators and can transmit information over much longer distances, as they can accept data, process and broadcast it from other tags/sensors. Since a battery is embedded within the tag, the antenna does not need to have the same dimensions as the ones present in passive transponders, being even possible to embed it in the tag's RF module. Active tags synthesize a carrier signal, using a local oscillator and crystal reference, so it can communicate within a specific frequency band even in the presence of other tags, by using different channels. Like the passive and semi-passive, active tags can use amplitude modulation, but it can also transmit and demodulate more sophisticated phase-based modulations (phase-shift keying (PSK), frequency-shift keying (FSK), and quadrature amplitude modulation (QAM)), which offer superior noise cancellation capabilities and better spectral efficiency[23]. This superior performance and capability comes at a cost of higher circuit complexity and larger dimensions, a short life span, of two to seven years[7]. The inclusion of the battery itself as well as the maintenance costs required for the proper functioning of the hardware is substantial, reaching up to 100 times the passive transponder costs.[24, 6]

The battery consumption can be reduced by using a built-in "sleep" mode. It can be programmed to periodically trigger data exchanges with the transponder, favouring the tag's longevity, which is ideal for Real-Time Location Systems (RLTS).

4.5.1.4 Overview

Table 4.1 provides a summary of the information discussed presviously regarding the defining characteristics of the different tag groups.

Figure 4.7: RFID active tag [11]

4.5.2 Coupling

Coupling is an important differentiation criteria for RFID systems, as it defines the way transponders communicate their information to the interrogator. Depending on the intended application, different coupling methods can be employed, such as backscatter, capacitive or inductive coupling, which will affect the range, the frequency and the hardware requisites of the system.

The range of RFID systems can be categorized into three groups:

- **Close range**, or close coupling, systems have a very small range (within 1 cm region), operating, theoretically, at any desired frequency between DC and 30MHz. In order to operate, the transponder must be, either inserted into the reader, or positioned upon a surface provided for this purpose, making these systems particularly useful in applications that are subject to strict security requirements but do not require a large range functionality.

- **Remote coupling** systems have a write and read range between 1cm and 1 m. These are the most widely deployed of all RFID systems currently sold, used in such applications as smart cards, animal identification and industrial automation[25]. These include proximity coupling and vicinity coupling systems.

- **Long range** systems have a range significantly above 1m. These systems operate at the UHF frequencies of 868MHz (Europe) and 915MHZ (USA) and at the microwave frequencies of 2.5GHz and 5.8GHz.

Of these types of RFID coupling, magnetic and capacitive types are normally used for close range links, inductive coupling for remote links and RFID backscatter coupling for long range links.

4.5.2.1 Capacitive Coupling

RFID capacitive coupling is mainly used for short ranges, where close coupling is needed, existing also systems that employ capacitive coupling for remote coupling (Motorola Inc.,

Tag Type => Tag Characteristic || V	Passive	Semipassive	Active
Power source	No power of its own; receives power from the reader's signal	Has its own power source (battery)	Has its own power source (battery)
Communication	Communication must be initiated by the reader	Communication must be initiated by the reader	Can respond to the reader's signal and can also initiate the communication
Size	Small Could be as small as (0.15 mm × 0.15 mm) × 7.5 m	Medium	Largest, typically (1.5 × 3) × 0.5 inch^3
Read range	Short 2 mm; few meters depending on the operating frequency	Up to 100 m	Large (up to 1 Km is possible); some limitations apply, resulting from standards and regulations
Memory design	Read only (RO), write once/read many (WORM), or read/write (RW)	Read only (RO), write once/read many (WORM), or read/write (RW)	Read only (RO), write once/read many (WORM), or read/write (RW)
Memory capacity	Mostly up to 128 bits, but some tags can have memory up to 64 KB	—	Up to 8 MB
Cost	Inexpensive	Intermediate	Expensive

Table 4.1: Defining features of the different tag groups [12]

1999). As the name implies, capacitive effects are used to provide coupling between the interrogator and the transponder, relying electrodes, present on the plates of the capacitor, instead of coils or antennas. The capacitance between the interrogator and tag provide the means through which the signal can be transmitted. being the generated AC signal from interrogator utilized to energize the transponder's internal devices, allowing it to rectify and return the signal back to the interrogator.

4.5.2.2 Inductive Coupling

Inductive coupling is the most used remote coupling system. Inductive coupling operates by transferring energy from the interrogator to the tag via mutual inductance. In order to achieve inductive coupling, both the antenna and the tag must be equipped with "antenna" coils. When the tag is placed close enough to the interrogator, the field from the interrogator coil will couple the coil from the tag, inducing a voltage in the tag that is used to rectify and power the tag's circuitry. To enable the information from the tag to be transmitted to the interrogator, the tag changes the coil's load, which will be detected by the interrogator as a result of the mutual coupling.

4.5.2.3 Backscatter Coupling

RFID backscatter coupling is used mainly by long range-systems. This method "reflects" back an altered signal, originated by the interrogator, by the tag, using some of the power harvested during the communication process, by changing its antenna's load or by changing some of its properties.

Depending on the tag's properties, like its cross sectional area, the way that the signal is reflected back is changed. Typical ranges of 3 meters can be achieved by using passive (battery-free) backscatter tags, while active (battery-supported) tags support a range of 15 meters or more. The battery of active backscatter tags is used exclusively to supply the microchip and for the retention of data, being the electromagnetic field from the interrogator used to power data transmission between the reader and the tag. In order to allow parallel data transmission and reception, directional couplers are often used. Additionally, the interrogator must be able to detect the tag's modulation, independently of other reflections generated from other hosts, although these will normally be stable and not modulated in any way.

4.5.3 Frequency of Operation

There exist many frequency bands that may be used by RFID systems. The frequency used is an important early development decision, since it will determine many of the characteristics and factors (both internal and external) about the way the system will operate. Frequencies around 900 MHz (UHF) are commonly used for supply management applications and warehouse management applications[14], being this frequency band the one utilized during the development of this thesis .

There exist four different RFID frequency bands, used worldwide, that enable the right system parameters to be obtained depending of the purpose of the application used.

There exist different restrictions for UHF frequencies in different countries. These frequencies cannot be used internationally due to allocation limitations imposed worldwide.

This thesis focuses on development of a smart antenna system functioning within the american RFID band, as all the hardware developed throughout this project was previously subjected to simulation tests for frequencies approximate to 915MHz.

RFID Frequency Band / Spectrum Allocations			
RFID Frequency Band	**Frequency Band Description**	**Typical Range**	**Typical RFID Applications**
125-134.2 kHz and 140-148.5 kHz	Low frequency	Up to ~ 1/2 metre	These frequencies can be used globally without a license. Often used for vehicle identification. Sometimes referred to as LowFID.
6.765 - 6.795 MHz	Medium frequency		Inductive coupling is used on these RFID frequencies.
13.553 - 13.567 MHz	High Frequency HF Often called 13.56 MHz	Up to ~ 1 metre	These RFID frequencies are typically used for electronic ticketing, contactless payment, access control, garment tracking, etc
26.957 - 27.283 MHz	Medium frequency	Up to ~ 1 metre	Inductive coupling only, and used for special applications.
433 MHz	UHF		These RFID frequencies are used with backscatter coupling, for applications such as remote car keys in Europe
858 - 930 MHz	Ultra High Frequency UHF	1 to 10 metres	These RFID frequencies cannot be accessed globally and there are significant restrictions on their use. When they are used, it is often used for asset management, container tracking, baggage tracking, work in progress tracking, etc. and often in conjunction with Wi-Fi systems. For further information on its use see the paragraph below.
2.400 - 2.483 GHz	SHF		Backscatter coupling, but only available in USA / Canada
2.446 - 2.454GHz	SHF	3 metres upwards	These RFID frequencies are used for long range tracking and with active tags, RFID and AVI (Automatic Vehicle Identification). Backscatter coupling is generally used.
5.725 - 5.875 GHz	SHF		Backscatter coupling. Not widely used for RFID.

Table 4.2: RFID Frequency bands [13]

UHF RFID Frequency Band Details	
Country	**Restrictions**
North America	Here the UHF RFID band can be used unlicensed within the limits of 915 MHz ± 15MHz (i.e. 902 - 928 MHz). There are restrictions on transmission power.
Europe (less exclusions)	Within this region, the RFID frequencies (and other low-power radio applications) specified ETSI recommendations EN 300 220 and EN 302 208, and ERO recommendation 70 03. These allow RFID operation within the band 865-868 MHz, but with some involved restrictions. RFID readers must to monitor a channel before transmitting - "Listen Before Talk".
France	The North American standard is not accepted within France as it interferes with frequencies allocated to the military.
China and Japan	There are no licence free RFID bands or frequencies. However it is possible to request a licence for UHF RFID which is granted in a site basis.
Australia & New Zealand	Within this area the RFID band exists between 918-926 MHz as these frequencies are unlicensed, but there are restrictions on the transmission power.

Table 4.3: Some Frequency band limitations worldwide [13]

Chapter 5

Hardware Development

In this chapter, the first section presents the develpomet process of the microstrip antenna, from the early simulation stages to the creation of the final circularly polarized antenna array. The measurements, both simulated and tested, are presented and discussed. Additionally, the steps taken during the development of an early prototype board used in this project. The board in question was then used as a base for the construction of a more compact and integrated board. The following chapter, along with a detailed overview of the implemented hardware and layout considerations, includes block diagrams and references schematics in order to provide a better understanding of the differentiating characteristics and (dis)advantages of these two implementations and how they integrate the overall smart antenna setup.

5.1 Antenna Design

The microstrip patch antenna that was developed in this work is made of a 1.598mm thick FR4 laminate with thin layers of copper on both sides of the dielectric (approximately 35μm thick). Since low-cost FR4 substrates introduce some additional complexity to the antenna design, due to their relative permittivity inaccuracy and high loss tangent, different antenna structures were studied and designed in order to better pinpoint acceptable values for these variables. Variations in the FR4 relative permittivity can shift the operating frequency of the antenna and the high loss tangent affects significantly the antenna axial ratio and gain, resulting in poor antenna efficiency. In order to overcome this efficiency deficit the thickest substrate available was used.

A rectangular patch was chosen as the initial building structure to design the proposed directional array antenna, due to its ease of implementation, and its development was based on the theory presented in chapter 3, supported by numerous intermediate simulations.

Simulation results and 3-dimensional wave analysis using Anasoft's HFSS and Advanced Design System 2011 software have also been included, followed by a comparison table indicating the advantages of the proposed array antenna.

5.1.1 Single element

The microstrip antenna was developed in order to function according american RFID standards, as discussed in Chapter 4. As such, the antenna must have a bandwidth that incorporates frequencies between [902 928]MHz, meaning it must have a 26MHz bandwidth.

The center frequency of 915MHz was deemed proper for the development of the antenna.

Using the expressions presented in chapter 3, and assuming a dielectric constant of 4.2, the theoretical parameters calculated were

Frequency	ε_r	ε_{reff}	W	L	$\triangle L$	Z_{in}	y_0
915MHz	4.2	3.161	96.71mm	73.21mm	1.137mm	203.43Ω	26.46mm

Table 5.1: Microstrip antenna parameters

This test allowed to better estimate the FR4 dielectric constant in order to achieve better matching for 915MHz. It can be seen by Figure 5.1(b),that the S_{11} parameter's minimum was achieved at 937.95MHz, with a value of -35.05dB. This frequency shift was due to the incorrect parametrization of the dielectric constant of the FR4 laminate.

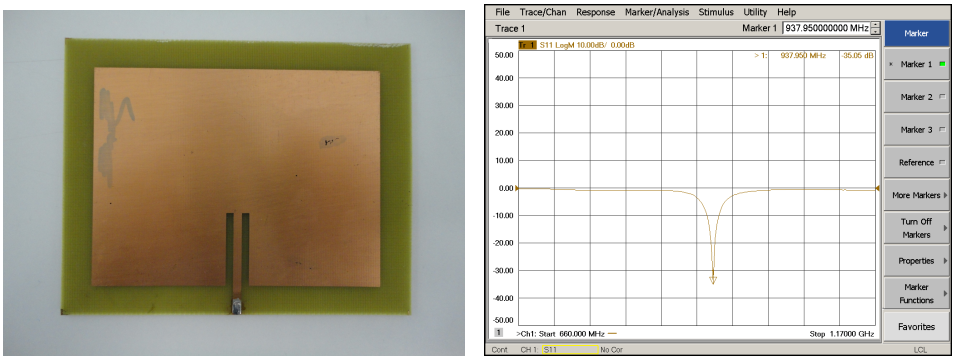

(a) (b)

Figure 5.1: Inset-fed microstrip antenna (a) and corresponding S_{11} parameter (b)

Once the antenna's parameters were studied, it was then necessary to design an antenna with circular polarization capabilities, based on the information given by the previous antennas. Upon various test procedures, the dielectric constant of 4.22 was the one that demonstrated better return loss values for frequencies close to 915MHz.

A simple way to obtain circular polarization was to chamfer the corners of the patch along a similar oblique direction, as shown in Figure 5.2. This figure illustrates an example of an right-hand polarization antenna, which is determined by the direction in which the corners were chamfered, meaning that a right-hand polarization could be obtained if the opposite corners were chamfered. Contrary to the previously studied antennas, this antenna has a near-square shape. The dimensions of the antenna were approximated using simulations in order to achieve optimal axial ratio. Coaxial-probe feeding was the preferred method, since, for the case of the inset-fed antenna, the antenna's structure was not very uniform for a near-square morphology and also because the inset microstrip line would deform the two orthogonal modes with a phase difference of 90^{o}.

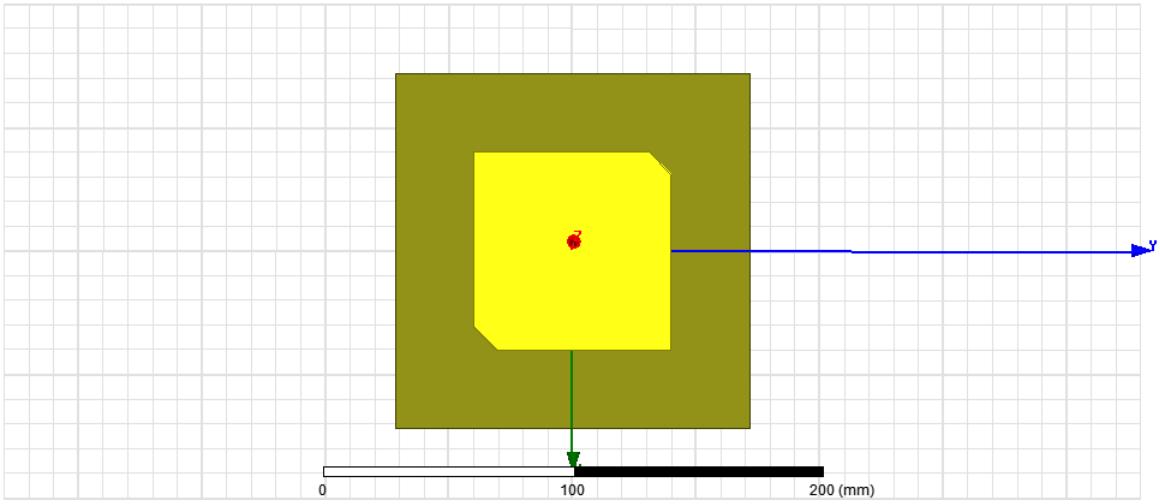

Figure 5.2: Square microstrip patch with circular polarization

The microstrip antenna was continuously subjected to modifications in order to achieve acceptable return loss (S_{11}) values for the 915MHz center frequency and to ensure the quality of the circular polarization, which was analyzed with respect to the axial ratio, being a value below 3dB acceptable and 0dB ideal.

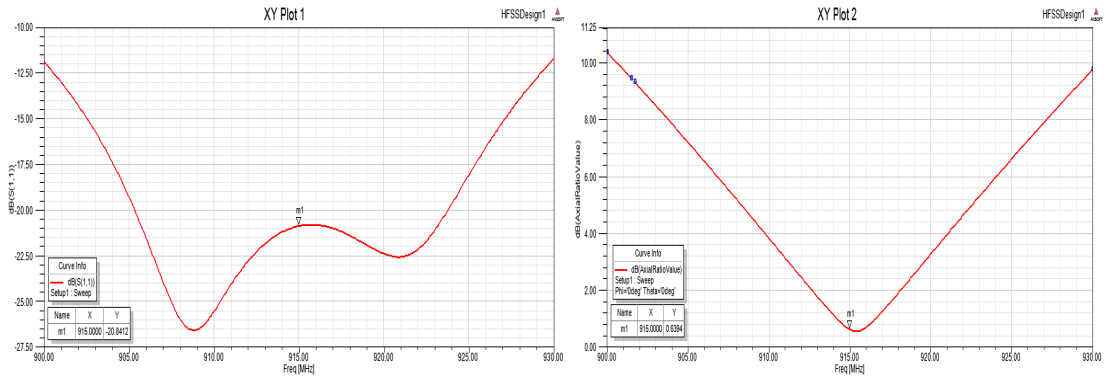

Figure 5.3: Simulated return loss (S_{11}) and axial ratio of the microstrip antenna

The simulated antenna, as shown in Fig(5.3), for a frequency of 915MHz has a good return loss value (S_{11}=-20.8412dB) and axial ratio (AR=0.6394), with a polarization bandwidth between [911 919]MHz.

Once finished the simulation tests, the antenna was ready for manufacturing. The final coaxial-probe fed microstrip antenna with right-hand polarization is shown in Figure 5.4.

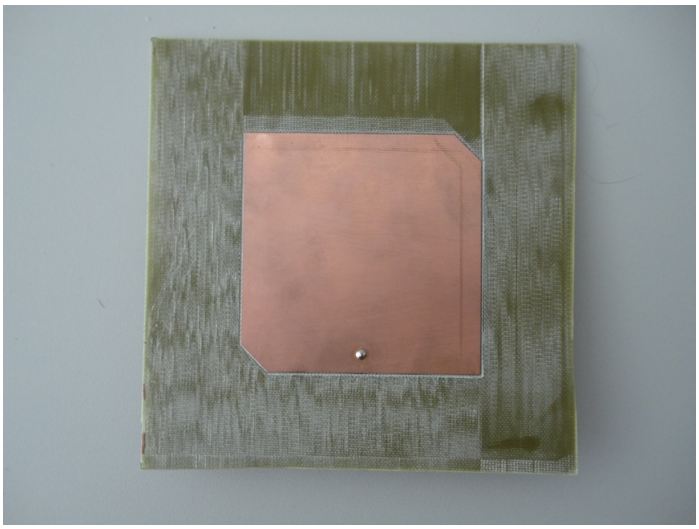

Figure 5.4: Manufactured antenna

Using a vector network analyzer (VNA) the S_{11} parameters were measured and subsequently compared to the simulated values, as shown by Fig(5.5). The S_{11} of the antenna has values similar to the ones simulated, with some minor differences, suffering an approximate 2dB return loss reduction at the 915MHz central frequency, being now at -18,73dB.

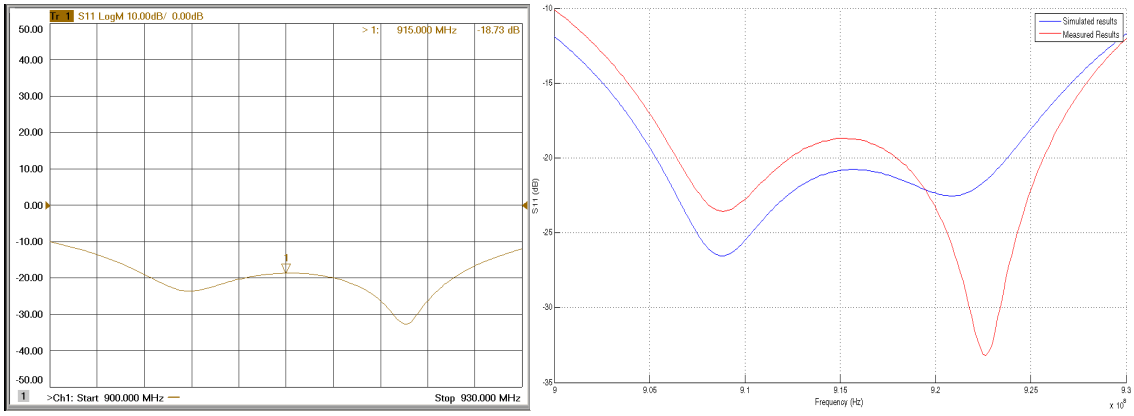

Figure 5.5: Return Loss (S_{11}) and comparison to simulated results

The microstrip antenna was then tested in an anechoic chamber in order to determine its polarization and radiation characteristics. The results show a good polarization matching with a significant inverse polarization rejection at 915MHZ.

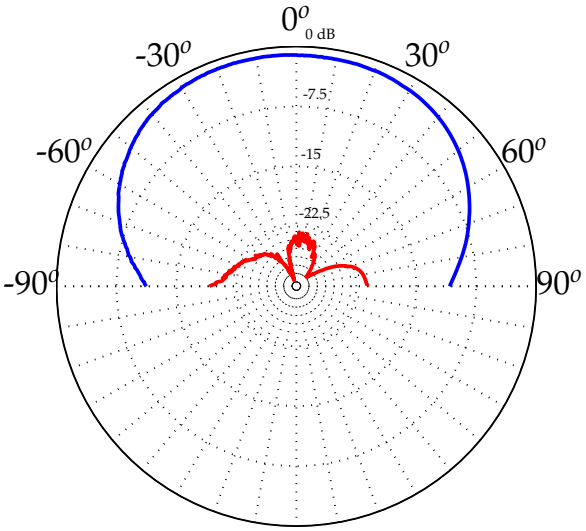

Figure 5.6: Left-hand polarization vs. Right-hand polarization for $\phi = 0^{o}$

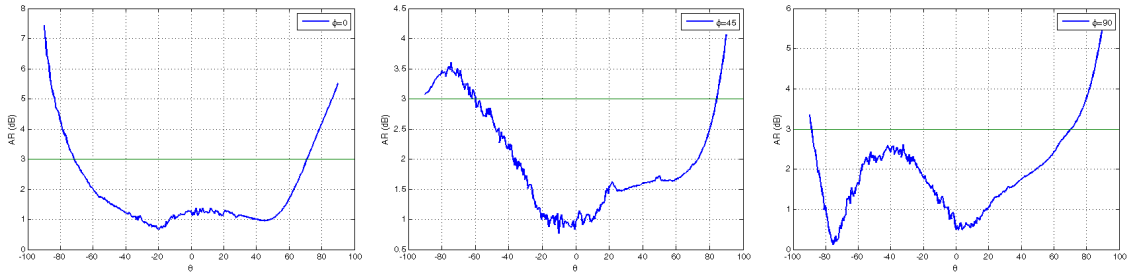

(a) (b) (c)

Figure 5.7: Axial Ratio for: (a)$\phi = 0^{o}$; (b)$\phi = 45^{o}$;(c)$\phi = 90^{o}$

The tests show that the antenna has solid right-hand polarization characteristics, corroborated by the axial ratio values that, for different values of phi (ϕ), are below 3dB, and good input impedance matching for the central frequency of 915MHz. The measurements present minor variations from the simulated results which may be explained by the undefined dielectric constant of the FR4 laminate, by the the welded coaxial-probe which may have been inserted in a slight incorrect position, by the thickness of the probe's feeding pin, or even by the solder used to join the probe and the antenna.

5.1.2 Antenna array with right-hand polarization

After studying the characteristics of a single microstrip antenna, and given the radiation pattern shown by Figure 5.6, it was then necessary to design the antenna array which would be used for beam steering applications. The morphology chosen for this array was an 4-element uniform linear array (ULA) of radiating elements.

Each antenna that constituted the array was studied prior to the simulation test phase. The return loss (S_{11}) and forward gain (S_{21}) were measured in the anechoic chamber.

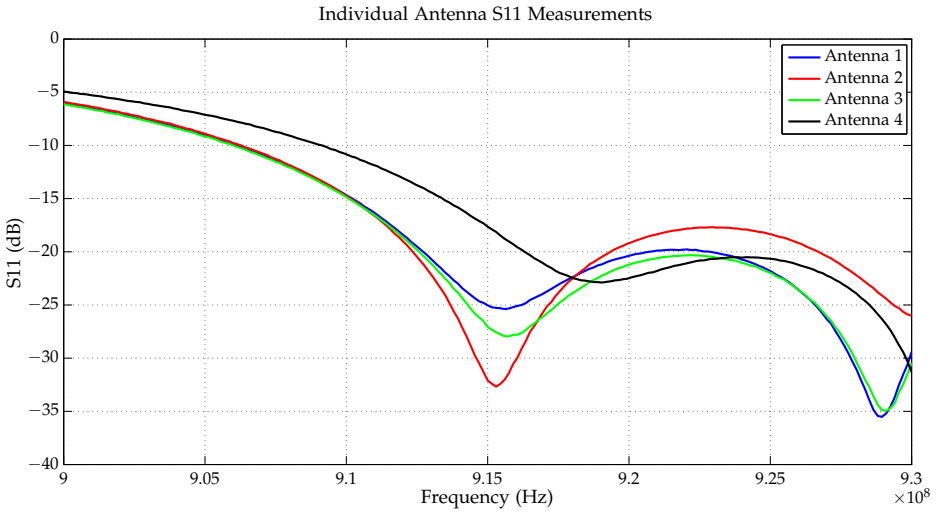

Figure 5.8: Return Loss (S_{11}) of the 4 antennas that incorporate the array

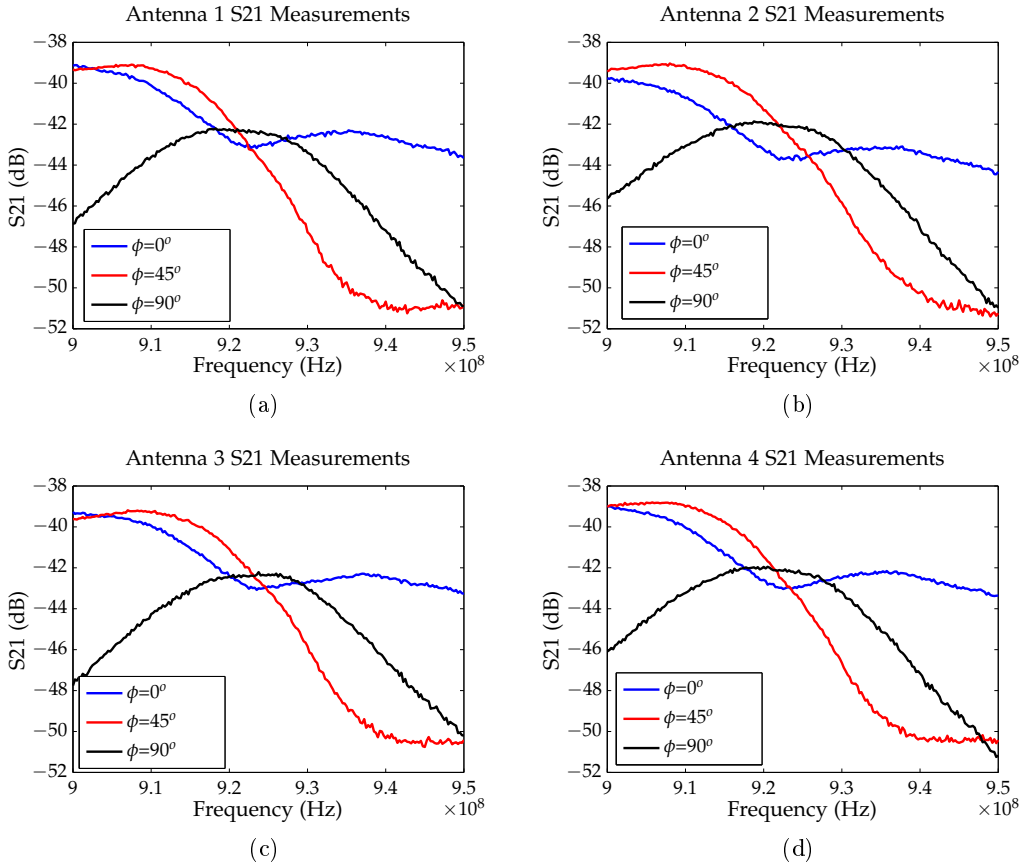

Figure 5.9: Forward Gain (S_{21}) of each of the antennas that incorporate the array

As shown by the measurements obtained, there was a considerable shift in both the S_{11} and S_{21} parameters, even though the structure of these antennas was similar to the original's. Further study and simulations were made, ultimately pointing to a change in the dielectric constant of the substrate as the most likely reason for this result discrepancy. The S_{21} tests now show that the new antennas have better polarization characteristics for a frequency of 922MHz, since for this frequency the forward gain of each antenna almost intersect for different values of ϕ. Even though these new values were substantially different from those initially obtained, these antennas were used for the final array structure, since the polarization frequency is contained within the permitted values for american RFID applications (between [902 928]MHZ) and the return loss measured was not significantly altered, maintaining a value of approximately -20dB for all antennas. These new values were taken into account when the array was designed, now considering 922MHz as the new working frequency of the antenna.

Various simulation tests were performed in order to determine the optimal distance between the antennas and, consequently, to obtain acceptable directivity and circular polarization. Results show that for a distance of $d = 0.75\lambda$ (being $\lambda = 327.86$mm) the array display better directivity (minimal main lobe width) and polarization (minimal axial ratio) responses, as shown by Table 5.2.

Distance between elements	Axial Ratio ($\theta = 0^o$)	Main lobe magnitude (dB)	Main lobe width (θ)	Main and secondary lobe distance (θ)	Secundary lobe magnitude (dB)	Antenna array dimension (mm)
0.55λ	1.5866	11.99	24	40	-1.64	684.58
0.6λ	1.6402	12.32	23	36	-1.48	733.76
0.65λ	1.5482	12.61	22	35	-0.84	782.94
0.68λ	1.5652	12.76	21	33	-0.10	811.88
0.7λ	1.5279	12.85	21	32	-0.3675	832.12
0.72λ	1.5304	12.95	20	31	-0.1879	851.8
0.75λ	1.3752	13.07	18	29	-0.0694	881.3
0.8λ	1.7189	13.22	16	27	-0.7357	930.49

Table 5.2: Evolution of various parameters of the 4-element ULA relative to the distance between adjacent elements

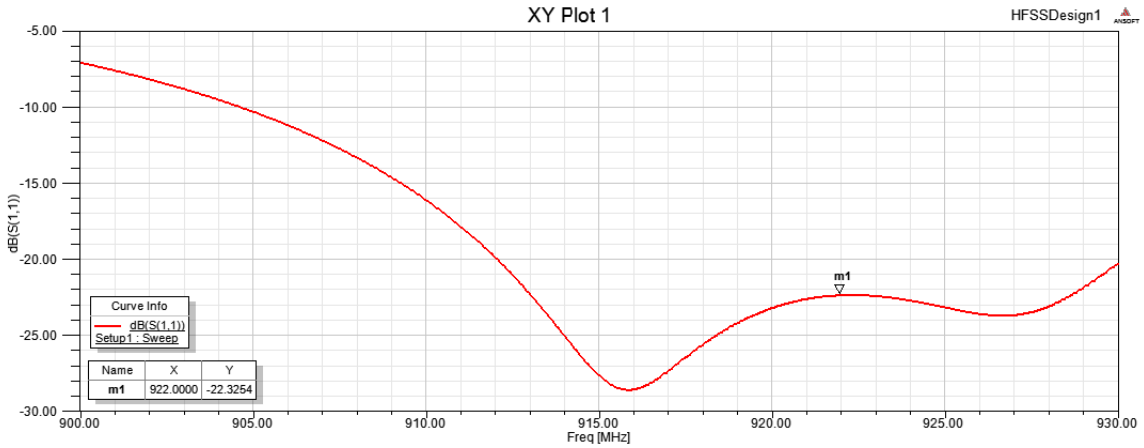

Figure 5.10: S_{11} parameter measurement

Analyzing Table 5.2 it is possible to infer that the width of the main lobe becomes narrower as the spacing between the elements increases, and also the greater the main lobe magnitude and smaller the secondary lobe become, thus making the radiation pattern of the array more directive. However, as the distance between elements increases, the number of secondary lobes also increases and the distance between the the main lobe and secondary lobes decreases.

The simulation of the uniform linear array shows that for the $\phi = 0^{\text{o}}$ plane the radiation pattern retains a similar shape for various values of θ, and as for the perpendicular plane ($\phi = 90^{\text{o}}$) it changes according with the distance between elements of the array, following the criteria stated above.

The final simulated 4-element ULA is represented by Figure 5.11, with a spacing of 0.75λ between antennas, and the resulting radiation pattern is shown in Figure 5.12.

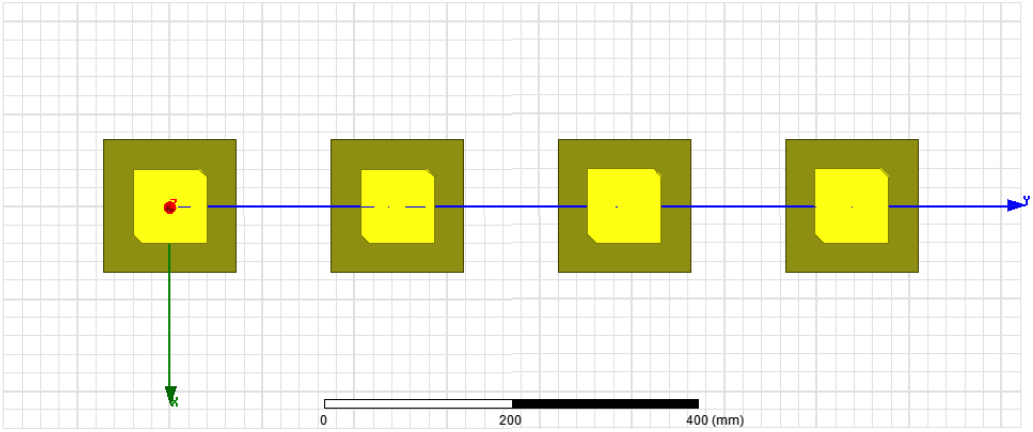

Figure 5.11: 4-Element Uniform Linear Array

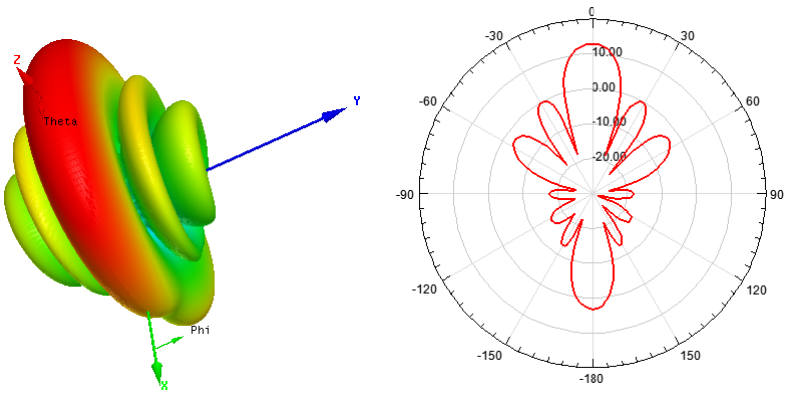

(a) (b)

Figure 5.12: Simulated radiation pattern of the ULA: (a) 3D representation (b) 2D representation

Terminated the simulation tests, the array structure was constructed in a way capable of accommodating each antenna at a precise distance of 0.75λ from each other. Due to the length of the array, acrylic plates were used to fix each element at a set distance from each other, providing a solid 144.32mm x 881.62mm structure in which the antenna array could be easily transported and deployed, as shown in Figure 5.13.

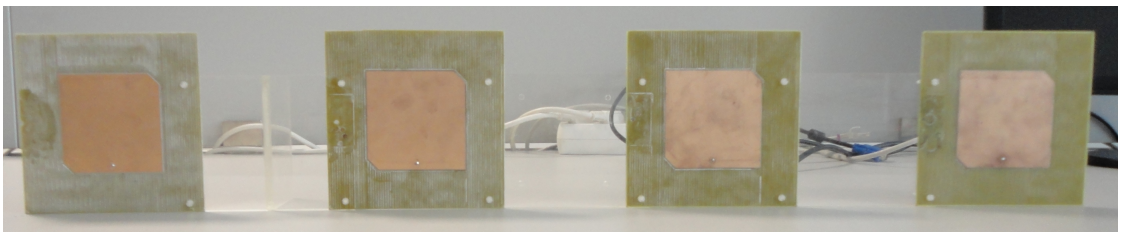

Figure 5.13: Uniform linear array structure

The antenna array was submitted to tests in the anechoic chamber in order to asses its radiation and polarization properties. The S_{11} parameter is shown in Figure 5.14 and the θ and ϕ field components are represented in Figure 5.15. To estimate the frequency at which the antenna array would display better circular polarization characteristics, the S_{21} parameter was also measured for $\phi = 0^{o}$, $\phi = 45^{o}$ and $\phi = 90^{o}$. As demonstrated by Figure 5.17, the array shows good circular polarization for a frequency of 922MHz, corroborated by the axial ratio values, for various values of ϕ, presented by Figure 5.18.

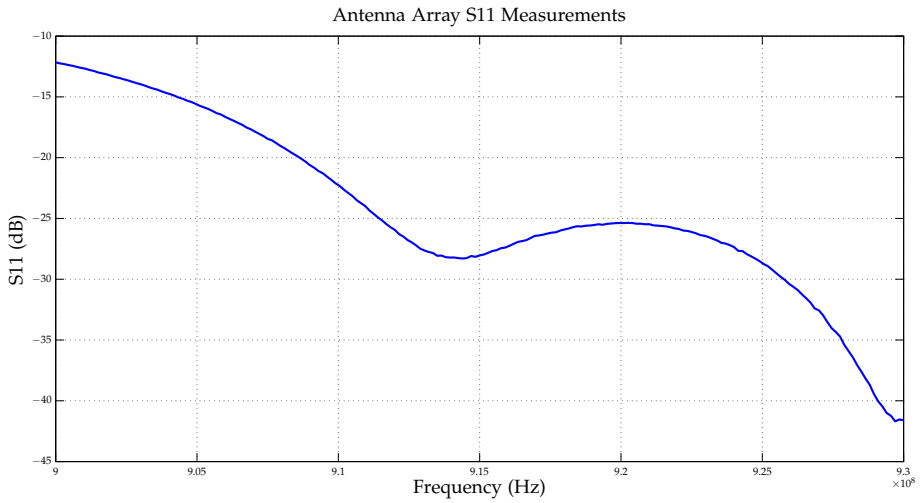

Figure 5.14: Return Loss (S_{11}) of the antenna array

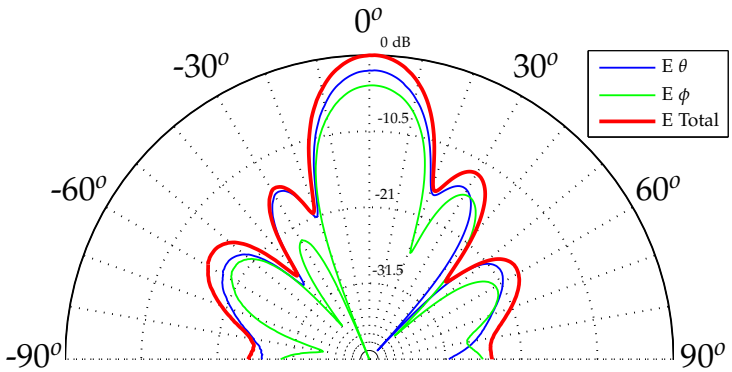

Figure 5.15: Radiation pattern of the antenna array

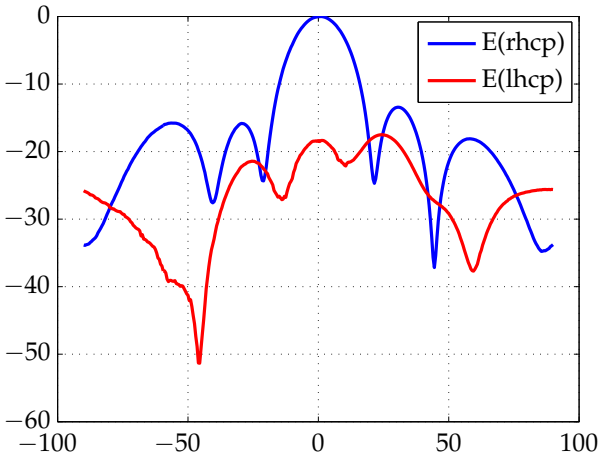

Figure 5.16: Right-hand and Left-hand components of the antenna array

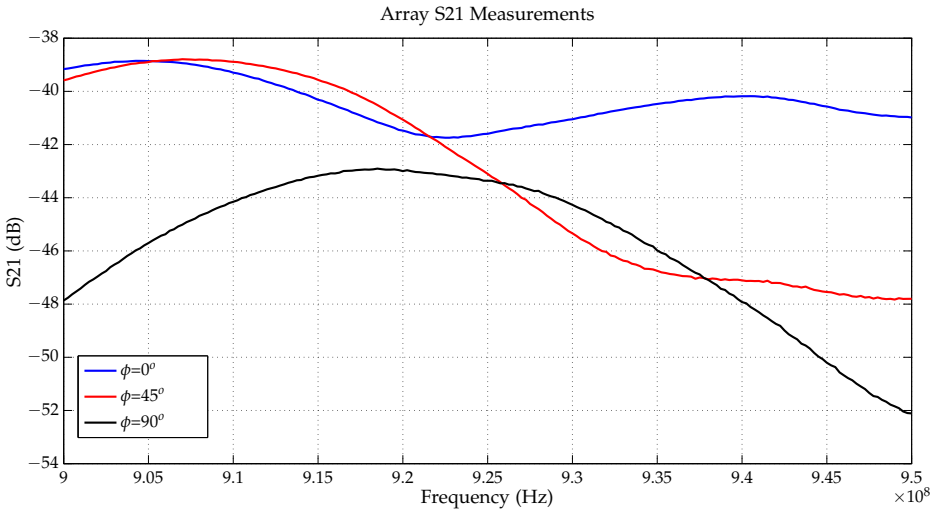

Figure 5.17: S_{21} parameter of the antenna array

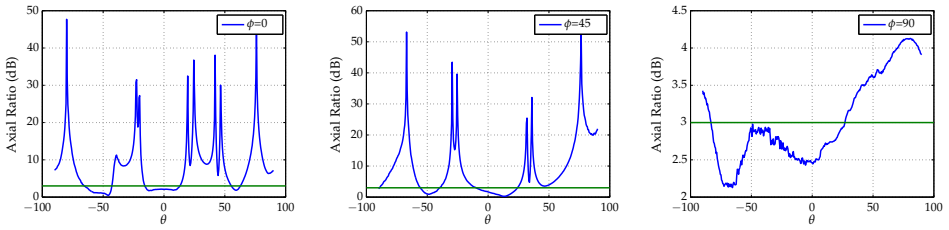

(a) (b) (c)

Figure 5.18: Axial Ratio for: (a) $\phi = 0^{o}$, (b) $\phi = 45^{o}$, (c) $\phi = 90^{o}$

Results show that the antenna array presents return loss values close to the ones simu-

lated, resulting in a value of -25.86dB at 922MHz, meaning that the antenna presents proper impedance matching at this frequency.

As for the radiation pattern, results show that the width of the antenna array's main lobe is approximately 12^{o}, presenting good circular right-hand polarization characteristics, corroborated by the axial ratio values and by Figure 5.16, showing a left-hand component rejection of 18.5dB at the maximum direction, for $\phi = 0^{o}$. Also it can be extrapolated that the distance between main and secondary lobes is approximately 31.5^{o}, close to the results simulated.

5.2 Phase Shifting Circuit Design

5.2.1 Initial Considerations

Prior to the final PCB board designs, several concepts and methods were pondered in order to better implement and test a circuit capable of basic beam steering functions, which could be used for both transmission and reception purposes.

In order to test the various possible circuit configurations, a breadboard, used primarily as a flexible circuit prototyping platform, and pre-assembled board embedded with a PIC32MX795F512H micro controller, were used as the preferred assembly blocks for this project. This initial implementation would later be used as the base for more specialized boards, with further developed capabilities and tighter hardware integration. The constructed boards, as well as design considerations and results, will be discussed and compared, highlighting the main differences and changes provided be the new layouts.

5.2.2 Prototype Board

The circuit developed had as base the scheme depicted in Figure 5.19.

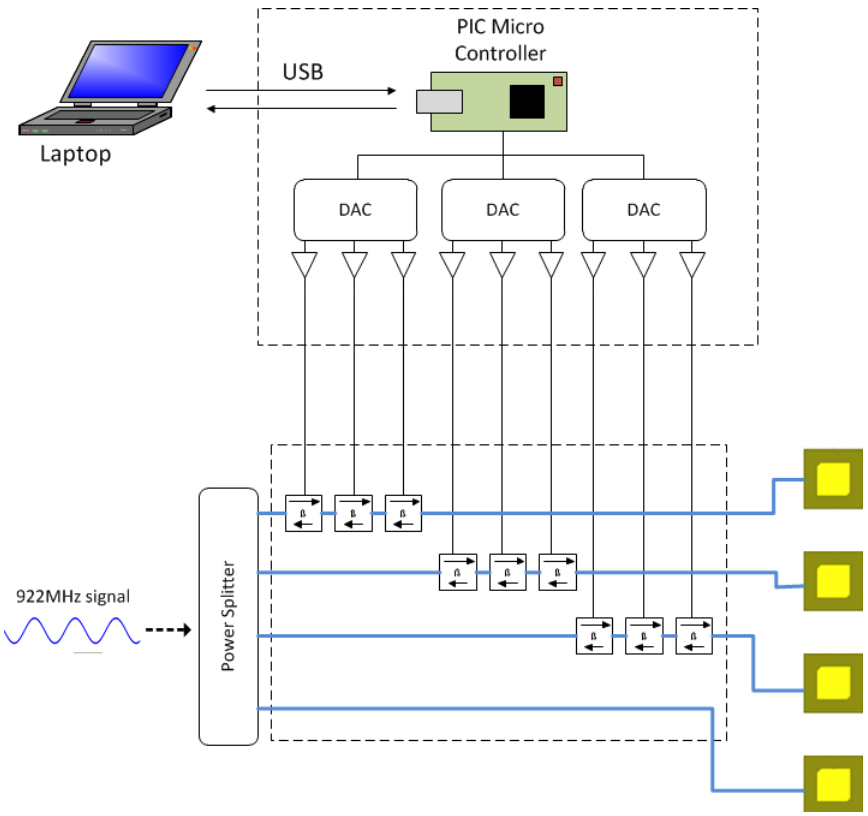

Figure 5.19: Block diagram of the beamforming circuit

The prototype circuit developed in this work is divided in two modules. The first module is equipped with a PIC32MX795F512H micro controller, responsible for communicating with the PC, via RS232 protocol. This micro controller is equiped with a 80MHz, 32-bit MIPS M4k core, 512K FLASH memory and 128K RAM. The information received by the MCU, containing the calculated normalized weights, is forwarded to three MAX506 DACs, simultaneously, via 8-bit parallel communication. These DAC's operate with a single +5V supply and provide 4 rail-to-rail voltage outputs. Each of the DAC's outputs were linked to TL084 voltage amplifiers. The circuit schematic of the board is presented in Attachments Chapter.

The second module is responsible for shifting the phase of each of the signals feeded to each antenna of the array. The developed board is made of 0.78mm thick FR4 substrate with 35μm thin copper layer on the bottom side, designed to be the ground plane. The board is capable of accommodating up to 3 channels, each linked to an output port of a ZN8PD1-53-S+ power splitter, which receives the source signal to be transmitted and feeds it to each of the board's inputs. Soldered on the top plane, three PS088-315 phase-shifters, each capable of introducing around 100º phase-shift, are placed on each of the existing channels responsible for guiding the signal to each of the antennas of the array, providing an approximate 300º phase-shifting capability to each channel, leaving the fourth channel functioning as a necessary phase reference for the normalized weights. Each phase shifter was controlled by a DC voltage, ranging from 0V-12V, applying to each channel a shift to the signal's phase proportional to the voltage delivered by the TL084 voltage amplifier from the control module. The microstrip lines responsible for guiding the high frequency signal are 1.438mm wide, resulting in a 50Ω impedance line, matching both the SMA connectors and the IC's impedance. The board was

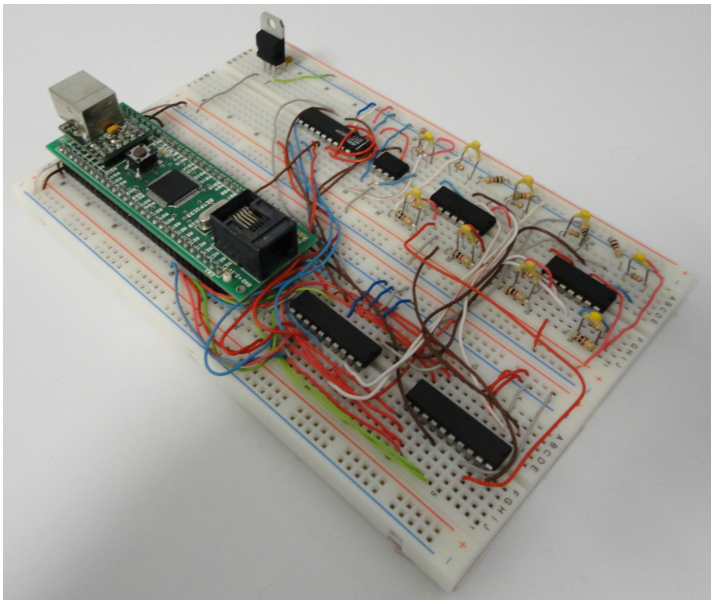

Figure 5.20: Control module

first designed using CADSoft Eagle software, as shown by Figure 7.2, and finally manufactured, resulting in the circuit presented in Figure 5.21.

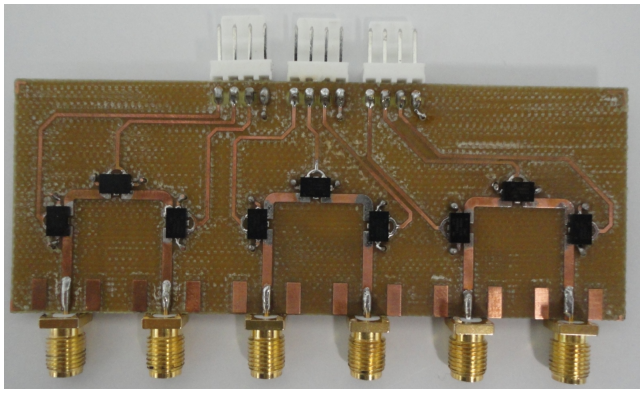

Figure 5.21: Final prototype board

In order to conjugate both modules it was necessary to project the voltage amplification section of the control module to achieve the maximum range available. As such, a non-inverting configuration, with a gain of approximately 2.5, was used in order to extend the limited voltage output of the DAC to the full range accepted by the phase-shifters. The schematic and the final circuit of the control module is presented by Figures 7.1 and 5.20, respectively. The TL084s are powered by an external $\pm 15V$ source and the MAX506s are powered by the MC7805 voltage regulator, functioning as a stable +5V source.

The prototype board setup is shown by Figure 5.22 and is the the first implementation of a circuit capable of basic beam steering. This configuration was the one tested in an anechoic chamber, being the resulting measurements later discussed and compared to the final transmitter board.

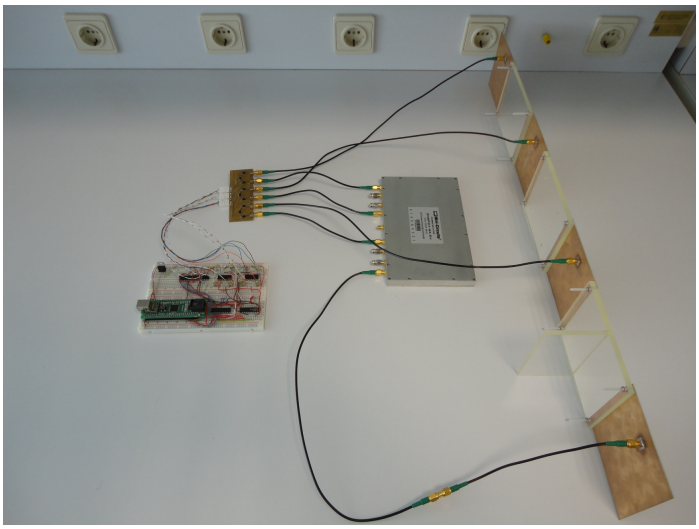

Figure 5.22: Prototype board setup

5.2.3 Final Board

The receiver board that was developed in this work was made of 0.81mm thick FR4 substrate with 35μm thin layers of copper on both sides. Both the bottom and the top layers of copper were designed to be a ground plane and a base for routing, being only the top copper layer utilized for soldering the hardware components. Even though the some of the ground plane was removed due to the routing, the portion corresponding to the high frequency microstrip line of each channel was left intact, in order to achieve better RF signal transmission quality. In terms of dimension, the board measures 129.28mm wide and 58.09mm high. This board closely followed the prototype's concept with the differentiating characteristic that it now has an embedded a PIC32 micro controller and two serial-controlled DACs, used for information processing and for applying the computed weights to each channel.

The developed receiver board does not include any form of internal power source, making it necessary to connect the board to a $\pm 15V$ source to power-up the circuit. The board contains a MM232 USB/UART interface, used for receiving the computed normalized weights from MATLAB, via RS232 communication. This information is relayed to a PIC32MX110F016B micro controller, responsible for reading and transmitting this information to two 12-bit MCP4822 DAC's, using SPI protocol. The PIC microcontroller is comprised of a 40MHz, 32-bit RISC CPU, two I2C/SPI modules, 32KB FLASH memory and up to 8K SRAM memory. The output of these DACs range between [0.6 2.045]V thus being necessary to project a voltage amplification section, using a TL084 voltage amplifier, to achieve maximum voltage control range for the phase shifters. Similarly to the prototype and transmitter boards, the RF lines have a 1.44mm width, providing the 50Ω matching required by the phase shifters and the SMA connectors for this range of frequencies. The circuit schematic can be consulted in Attachments chapter.

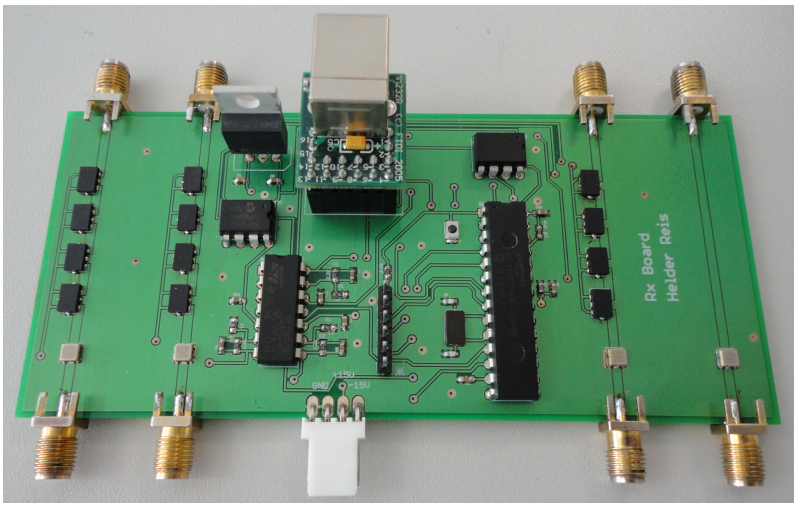

Figure 5.23: Final receiver board

Much like the prototype board, the voltage amplifying section was projected in order to achieve maximum phase-shifting control range. As such, the following relation for non-inverting amplifying configurations was used

$$V_{out} = (1 + \frac{R_2}{R_1})V_{in} \tag{5.1}$$

where it was defined $R_2 = 2.2K\Omega$ and $R_1 = 430K\Omega$, knowing that $Vmax_{in} = 2.045V$ and the intended control voltage was $V_{out} = 12V$, resulting in a configuration with a gain of approximately 6. The control voltage of each of the outputs of the TL084 is directed towards a specific channels, powering up simultaneously a set of 4 phase-shifters, granting each channel the capacity to introduce a phase shift of approximately 400°. Once again, one of the channels does not introduce any shift in the signal's phase, functioning as the reference channel for the computed normalized weights. As the primary function of this board is to receive RF signals from an external source, B3588 SAW filters were used on each channel in order to filter unwanted interferences and, consequently, to guarantee better signal reception.

Chapter 6

Smart Antenna System Results

6.1 Beamformer Measurements

The proposed beamformer setup utilized the circuit discussed in Chapter 5. The test was made using the prototype board, as to better assess the behavior and characteristics of a simple phase shifting capable circuit. The initial setup was assembled as shown by Figure 6.1. The UHF signal was to be fed to a ZN8PD1-53-S+ power splitter and divided into four channels, each connected to the phase shifting capable PCB board. The board would then, after inserting the appropriate shifts in phase determined by the algorithm's computed weights, carry each of the signals to an individual antenna of the array.

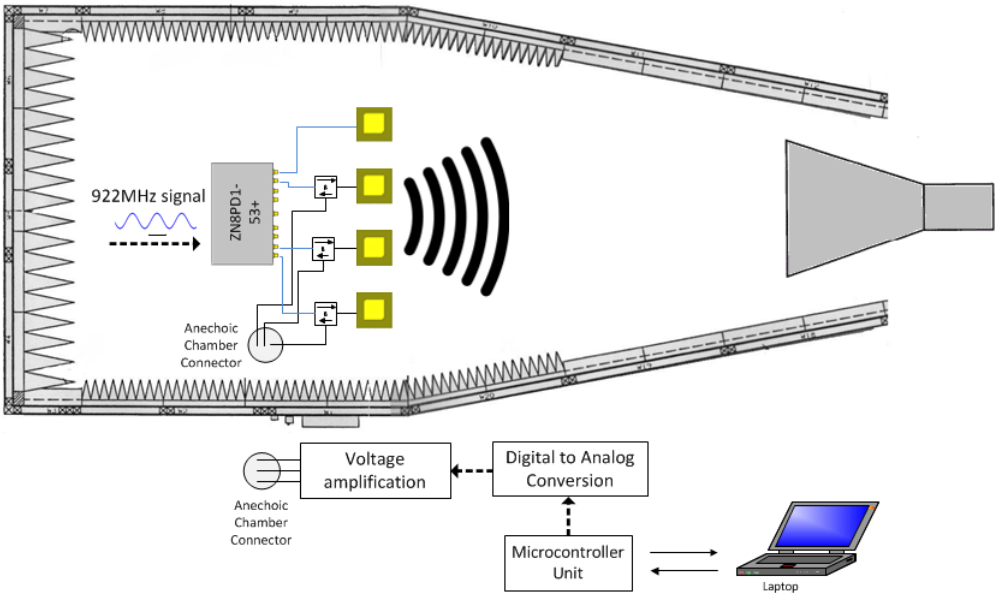

Figure 6.1: Beamformer measurement test setup

In order to utilize the circuit it was necessary to physically connect the computer to the micro controller unit inserted in the breadboard, thus creating a communication channel specifying the desired direction in which the main lobe of the radiation pattern would be steered. As such it was necessary to divide the circuit, leaving the control module outside the

anechoic chamber, to grant direct communication between PC and circuit, and attach the PCB board to the the power splitter and antenna array, which were positioned inside the chamber. The link between the two modules was reestablished by using the anechoic chamber's built-in I/O connector.

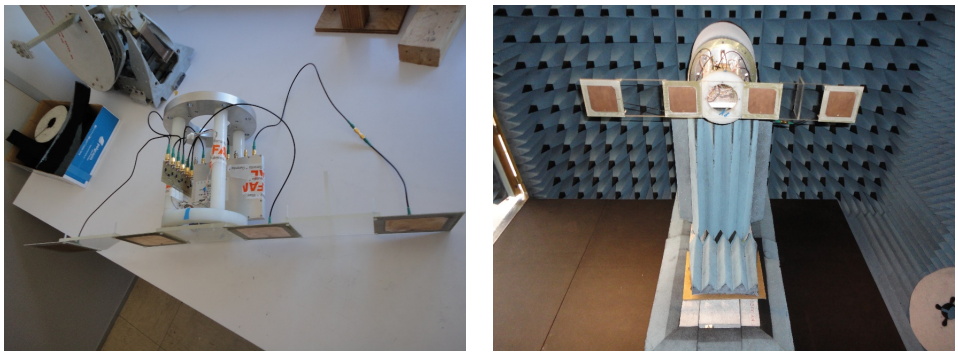

(a) (b)

Figure 6.2: Beamformer setup

The beamforming measurements were conducted by applying a 13dBm signal to the transmitter, with a frequency of 922MHz. This section discusses and compares the various results provided by the different beamforming algorithms, introduced in Chapter 2. Additional information, regarding the acquisition and tracking of the signal of interest behaviour of each of the discussed algorithms, is present in the Attachments chapter, used to consolidate the underlying understanding of of each method when used in different applications and/or environments.

6.1.1 Mean-Square Error Minimization Algorithms Output

This section focuses on the measurement and comparision of both the Least Mean-Squares and Recursive Least-Squares beamforming outputs and convergence speeds. The measurement process was divided into three main parts. First, the radiation pattern's main beam was steered into a single predetermined angle. Secondly, null steering was realized in parallel with the steering of the main lobe towards a given direction. Finally, it was considered that two signal of interest were being emitted, each at a different angle, thus forming two beams, each directed towards a separated direction. For ease of comparison with the measured results, simulated outputs were also included in this section.

For this measurement procedure the signal of interest was considered as being a sinusoidal wave of constant amplitude and a span of an hundred samples were used in order for the algorithm compute the complex weights necessary for the beamforming process.

This section finalizes with an overview in which is summarized the results obtained throughout the measurement tests, offering a more detailed view on the characteristics on each of the used algorithms, along with a study on the obtained beampatterns produced by the antenna array. The graphical representation of the results are present in the Attachments chapter whereas this chapter focuses on the interpretation of said results.

6.1.1.1 Beam Steering for a single θ_{SOI}

The first measurement test focused on the steering of a single maximum of the radiation pattern produced by the antenna array, towards a specified set of angles. It is first presented the results produced by the LMS algorithm for $\theta_{SOI} = 0^{o}$, $\theta_{SOI} = 30^{o}$, and $\theta_{SOI} = -30^{o}$, followed by the measured results obtained by the RLS algorithm, for the same angle set. This section finalizes with a brief summary of both method's measured results, offering a comparision based on the directivity and convergence speeds obtained by each of them. It is also analyzed the antenna array's circular polarization property, as to determine the polarization's quality for various different steering angles.

Least Mean-Square Algorithm

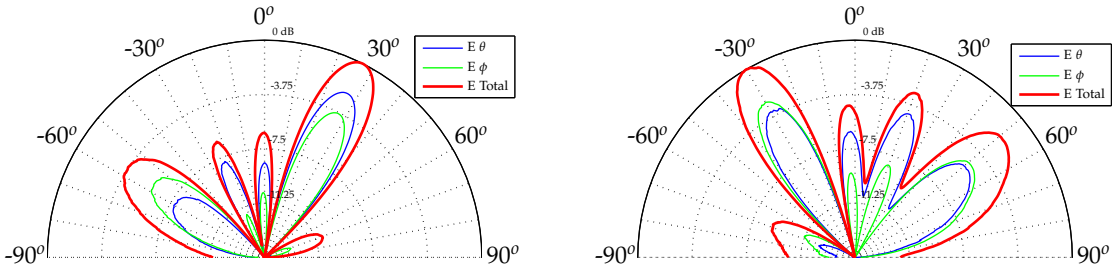

(a) (b)

Figure 6.3: Examples of measured radiation patterns for a single θ_{SOI}

Angle (θ)	Main lobe direction (θ)	Main lobe width (θ)	Distance between main and side lobes		Side lobe normalized maximum amplitude	
			Left Side Lobe (θ)	Right Side Lobe (θ)	Left Side Lobe (dB)	Right Side Lobe (dB)
0º	-0.5º	16º	29.5º	27º	-6.485	-5.069
30º	27º	18.5º	27º	43º	-6.439	-10.22
-30º	-30º	18.5º	37.5º	27º	-8.938	-4.516

Table 6.1: LMS measured parameters

Recursive Least-Squares Algorithm

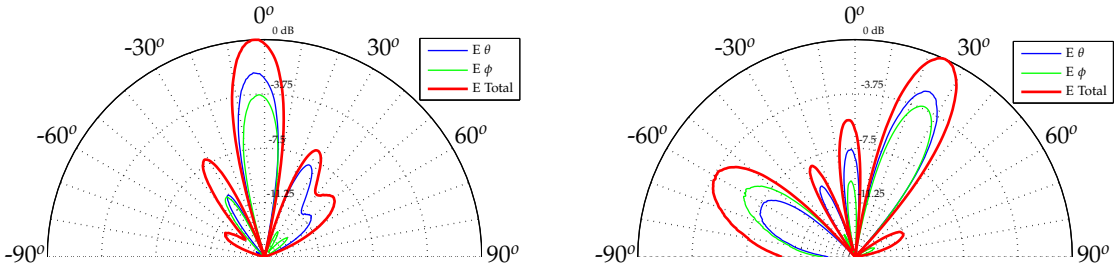

(a) (b)

Figure 6.4: Examples of measured radiation patterns for a single θ_{SOI}

Angle (θ)	Main lobe direction (θ)	Main lobe width (θ)	Distance between main and side lobes		Side lobe normalized maximum amplitude	
			Left Side Lobe (θ)	Right Side Lobe (θ)	Left Side Lobe (dB)	Right Side Lobe (dB)
0^o	-2.5^o	15.5^o	28.5^o	29.5^o	-7.174	-6.805
30^o	24.5^o	18^o	27^o	39.5^o	-5.556	-11.34
-30^o	-28^o	17.5^o	38.5^o	28^o	-8.609	-4.133

Table 6.2: RLS measured parameters

The normalized beamformer outputs obtained with LMS and RLS algorithm are shown for $\theta = 0^o$, $\theta = 30^o$ and $\theta = -30^o$. The beampattern agrees fairly well with the simulation outputs, presenting just some minor differences. One such difference is the amplitude of some of the measured secondary lobes that are considerably greater than the ones expected by simulation. A minor steering error was also introduced for both methods, causing the main lobe of the radiation pattern to be slightly off from the intended direction. This may be explained by a phase shift introduced by the high frequency cables used to connect the circuit or even even by minor offsets created by the control voltage used to adjust the phase shifters functionality.

In this test, the convergence speed of each of the tested methods is the main differentiator between the Least-Mean Squares and the Recursive Least-Squares methods, since the beampattern produced by these to methods are identical, as corroborated by Table 6.1 and Table 6.2.

For the LMS method, for different beam steering angles, the computed weights for each channel stablilized after approximately six iterations, presenting this algorithm as a fast converging method, adequated for basic beamforming applications. Also, it is interesting to see that the calculated complex weight values are equal for all the channels present within the system.

On the other hand, for simple applications where a simple beam must be directed towards a specified angle, ignoring null steering or multiple beamforming functionality, the RLS showed

a slightly slower weight convergence rate than the Least-Mean Squares approach, taking the algorithm about twenty iterations in order stabilize its weights. These results can be corroborated by the track and hold capability, demonstrated by both algorithms, of the reference signal. It is shown that both methods successfully acquire and track the desired signal after approximatelly the number of iterations taken in order for the weights to stabilize. it is also visible that the obtained RLS weights diverge slightly from each other, being this the consequence of a minor alteration of their real components, indicated by faint change of the signals amplitude computed by the algorithm.

It is also shown that, for each of the angles chosen to steer the antenna array's radiation pattern, the circular polarization property was lost. This may be due to the different radiation characteristics of each of the array's elements produced by the imprecisions in the dielectric constant, characteristic inherent to the FR4 dielectric and previously discussed previously, or a misalignment of the array when mounted in the anechoic chamber.

6.1.1.2 Beam Steering for a single θ_{SOI} and θ_{SNOI}

The second test was centred on the steering of a single maximum and a single null of the radiation pattern, produced by the antenna array, towards a specified set of angles. First are presented the results produced by the LMS algorithm, followed by the measured results obtained by the RLS algorithm, for the same set of angles. This section concludes with brief summary of both method's measured results, comparing the directivity and convergence speeds obtained by each. The antenna array's circular polarization property is also analyzed, as to determine the polarization's quality for various different steering angles.

Least Mean-Square Algorithm

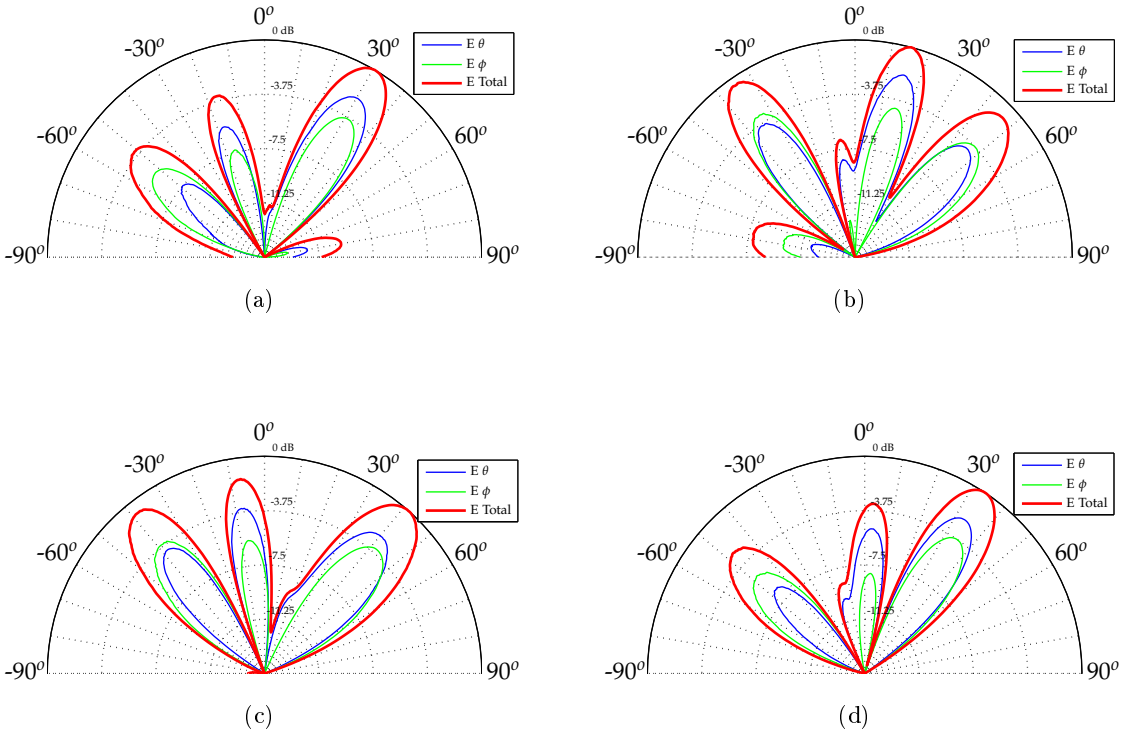

Figure 6.5: Examples of measured radiation patterns for a single θ_{SOI} and θ_{SNOI}

Angle (θ_{SOI})	Main lobe direction (θ)	Main lobe width (θ)	Distance between main and side lobes		Side lobe normalized maximum amplitude	
			Left Side Lobe (θ)	Right Side Lobe (θ)	Left Side Lobe (dB)	Right Side Lobe (dB)
45º	30.5º	20.5º	47.5º	49.5º	-3.409	-9.636
-45º	-33.5º	18.5º	42.5º	27.5º	-6.262	-6.104
60º	42º	23.5º	49º	-	-1.475	-
-60º	-47.5º	23º	-	50º	-	-3.276

Table 6.3: LMS measured parameters

Recursive Least-Squares Algorithm

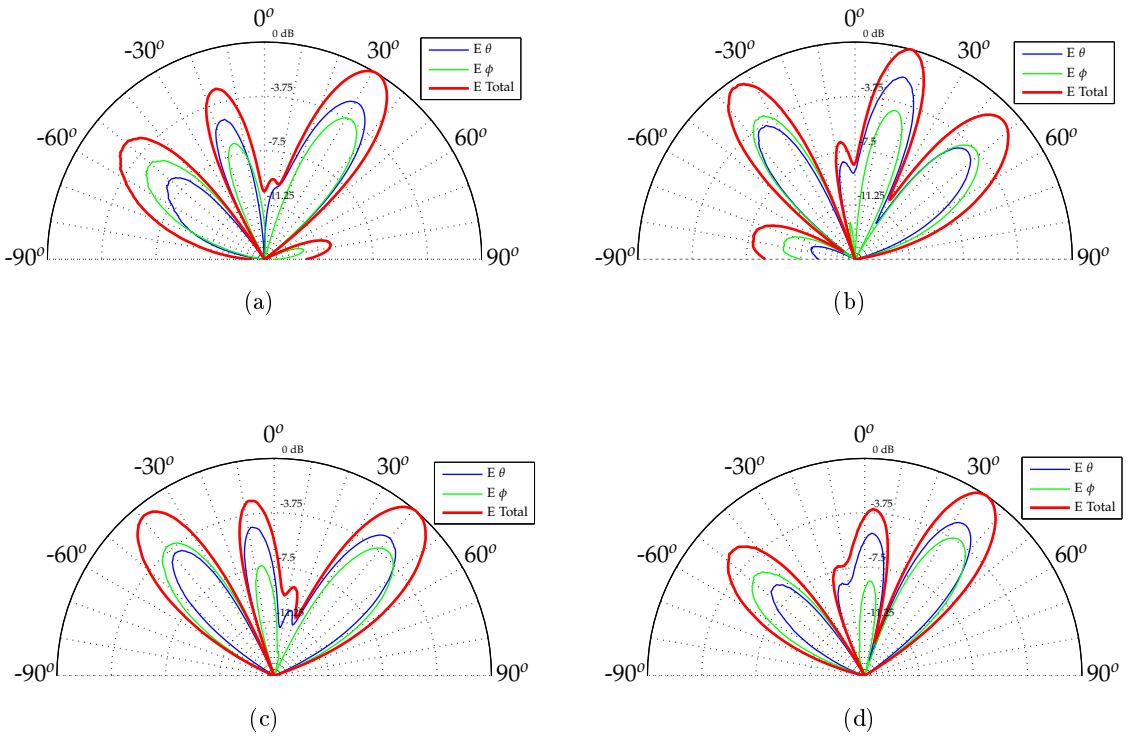

Figure 6.6: Examples of measured radiation patterns for a single θ_{SOI} and θ_{SNOI}

Angle (θ_{SOI})	Main lobe direction (θ)	Main lobe width (θ)	Distance between main and side lobes		Side lobe normalized maximum amplitude	
			Left Side Lobe (θ)	Right Side Lobe (θ)	Left Side Lobe (dB)	Right Side Lobe (dB)
45º	31º	20.5º	47º	46º	-2.753	-10.33
-45º	-34º	18.5º	43º	27º	-6.839	-6.124
60º	41º	22.5º	48º	-	-2.837	-
-60º	-47	23.5	-	51º	-	-3.538

Table 6.4: RLS measured parameters

This measurement test studied the behavior of both methods when null steering functionality is introduced, in order to cancel out a hypothetical interference originated from a determined direction. The resulting beampattern from both LMS and RLS algorithms show some differences from the intended simulated output, like the introduction of some steering errors, causing the main lobe and the nulls of the radiation pattern to be slightly off from the intended direction. Unlike the previous measurement test, where no null steering functionality was programmed into the algorithm, the computed complex weights in these tests required

both amplitude and phase adjustments, in order to obtain optimum directional resolution. The hardware used for these measurements was not, however, equipped with means to alter the signal's amplitude of each channel, generating an output that, in addition to the previously stated possible error inducing problems, generated a beampattern closely matched, but imperfect, to the intended simulated results.

These tests show that when the LMS's algorithm complexity is increased, with the introduction of the null steering property, its convergence speed is greatly reduced, as presented by the progression of the complex weights throughout the iteration span. A significant value fluctuation of the weights, approximatelly up to the sixtieth iteration, can be seen for all of the chosen measurement angles, point at which the weights reach a more stable behavior.

A more detailed overview of some of the parameters produced by this method's beamforming output can be seen in Table 6.3.

As for the beamforming tests achieved by the RLS algorithm, results show that the complex weight's progression stabilizes only after about the twenty-fifth iteration, demonstrating a much faster convergence rate than the LMS method. The measurement parameters for the different angles of the RLS algorithm are condensed in Table 6.4. These results can be corroborated by the acquisition and tracking capability of the desired signal, by both algorithms. The LMS method shows difficulty in converging the signal outputted by the algorithm with the one generated as a reference, up to approximatelly sixty iterations. As for the RLS method, it is shown a much faster and stable convergence process, achieving the required weight solution in about twenty-five iterations.

Analyzing the antenna array's axial ratio properties it also can be concluded that the circular polarization characteristic is held for all measurement angles, having a value inferior to three for all signal of interest's directions.

6.1.1.3 Beam Steering for two θ_{SOI}

The third and final test was centred on the steering of two maximums towards a specified set of angles. The results produced by the LMS algorithm are first presented, followed by the measured results obtained by the RLS algorithm, for the same angle set. This section concludes with brief summary of both method's measured results, comparing the directivity and convergence speeds obtained by each of the used algorithms. The antenna array's circular polarization property is also analyzed, as to determine the polarization's quality for various different steering angles.

Least Mean-Square Algorithm

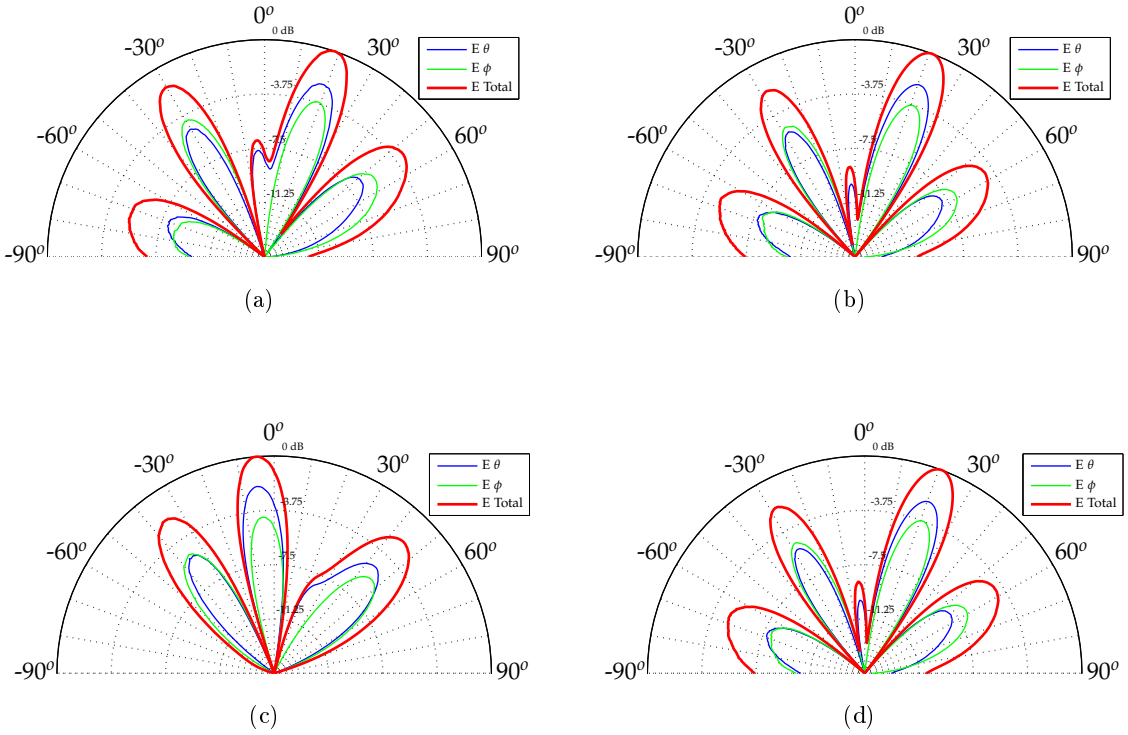

Figure 6.7: Examples of measured radiation patterns for two θ_{SOI}

Angles (θ_{SOI})	Closest main lobe direction		Closest main lobe width		Closest main lobe maximum normalized amplitude	
	First Main Lobe (θ)	Second Main Lobe (θ)	First Main Lobe (θ)	Second Main Lobe (θ)	First Main Lobe (dB)	Second Main Lobe (dB)
20º/60º	19º	53.5º	16.5º	28.5º	0	-3.085
60º/-60º	58º	-67º	30º	30.5º	-4.924	-4.332
0º/45º	-4.5º	45º	15.5º	25.5º	0	-2.285
-20º/-80º	21º	-67º	17º	34.5º	0	-4.872

Table 6.5: LMS measured parameters

Recursive Least-Squares Algorithm

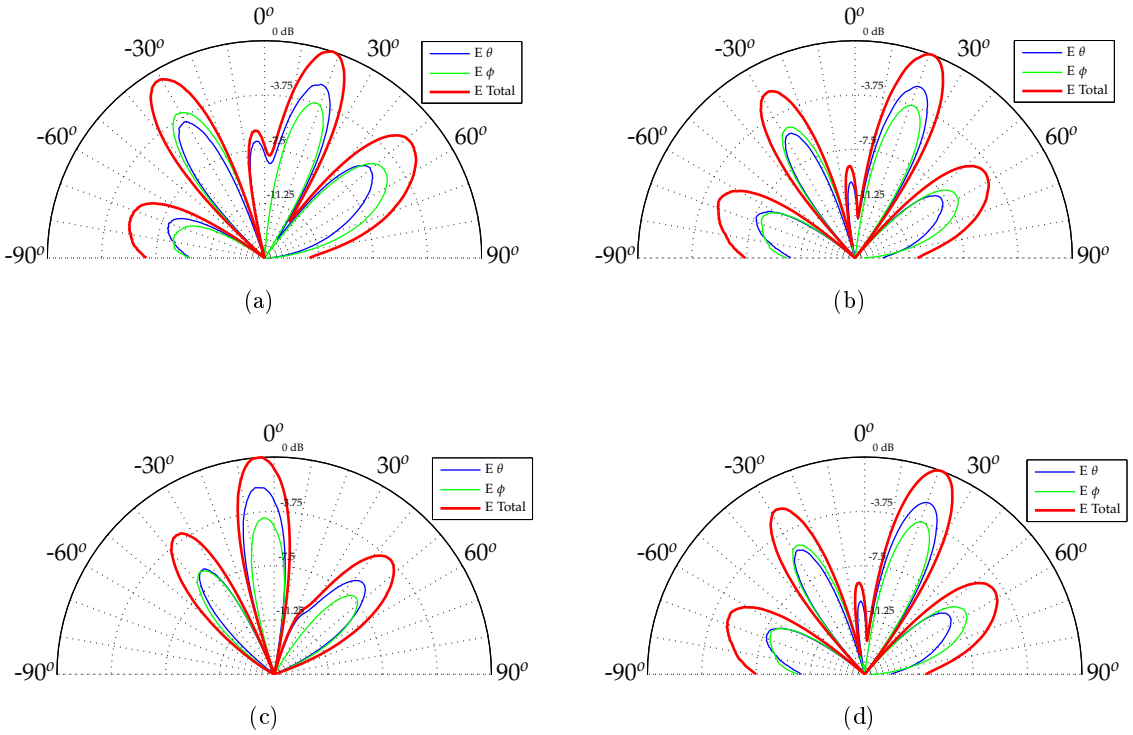

Figure 6.8: Examples of measured radiation patterns for two θ_{SOI}

Angles (θ_{SOI})	Closest main lobe direction		Closest main lobe width		Closest main lobe maximum normalized amplitude	
	First Main Lobe (θ)	Second Main Lobe (θ)	First Main Lobe (θ)	Second Main Lobe (θ)	First Main Lobe (dB)	Second Main Lobe (dB)
20º/60º	18º	51º	16.5º	27.5º	0	-2.141
60º/-60º	58.5º	-66º	32º	30º	-4.268	-4.332
0º/45º	-3.5º	45º	16º	22º	0	-3.741
-20º/-80º	21º	-66º	16.5º	35º	0	-4.822

Table 6.6: RLS measured parameters

This measurement test functioned as a study on the behavior of both LMS and RLS algorithms for a situation when information must be transmitted to two directions simultaneously. Similarly to the measurements where null steering was performed, by directioning two maximums of the antenna's radiation pattern to different directions, adjustments of both

the phase and magnitude of each of the channel's signal are also required. Due to hardware limitations, changes in the signal's amplitude were not performed, creating a slight deviation of the measured beampattern relative to the simulated and, as a consequence, resulting in some degradation in directional resolution.

In concordance to the previously realized tests, the LMS and RLS algorithms output a very similar beampattern, only showing differentiating characteristics in their convergence speed via the behavior of their complex weights along a set number of iterations defined in their code.

The Least-Mean Squares method, albeit the increased complexity added by the necessity of directing an additional maximum towards a defined direction, did not demonstrated a considerable impact on its performance, as its weights reached a stable value at around the sixth iteration. Also, a brief summary of the measurements taken suing the LMS method is represented by Table 6.5.

On the other hand, the beamformer output obtained with the RLS algorithm only is concluded at about the twentieth iteration for all the intended angles, demonstrating a much slower convergence behavior than the LMS method. The measurements for the different parameter of the RLS algorithm is condensed in Table 6.6. These results can be corroborated by the track and hold capability, demonstrated by both algorithms, of the reference signal. It is shown that both methods successfully acquire and track the desired signal after approximatelly the number of iterations taken in order for the weights to stabilize.

Concerning the circular polarization characteristics demonstrated by the antenna array, some interesting results are presented. As shown by the axial ratio values, it can be seen that for angles comprised between [-20º 20º] the antenna array can not hold its circular polarization characteristics, which in turn does not pose a problem for the remaining angle span. Once again, such behavior may be explained by the non-rigorous parametrization of the dielectric constant of the FR4 substrate, which creates unpredictable radiation behaviors capable of breaking the radiation properties of the antenna. Misalignment of the array when placed in the anechoic chamber can also be a suitable explanation, due to relative flexible structure of the array, which may have been the cause of some of the measurement imprecisions verified throughout the testing phase.

6.1.1.4 Overview

This section focused on the comparison of both the Least-Mean Squares and Recursive-Least Squares algorithms, taking into account simulated and measured results, polarization characteristics and the method's convergence speed. As referenced back in Chapter 2, both these algorithms function based on a reference signal, sent from a transmitter to the receiver, that is essential to obtain the desired error signal at the receiver. For this measurement tests it was assumed that the received signal was a sinusoidal wave, as to offer a solid and predictable reference point to create a beampattern most fitted for the desired angles.

The Least Mean-Square algorithm function on the principle of updating its weight vector according to a given mean-square-error function, controlled by a scalar that controls the rate and stability at which the method converges.

As for the Recursive Least-Squares algorithm, which uses the method of least squares to update its weight vector, utilizes only the most recent data samples from the received signal, thus, theoretically, achieving faster converging rates.

The first test, where it is required to steer a single maximum towards a given direction,

shows that the normalized output obtained by both the LMS and RLS algorithms agree fairly well with the simulations and are very similar with each other, existing just a few aspects worth commenting. Results show that the measured side lobes are fairly deformed, presenting, for the most part, a larger amplitude than expected by the simulations. Also there are some, albeit minor, directivity resolution issues where the maximum of the main lobe presents a slight offset from the intended direction. These result inconsistencies may be due to various factors, being one of them the inherent properties of the algorithms used, as they are coded under the assumption that the array used is comprised of isotropic elements. The effects of using an array of highly directive microstrip antennas may not only explain this disparity but it can also be seen that for steeper angles, corroborated by the measurement tests taken for angles of interest at 60^{o} and 80^{o}, not displaying an amplitude as high as expected for more forward facing angles.

Other factors that may explain this behavior are unwanted shifts in the signal's phase introduced by the RF cables, responsible for connecting the circuit, or by fluctuations in the control voltage regulating the phase shifters functional properties, thus creating unaccounted constructive and destructive interferences during the beampattern formation process that were not present in the simulation tests.

For the single main lobe forming measuring tests, results show that the LMS algorithm has a significantly faster convergence rate than the RLS method, as its weights need less iterations in order to adopt a more stable value. Here it can be corroborated that the mean-square-error function outputs the necessary weights much faster than the method employed by the Recursive-Least Squares algorithm for these basic beamforming applications. For this test it is important to outline that the specific step size parameter used in the LMS algorithm the one presented by Equation 2.48, as it assumes that only one signal of interest is present and that all interfering signal are noise.

As for the null steering and two main lobe forming tests, the measured results show a more differentiated beampattern than that of those obtained by simulation. Unlike the previous measurement tests, here the complex weights deemed amplitude and phase adjustments necessary in order to obtain optimal directional resolution. Due to limitations in the hardware, alterations on the signal's amplitude could not be performed, resulting in outputs that were not as similar as to the simulated beampatterns. However, despite these differences, the nulls and maximums were correctly steered towards the desired angles, exhibiting only some minor directional imprecisions and divergences in the lobes amplitude, demonstrated by the measured radiation patterns of the antenna array, which may be due to the circumstances explained previously. For this measurement procedures the step size parameter utilized in the LMS algorithm was the one given by Equation 2.47, a more conventional approach for unknown environments. It can be seen that for applications where maximum and null steering functionality is required the RLS method can adapt much faster than the LMS algorithm. The RLS approach finalizes its beamforming process after about twenty-five iterations, as in contrast the LMS method only reaches convergence at about the sixtieth iteration.

Finally, tests were conducted to create two maximum lobes towards different directions. Here it was also necessary to alter the signal's amplitude, according to the weight's computed values, which could not be accomplished. It can be seen that the LMS algorithm presents, once again, a faster behavior than the RLS approach, as it only requires about ten iterations to steer the radiation pattern's beam towards the intended directions, contrary to the RLS algorithm that requires about twenty iterations to achieve a similar result, for all the defined angles.

It was also studied the right-hand circular polarization characteristic of the antenna array during the beamforming process. Results show that for all the defined angles the array was capable of performing beam steering while still holding the circular polarization property, as demonstrated by the axial ratio graphics, except for angles ranging from [-30º 30º]. Such anomalies may be due to fluctuations of the dielectric constant of the different radiating elements and structural deficiencies of the array (such as its flexibility due to the acrylic support) which may have contributed to the irregular radiation behavior of the antenna array.

6.1.2 Constant Modulus Based Algorithms Output

This section focuses on the measurement and comparison of both the Constant Modulus and Least Square Constant Modulus beamforming outputs and convergence speeds. The measurement process was divided into two main parts. The first part consisted on directing the antenna array's radiation pattern towards a single angle, which corresponded to a signal of interest. The second part focused on the beamforming capabilities of each method when multipath components were present within the surrounding environment. For ease of comparison with the measured results, simulated outputs were also included in this section.

For this measurement procedure the signal of interest was considered to be a randomly generated square wave, simulating a frequency or phase modulated signal, fed to the algorithms, as being a 32 chip sequence of ± 1 values, sampled four times per chip, shown in the Attachments . A total of 128 samples were taken from the generated signal in order to compute the complex weights necessary to the beamforming process.

This section finalizes with an overview in which is summarized the results obtained throughout the measurement tests, offering a more detailed view on the characteristics on each of the used algorithms, along with a study on the obtained beampatterns produced by the antenna array. The graphical representation of the results are present in the Attachments chapter whereas this chapter focuses on the interpretation of said results.

6.1.2.1 Beam Steering for a single θ_{SOI}

The first test was centred on the steering of a single maximum of the radiation pattern produced by the antenna array, towards a specified set of angles. First are presented the results produced by the CM algorithm, followed by the measured results obtained by the LSCM algorithm, for the same set of angles. This section concludes with brief summary of both method's measured results, comparing the directivity and convergence speeds obtained by each of the used algorithms. The antenna array's circular polarization propert is also analyzed, as to determine the polarization's quality for various different steering angles.

Constant Modulus Algorithm

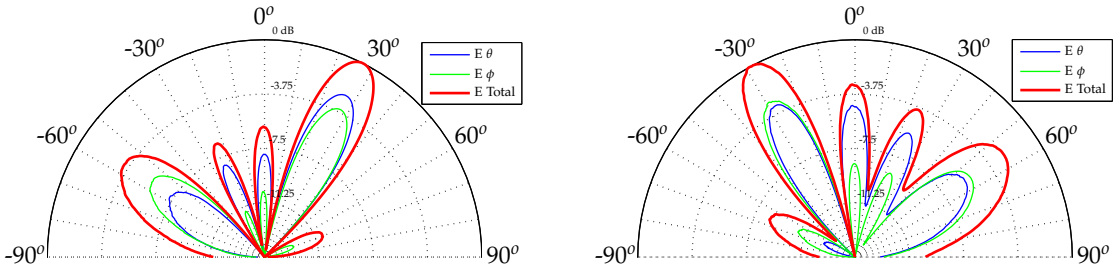

(a) (b)

Figure 6.9: Examples of measured radiation patterns for a single θ_{SOI}

Angle (θ)	Main lobe direction (θ)	Main lobe width (θ)	Distance between main and side lobes		Side lobe normalized maximum amplitude	
			Left Secondary Lobe (θ)	Right Secondary Lobe (θ)	Left Secondary Lobe (dB)	Right Secondary Lobe (dB)
0º	-2.5º	16º	29.5º	28.5º	-7.294	-6.962
30º	27º	18º	26.5º	41.5º	-5.996	-10.73
-30º	-29º	17.5º	36.5º	29.5º	-8.602	-3.125

Table 6.7: CM measured parameters

Least Square Constant Modulus Algorithm

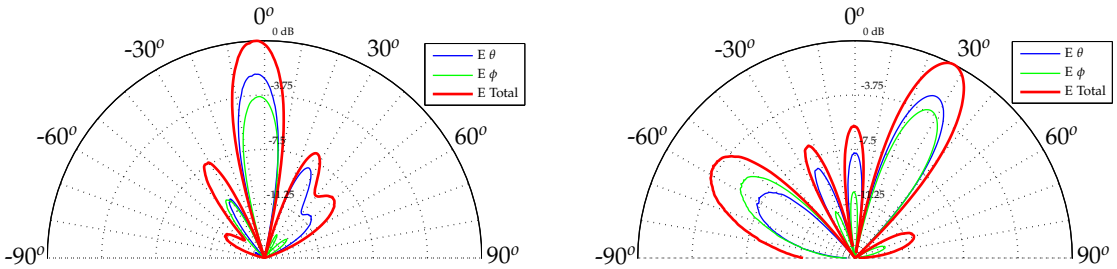

(a) (b)

Figure 6.10: Examples of measured radiation patterns for a single θ_{SOI}

Angle (θ)	Main lobe direction (θ)	Main lobe width (θ)	Distance between main and side lobes		Side lobe normalized maximum amplitude	
			Left Secondary Lobe (θ)	Right Secondary Lobe (θ)	Left Secondary Lobe (dB)	Right Secondary Lobe (dB)
0^o	-2^o	16^o	29.5^o	28.5^o	-7.374	-6.933
30^o	27^o	18^o	28^o	41^o	-5.937	-10.71
-30^o	-30^o	16^o	38.5^o	27.5^o	-9.015	-3.479

Table 6.8: LSCM measured parameters

This measurement test studied the behavior of both methods for steering a single maximum towards a given angle. The resulting beampattern from both the CM and LSCM algorithms are very similar between each other and agree fairly well with the simulation outputs, presenting only some abnormal side lobe amplitudes and minor angle offset, in accordance to the results obtained thus far. These results however present interesting results since, even though the beamformer output of each of the method closely resembles each other, their convergence rate is widely different. The Constant Modulus algorithm, for all specified angles, demonstrates a very slow weight stabilization process, requiring the whole iteration span to reach the final values required to create the intended beampattern. The obtained weights diverge slightly from each other, being this the consequence of a minor alteration to their real components, indicated by faint change of the signals amplitude calculated by the algorithm. On the other side, the Least Square Constant Modulus method reach a quasi-instantaneous solution for angles, achieving optimal solution within a very short iteration span. A more detailed overview of the measured parameters is present on Table 6.7 and Table 6.8.

As for the circular radiation property displayed by the antenna array, results show that, for the designated angles, this characteristic was lost, in a similar fashion as with the ones obtained by the beamforming output produced by the Least-Squares based algorithms.

6.1.2.2 Beam Steering for a single θ_{SOI} with multipath components

The second and final test was centred on the steering of a single maximum of the radiation pattern produced by the antenna array, towards a specified set of angles, when the system is introduced in an environment afflicted by multipath. Here, three signals with different amplitude and varying delays were created within the algorithm, shown in the Attachments chapter, as to evaluate the interference cancelation behavior of these constant modulus algorithms and how similar the resulting output signal was to the one originally received. First are presented the results produced by the CM algorithm, followed by the measured results obtained by the LSCM algorithm, for the same set of angles. This section concludes with brief summary of both method's measured results, comparing the directivity and convergence speeds obtained by each of the used algorithms. The antenna array's circular polarization property is also analyzed, as to determine the polarization's quality for various different steering angles, as is the signal outputted by each algorithm, comparatively to the received signal of interest, when used in an multipath environment.

Constant Modulus Algorithm

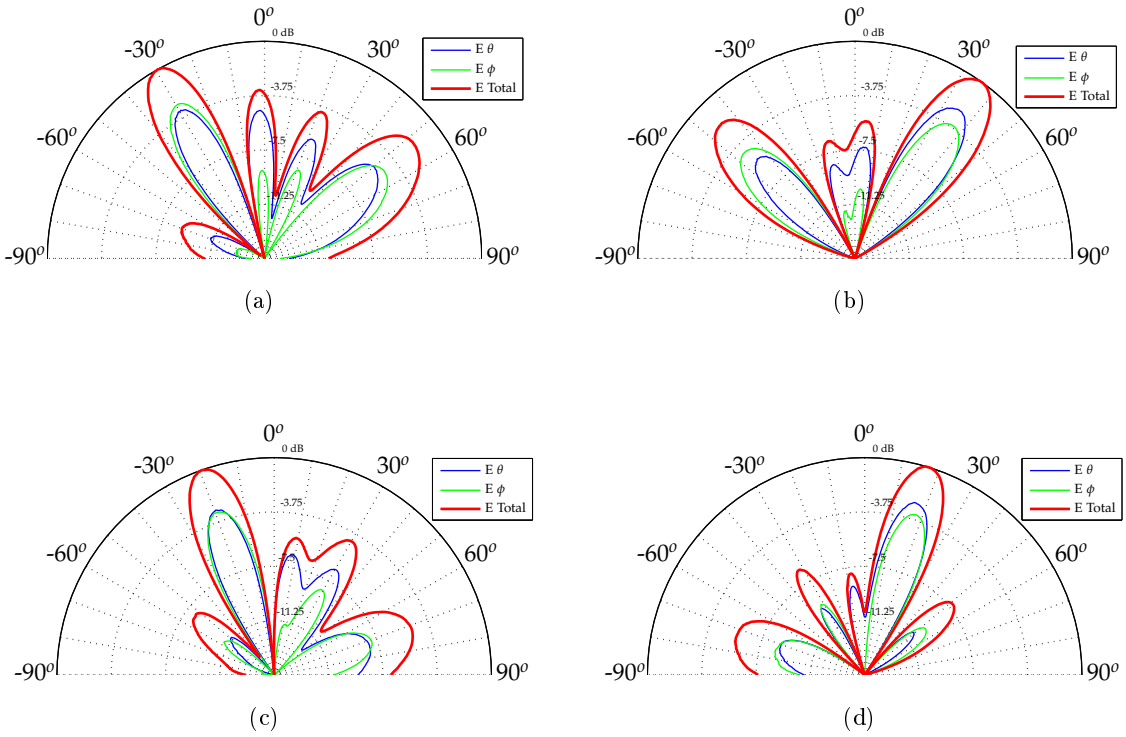

(a) (b)

(c) (d)

Figure 6.11: Examples of measured radiation patterns for a single θ_{SOI} with multipath components

Angle (θ)	Closest lobe direction (θ)	Closest lobe width (θ)	Distance between main and side lobes		Side lobe normalized maximum amplitude	
			Left Secundary Lobe (θ)	Right Secundary Lobe (θ)	Left Secundary Lobe (dB)	Right Secundary Lobe (dB)
60º	52.5º	29.5º	31º	-	-4.149	-
-45º	-45º	23º	-	32º	-	-6.684
-20º	-19.5º	17º	33º	10º	-8.176	-5.437
20º	17.5	17º	26º	33.5º	-7.978	-7.21

Table 6.9: CM measured parameters

Least Square Constant Modulus Algorithm

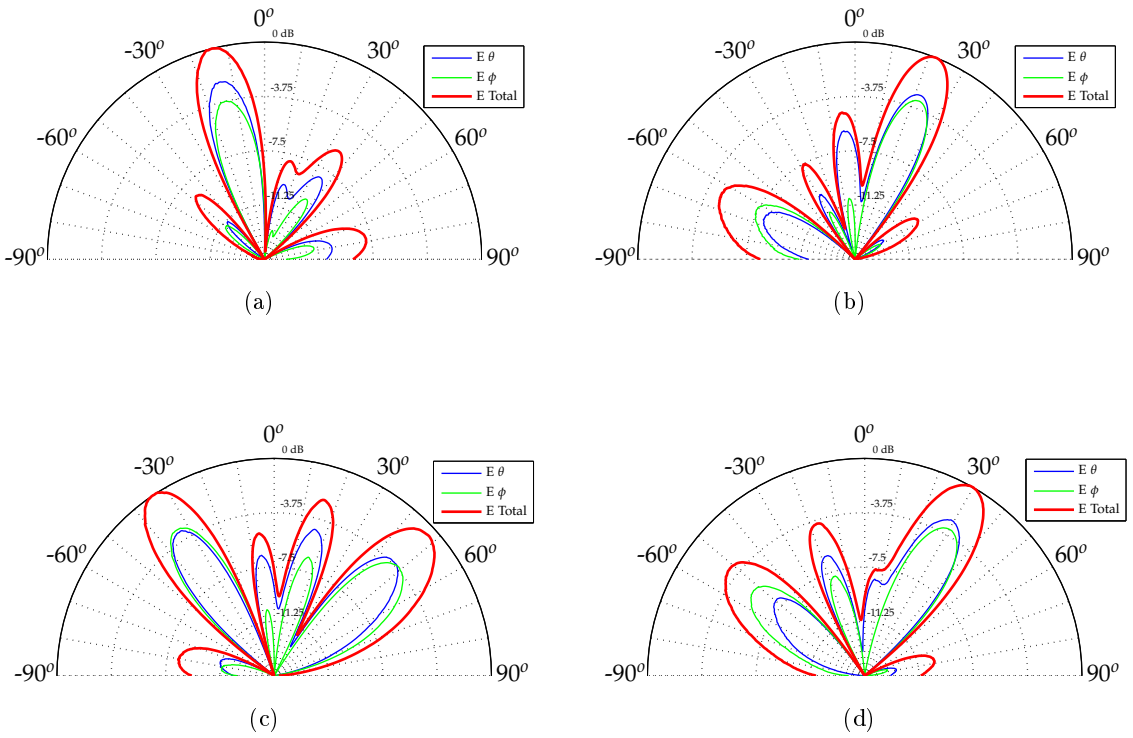

Figure 6.12: Examples of measured radiation patterns for a single θ_{SOI} with multipath components

Angle (θ)	Closest lobe direction (θ)	Closest lobe width (θ)	Distance between main and side lobes		Side lobe normalized maximum amplitude	
			Left Secundary Lobe (θ)	Right Secundary Lobe (θ)	Left Secundary Lobe (dB)	Right Secundary Lobe (dB)
60º	77.5º	33º	42.5º	-	-5.962	-
-45º	-28.5º	13º	35.5	23.5º	-4.758	-4.827
-20º	-34º	19º	46º	28º	-8.284	-5.123
20º	30º	20.5º	48º	47.5º	-4.035	-10.08

Table 6.10: LSCM measured parameters

This measurement test delivered a more comprehensive study on the behavior of the CM and LSCM methods when multipath components of the signal of interest are present within the array's surrounding environment. This test required, as consequence of the additional complexity created by the multipath components of the signal of interest, adjustments of both the phase and amplitude of each channel's signal. Once again such could not be accomplished

due to hardware limitations, being only possible to alter the signal's phase, which, in turn, resulted in a slight deviation of the measured output comparatively to the simulated results, culminating in some directional resolution degradation and beam amplitude inconsistencies.

Here it can be seen that the approach taken by both algorithms diverges greatly from each other. The Constant Modulus algorithm's output shows that, for circumstances where a multipath scenario exists, the beampattern takes a form in which the maximum is only steered towards the signal that presents larger amplitude, ignoring the received multipath components that arrive at the antenna array. On the other hand, the LSCM method not only steers the radiation pattern's maximum towards the signal of interest's direction, it also shapes the beampattern to more efficiently capture the multipath components. These results can be more clearly interpreted by Table 6.9 and Table 6.10. It can also be seen that the LSCM algorithm is capable of converging towards the Wiener solution much faster than the CM method. The complex weights calculated by the LSCM algorithm reach stable values at about the fortieth iteration for all designated angles, which for the case of the CM algorithm does not happen, as its weights only reach their final value ate the end of the given iteration span.

Concerning the circular polarization characteristics of the antenna array, the Constant Modulus algorithm is only able to maintain this radiation property when directing the radiation pattern's maximum towards 60^{o} and -45^{o} and as for the LSCM method this only holds true for -45^{o} and 20^{o}.

It is also shown that both algorithms were able to suppress, but not eliminate, the existing multipath. Three randomly generated signals, each with an associated amplitude and delay, were fed to the algorithm. Results show that both the CM and LSCM algorithms were capable of approximating the estimated received signal to the original signal of interest by exploiting its constant modulus property.

6.1.2.3 Overview

This section focused on the comparison of both the Constant Modulus and Least-Square Constant Modulus algorithms, taking into account simulated and measured results, polarization characteristics and the method's convergence speeds. These methods exploit the inherent constant modulus property of frequency and phase modulated signals, such as FM, PSK, FSK and QAM, and, as such, do not require a reference signal to generate an error signal at the receiver. This characteristic confers these constant modulus based algorithms the ability to perform 'blind' beamforming, since the exact contents of the signal do not require to be known by the receiver, by adjusting the computed complex weight values as to reduce the variation of the desired signal at the array and by providing a indirect measure quality of the filtered signal.

The single maximum steering test's results show that the normalized output created by both the CM and LSCM methods are similar to the expected beampattern obtained via simulation. There exists, however, some deformation of the side lobes, mostly presenting greater amplitude than the ones simulated. Some directivity offset was also present in the beamforming measurements, albeit less significant, as the lobe's maximum slightly deviated from the intended direction. These may be due to the very nature of the beamforming algorithms, as they were developed under the assumption that the antenna array is comprised of isotropic radiating elements, resulting in the computation of results inconsistent with the ones originated by an highly directive antenna array. Additionally, the directivity property can be

corroborated due to the incoherent magnitude behavior of the side lobes directioned towards steeper angles, as they do not reach a value as high as the ones simulated. Other factors, albeit less likely, that may justify these inconsistencies are phase fluctuations created by the RF cables, used to connect the hardware, and by a possible imperfect parametrization of the phase shifters used. The single main lobe steering measurements also show that, for equally defined step size parameters, the CM algorithm show convergence problems, corroborated by the complex weights behavior, unlike the results obtained by the LSCM method. It can be seen that the Constant Modulus technique, for all determined angles, displayed a very slow convergence speed, as the computed weights took the whole iteration span to reach their respective values. Other aspect worth noting is the abnormal values taken by said weights, surpassing all the values measured for all other studied algorithms. This erratic behavior is the result of the choice made concerning the step size parameter, taking a value larger than the one required by the algorithm to calculate the appropriate weights within the available iteration window. Simulations showed that, albeit negatively impacting the algorithm's convergence speed, the chosen value for this parameter was the one that best allowed the CM method to produce a more directive beampattern. In turn, using a smaller step size would result in a more responsive behavior, but would output a less defined maximums and nulls. As for the LSCM algorithm, it produced near instantaneous results for all defined anlged. This behavior is the result of the non-linear least-squares algorithm employed by the LSCM method, achieving convergence rates much higher than the ones outputted by the CM algorithm.

The second measurement test was conducted in order to study the behavior of each the employed methods when used under environments where multipath components of the signal of interest exist. Two multipath sources with different amplitude and delays were added, each being transmitted at a different location, in order create a composite signal with different characteristics than the one of interest. Due to the complex beam and null steering produced by the algorithm, the computed complex weights required both phase and amplitude adjustment in order to output a beampattern with optimal directional resolution. Due to hardware limitations alterations to the signal's amplitude could not be performed, resulting in outputs that were not as similar as the ones predicted by the simulations and consequently leading to radiation patterns that do not clearly display the intended simulated pattern. Other factors such the directivity and radiation characteristics of the array's elements, mentioned previously, may have also contributed to further accentuate these discrepancies. This test demonstrated two highly different behavior displayed by both algorithms in terms of pattern output and convergence speed. The CM method, similarly to the results obtained by the single beam steering tests, demonstrated a overly slow convergence behavior. Once again, the used step size parameter was not the most suitable to generate a faster response from this algorithm, albeit was the lowest one tested that could output a more directive beampattern. As for the generated radiation pattern, the Constant Modulus algorithm was only able to recover one source from the three available, directing the radiation pattern's maximum towards the angle from which the signal with the greater magnitude was being transmitted, ignoring the remaining directions. Results show that the beampattern formed by the antenna array are similar to the ones simulated, existing only minor directional offsets and side lobe magnitude inconsistencies derived by factors such as the directivity and radiation properties of the radiating elements, as previously stated, accentuated by the lack of amplitude adjustment required by the algorithm. As for the signal output generated by the CM method, it can be seen that the interference created by multipath is suppressed, but not canceled, resulting in a signal much more similar to the original.

The LSCM algorithm, on the other hand, demonstrates a much faster and dynamic behavior when handling these types of problems when compared to the CM method. Results show that for all defined angles the algorithm reached convergence in about forty iterations, demonstrating that the chosen step size parameter was qualified to allow a more responsive behavior by the LSCM method. The beampattern specified by this algorithm, contrary to the ones obtained by the CM method, not only steer the maximum towards the signal of interest's location but also steers other possible maximums towards the multipath component's arriving angles. This more complex beamforming scheme was fairly well represented by the measured beampattern produced by the antenna array, with exception for the $\theta = 60^{\text{o}}$ where maximum could not be steered towards the intended direction, existing only some minor directional resolution issues and side lobe magnitude incongruities, likely derived from the antenna's radiation and directivity properties, and the impossibility of performing amplitude modifications required by the algorithm. In terms of the output signal, the multipath was attenuated, thus shaping the signal to be transmitted by the array to be more similar to the received original signal.

Concerning the consistency of right-hand circular polarization characteristic of the antenna array during the beamforming process, results are mixed. The beampatterns produced by the CM algorithm hold the circular polarization property for all the signal of interest angles, except for $\theta = 30^{\text{o}}$ and $\theta = -30^{\text{o}}$ for the single beam steering test and for $\theta = 20^{\text{o}}$ and $\theta = -20^{\text{o}}$ for the multipath test. As for the LSCM, for the single maximum steering test, in a similar fashion as the CM method, circular polarization was not demonstrated for $\theta = 30^{\text{o}}$ and $\theta = -30^{\text{o}}$ was only present for $\theta = -45^{\text{o}}$ and $\theta = 20^{\text{o}}$. These anomalies may be explained by the different radiation properties of the antennas that constitute the array due to the flawed parametrization of their dielectric constant or by structural deficiencies of the array (flexibility as a result of the acrylic support) which may have contributed to the irregular radiation behavior of the antenna array.

6.2 DOA Measurements

The proposed setup was based on the notion of using a stationary receiver unit comprised of a circuit module capable of receiving and processing an incoming signal transmitted by a mobile source. In order to simulate a dynamic environment with a non-stationary transmitter, it was necessary to conceive an antenna capable of emulating the omnidirectional radiation properties of a RFID tag and serve as the source of the signal to be received by the antenna array.

An dipole antenna design, based on a structure created by Ricardo Dias Fernandes, a PhD student, currently working in Instituto de Telecomunicações, was deemed as a suitable replacement for the tag. The dipole antenna was created using a 1.61mm thick FR4 laminate. Contrary to the directive microstrip antennas used on the array, the dielectric constant fluctuations inherent to the FR4 laminate did not pose a problem, since this parameter is not tightly related to the radiation properties of the dipole antenna. The dipole design features two thin copper traces printed onto the FR4 substrate, each printed on an opposite side of the laminate, with a length of 64.1mm each. One arm of the dipole was displaced over the other, creating parasitic effects that improve the impedance matching required by the 50Ω SMA connector. Simulations showed that, while the behavior of the antenna is affected by the size of the dielectric which it is built upon, changes on the loss tangent or on the dielectric

constant wield little to no effect on the radiation characteristics of the dipole antenna.

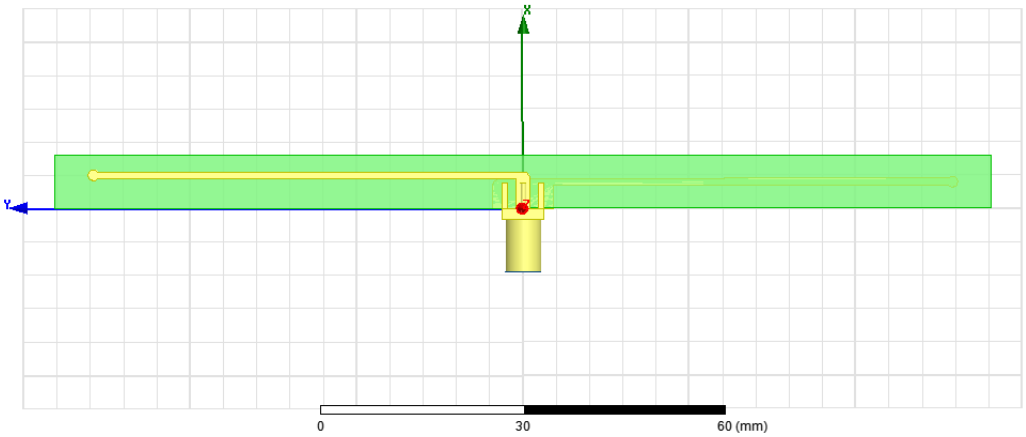

Figure 6.13: Dipole design

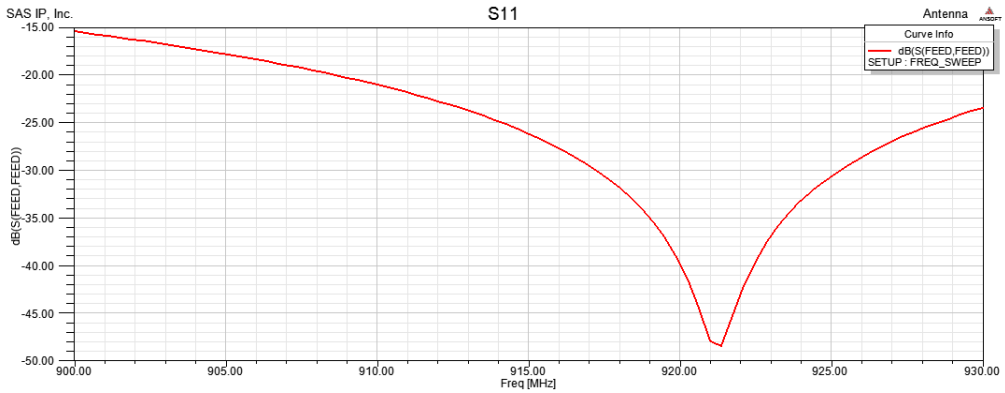

Figure 6.14: S_{11} Parameter of the dipole antenna

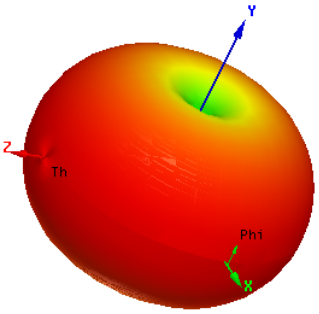

Figure 6.15: Radiation pattern of the dipole

The final dipole structure is presented by Figure 6.16

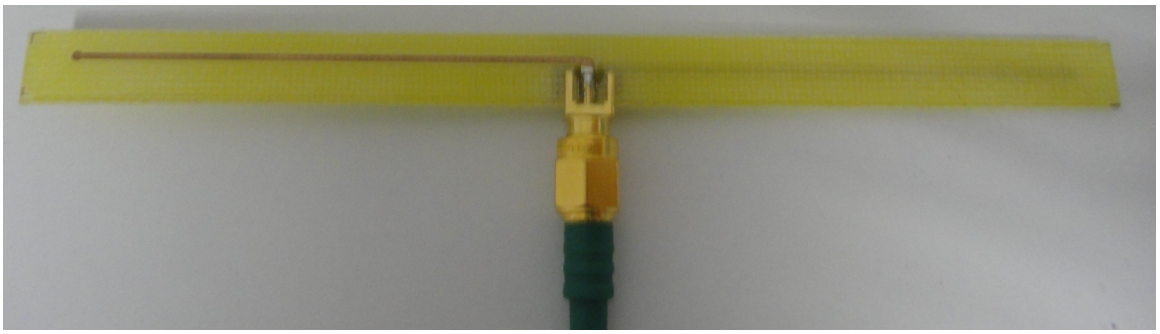

Figure 6.16: Produced dipole antenna

In order to simulate a RFID communication system, some details were taken into account. It was assumed that the dipole antenna would function as a passive tag replacement, as these tags are the most widely used for cost-sensitive applications, and thus would function based on the principles of power reflection, or backscattering, as explained in Chapter 4. Published results suggest that a typical tag integrated circuit requires around 30μW to 50μW to operate and that their performance decays as it moves farther away from the transmitter, gradually receiving less power and reaching a point which the power received is not sufficient to power up the tag's circuit[26]. A RFID system is highly dependent on the tag's performance characteristics, since it impacts the underlying functionality of the system when transmitting in forward link (reader-to tag) and in return link (tag-to-reader). These characteristics are intrinsic to the tag's structure (such as its sensitivity and backscattering efficiency), depending also on the reader and the surrounding environment (such as range and backscatter range) and can be measured as functions of frequency for different communication scenarios, such as for situations where the tag is on various materials or orientations. Of these characteristics, important forward-link parameters are the tag's sensitivity, it being the minimum incident power (signal strength) at the tag's location needed to either read or write on the tag, the tag's range, or the maximum distance at which the tag can read or written in free space[27]. These parameters can be estimated by determining the tag sensitivity, P_{tag}, needed to read or write to the tag, and can be related as[27]

$$P_{tag} = EIRP\left(\frac{\lambda}{4\pi r_{tag}}\right)^2 \tag{6.1}$$

being $\lambda$the wavelength of the RFID signal and EIRP the equivalent isotropically radiated power by the reader. American EPCGlobal standards limit RFID application's EIRP to 4W, and tests show that for this EIRP the tag sensitivity for a distance of approximately 4m is about $100\mu W$ [27]. By using Equation 6.1, the maximum distance allowed for a passive tag to be reachable can be estimated, using the following transformation

$$r_{tag} = \frac{\lambda}{4\pi\sqrt{\frac{P_{tag}}{EIRP}}} \tag{6.2}$$

In a scenario where the hypothetical parameters previously presented are applied and a 922MHz signal is transmitted, Equation 6.2 can be written as to determine an approximation of the tag's range by

$$r_{tag} = \frac{325.4mm}{4\pi\sqrt{\frac{100\mu W}{4}}} = 5.178m \tag{6.3}$$

It is important to note, however, that the write sensitivity typically differs from the read sensitivity by approximately 3dB, since the RFID tag's IC requires more power to perform write operations, and as consequence the range of read and write operations differ by about 30%[27]. These parameters were taken into account when performing the measurement test in order to simulate as closely as possible a real-world RFID communication scenario.

The receiver setup was composed by a 20GHz DPO7000 digital phosphor oscilloscope and by the produced uniform linear antenna array, discussed previously in this chapter, responsible for capturing a sinusoidal signal generated by a SMU200A Vector signal generator and emitted by the dipole antenna. The dipole antenna was placed at pre-defined angles, distantiated from the array approximately four meters, transmitting a 0dBm, 922MHz sinusoidal wave, which the antenna array captured. The signal received by each of the elements of the antenna array was forwarded to different input ports of the oscilloscope, in order to independently process the information. The oscilloscope was configured to sample the signal a rate of 12.6GHz, approximately 13.7 times the frequency of the incoming signal, and was used to save the signal's real and imaginary components received by each of the antenna's that constituted the array, that would later be used for off-line DOA estimation. The measurement setup is represented by Figure 6.17.

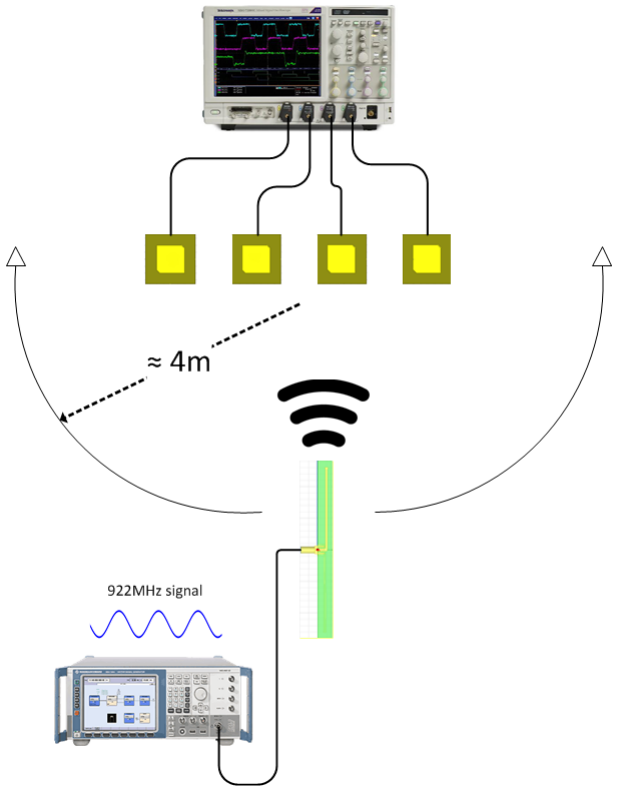

Figure 6.17: Receiver setup

6.2.1 Algorithm Measurements

This sections focuses on performing a comparative analysis of the various direction of arrival algorithms previously discussed in Chapter 2. In order to verify the consistency of the results three consecutive measurements were performed with the same conditions. In accordance to the measurement setup parameters described above, the source was placed at 0^{o} with respect to the array, at a distance of 4.1m and fed by a coaxial cable, and was afterwards placed at different predefined angles, relative to the receiver. The resolution of the MUSIC, Root-MUSIC and ESPRIT methods is here studied and discussed along with an analysis of the measurement errors.

6.2.1.1 MUSIC

The first measurement taken was for a source transmitting at a $\theta = 0^{\text{o}}$ angle. The computed spectrum is shown in Figure 6.18.

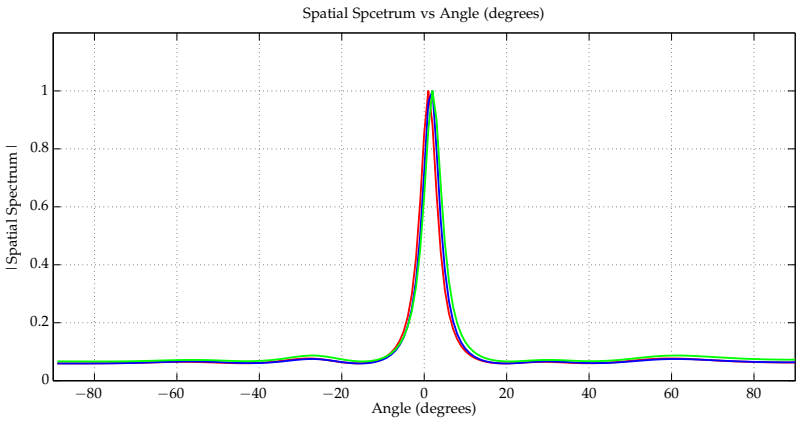

Figure 6.18: MUSIC spatial spectrum for $\theta = 0^{\text{o}}$

Angle (θ)	Measurement 1	Measurement 2	Measurement 3
0^{o}	1^{o}	2^{o}	2^{o}

Table 6.11: MUSIC angle estimation for $\theta = 0^{\text{o}}$

The peak of the spatial spectrum of the MUSIC algorithm is reached for a angle of $\theta = 1^{\text{o}}$ with no other peaks or fluctuations that could present discrepancies about which the direction the transmitter was positioned.

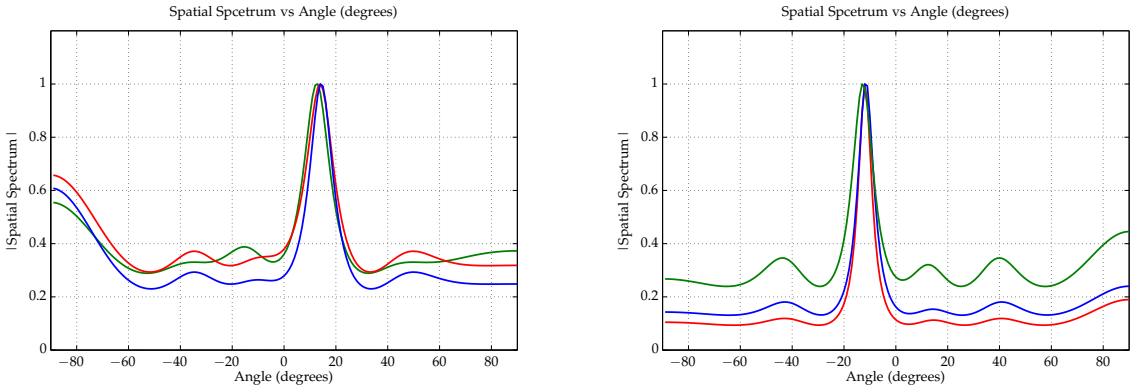

(a) (b)

Figure 6.19: MUSIC spatial spectrum for $\theta = 10^{o}$ (a) and $\theta = -10^{o}$ (b)

Angle (θ)	Measurement 1	Measurement 2	Measurement 3
-10º	-12º	-13º	-12º
10º	13º	14º	14º

Table 6.12: MUSIC angle estimation for $\theta = 10^{o}$ and $\theta = -10^{o}$

For $\theta = 10^{o}$ the MUSIC algorithm outputted a single peak, for all three measurements, very close to the pre-determined angle, with a maximum error of 3^{o}. As for $\theta = -10^{o}$ the method also correctly determined the direction in which the signal is being transmitted, with a maximum error of 4^{o}. For both measurements no additional peaks were created, thus corroborating the successful estimation of the source's position.

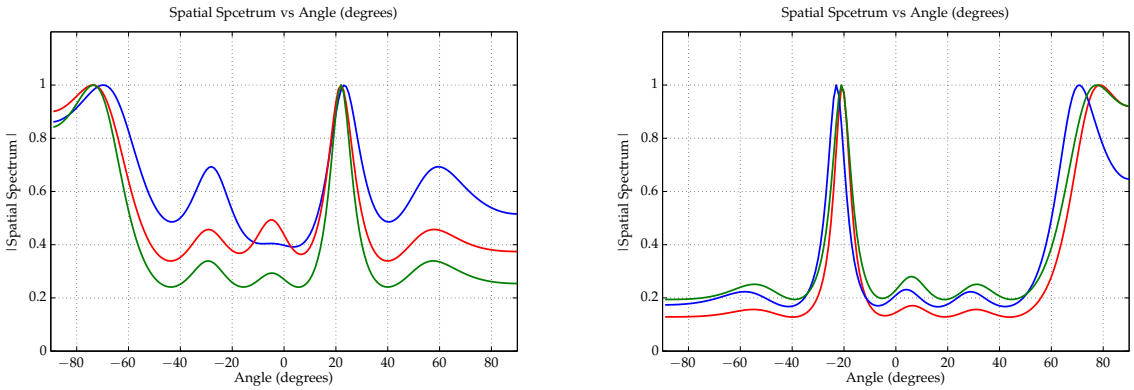

(a) (b)

Figure 6.20: MUSIC spatial spectrum for $\theta = 20^{o}$ (a) and $\theta = -20^{o}$ (b)

Angle (θ)	Measurement 1	Measurement 2	Measurement 3
-20º	-23º	-22º	-22º
20º	22º	22º	23º

Table 6.13: MUSIC angle estimation for $\theta = 20^{o}$ and $\theta = -20^{o}$

For an angle of $\theta = 20^{o}$, two peaks were computed by the algorithm, one placed correctly, with a maximum error of 3^{o}, and other situated at $\theta = -74^{o}$. In this situated the algorithm failed to accurately pinpoint the exact direction of which the signal was being sent. The same behavior is present for $\theta = -20^{o}$ as two peaks were also drawn, one on $\theta = -20^{o}$, correctly placed, and others situated at $\theta = 78, 2^{o}$ and $\theta = 69.1$. As previously occurred, the algorithm could not accurately determine the transmitter's position.

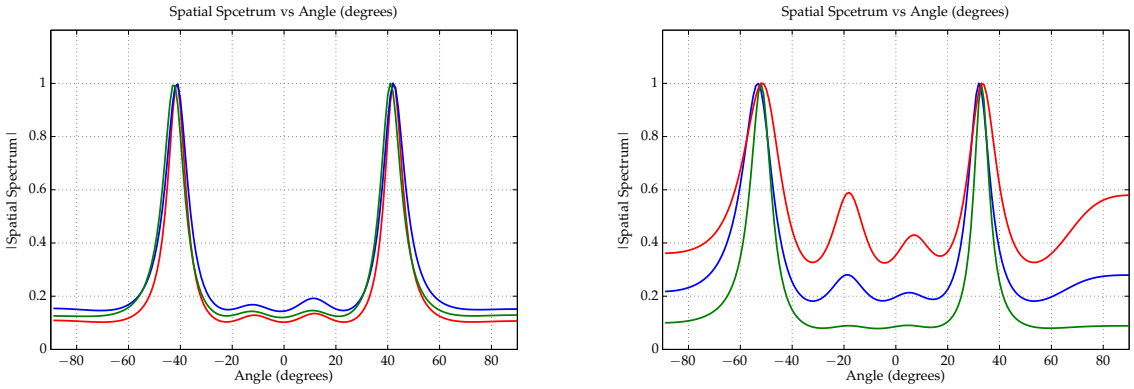

(a) (b)

Figure 6.21: MUSIC spatial spectrum for $\theta = 40^{o}$ (a) and $\theta = -40^{o}$ (b)

Angle (θ)	Measurement 1	Measurement 2	Measurement 3
-40º	-52º	-53º	-52º
40º	41º	42º	42º

Table 6.14: MUSIC angle estimation for $\theta = 40^{o}$ and $\theta = -40^{o}$

Placing the signal's source at $\theta = 40^{o}$ also produced two peaks when using the MUSIC algorithm. The outputted spatial spectrum correctly estimated the arriving angle of $\theta = 40^{o}$ with a maximum error of 2^{o} but also determines that a signal is being transmitted at $\theta = -42^{o}$, thus being unable to extrapolate the one correct direction from which the signal is being transmitted. This result inconsistency is also visible for $\theta = -40^{o}$,as the MUSIC algorithm determines that the signal is being transmitted 10^{o} off from where it is actually placed. Additionally a second angle of arrival is estimated for $\theta = 33^{o}$, which does not correspond to any existing signal used in this measurement test.

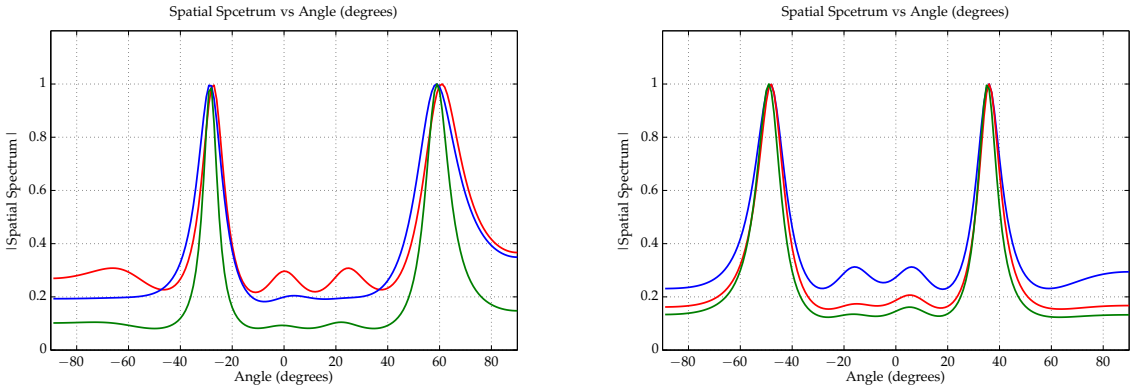

(a) (b)

Figure 6.22: MUSIC spatial spectrum for $\theta = 60^{o}$ (a) and $\theta = -60^{o}$ (b)

Angle (θ)	Measurement 1	Measurement 2	Measurement 3
-60º	-49º	-48º	-49º
60º	59º	59º	60º

Table 6.15: MUSIC angle estimation for $\theta = 60^{o}$ and $\theta = -60^{o}$

For an angle of $\theta = 60^{o}$, MUSIC determined that two signals were being received, each from a different angle. Even though the algorithm correctly positioned a peak at the transmitter's location with minimal error, it also determined that $\theta = -28^{o}$ is an angle from which a different signal is also being transmitted, which does not correspond to the reality. As for $\theta = -60^{o}$ the method displayed a larger estimation error, determining $\theta = -49^{o}$ as being the signal's position, which corresponds to an error of approximately of 10^{o}. It also estimated that a second signal, arriving from $\theta = 36^{o}$, is being received by the array, thus not being able to accurately pinpoint the source of the incoming signal.

6.2.1.2 Root-MUSIC

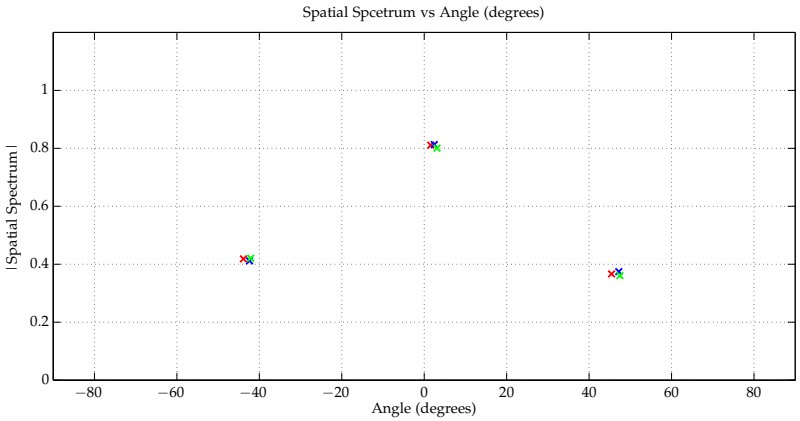

Figure 6.23: Root-MUSIC roots for $\theta = 0^{o}$

Angle (θ)	Measurement 1	Measurement 2	Measurement 3
0^{o}	2.45^{o}	1.58^{o}	-3.1^{o}

Table 6.16: Root-MUSIC angle estimation for $\theta = 0^{o}$

Results show that the calculated roots present slight variation of values for different angles comparatively to the MUSIC algorithm. For a known angle of $\theta = 0^{o}$ the Root-MUSIC algorithm was capable of discerning the correct positioning of the transmitter. The complex modulus of the normalized root for $\theta = 0^{o}$ clearly presents a higher value than the other two computed roots, correctly and unmistakeably estimating the direction of which the incoming signal was being transmitted with minimal error.

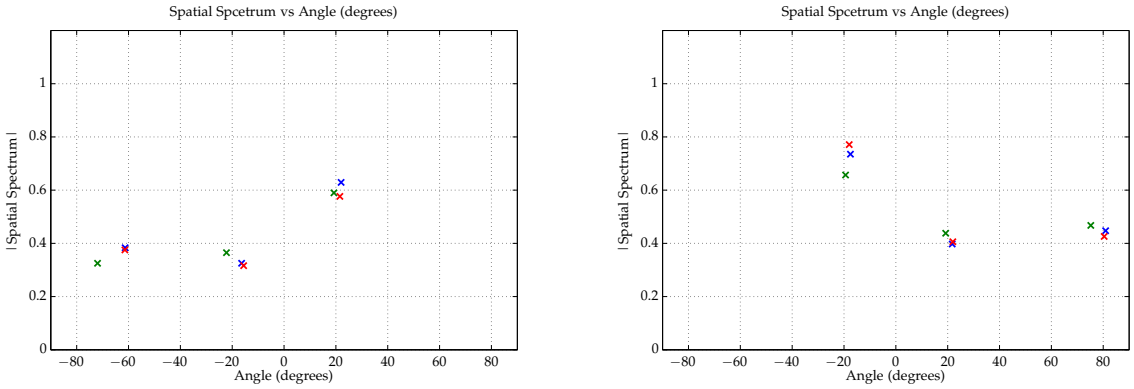

(a) (b)

Figure 6.24: Root-MUSIC roots for $\theta = 10^{o}$ (a) and $\theta = -10^{o}$ (b)

Angle (θ)	Measurement 1	Measurement 2	Measurement 3
-10^{o}	-18^{o}	-17.52^{o}	-19.39^{o}
10^{o}	22.01^{o}	19.24^{o}	21.53^{o}

Table 6.17: Root-MUSIC angle estimation for $\theta = 10^{o}$ and $\theta = -10^{o}$

For an angle of $\theta = 10^{o}$ the Root-MUSIC algorithm determined that the incoming signal was being transmitted at approximately $\theta = 20^{o}$, corresponding to a measurement error of 10^{o} relative to the actual position of the dipole antenna. As for $\theta = -10^{o}$, a similar error is introduced by the algorithm, now determining that the signal of interest was being transmitted from $\theta = -18^{o}$. Despite the relative large deviation was visible in the results obtained, the roots computed by the algorithm determined for all three measurements only one possible position for the transmitter.

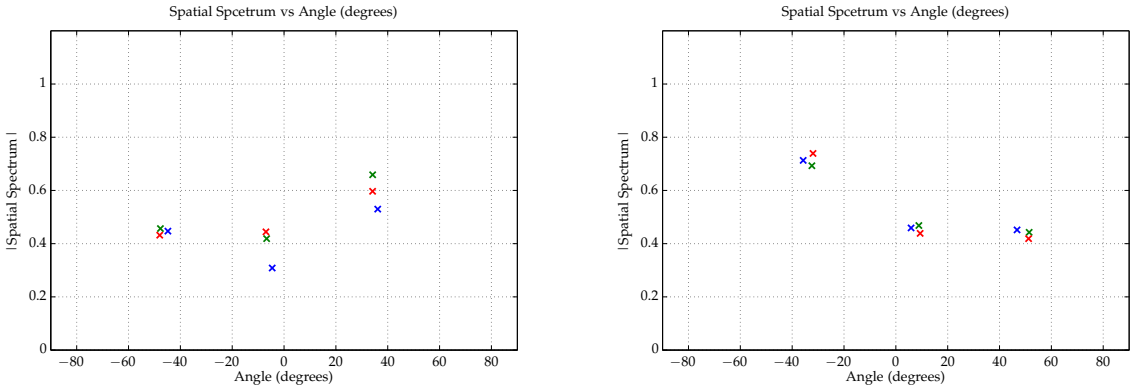

(a) (b)

Figure 6.25: Root-MUSIC roots for $\theta = 20^{o}$ (a) and $\theta = -20^{o}$ (b)

Angle (θ)	Measurement 1	Measurement 2	Measurement 3
-20º	-31.9º	-35.8º	-32.4º
20º	34.18º	34.16º	36.14º

Table 6.18: Root-MUSIC angle estimation for $\theta = 20^{o}$ and $\theta = -20^{o}$

The Root-MUSIC method, for $\theta = 20^{o}$, estimated the position of the the dipole antenna to be approximately $\theta = 34^{o}$, introducing an error of 14^{o}. For $\theta = -20^{o}$ there is also an deviation, being the estimated position approximately $\theta = -32^{o}$, corresponding to an error of 12^{o}. Albeit incorrectly estimating the precise position of the transmitter the Root-MUSIC algorithm calculated only one relevant angle in which the antenna might have being located for each measurement, contrasting with the MUSIC approach. Nevertheless, the maximum calculated error was of 15^{o}, which is inadvisable for highly directive communication systems.

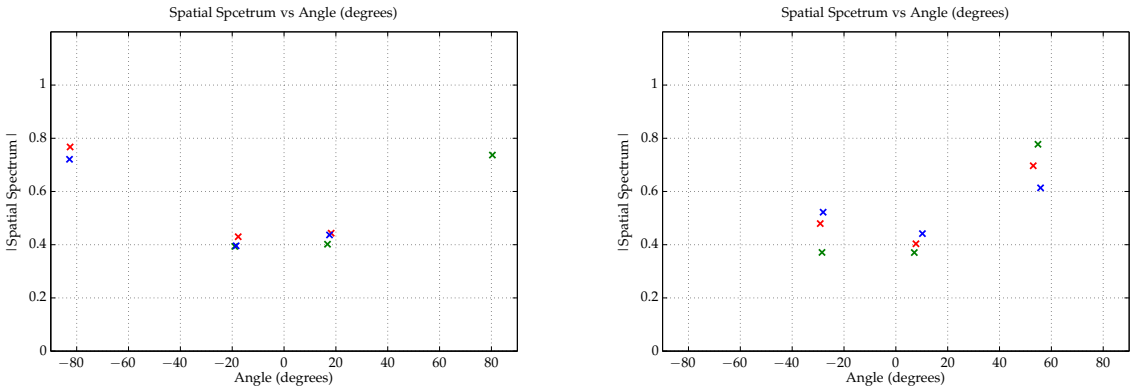

(a) (b)

Figure 6.26: Root-MUSIC roots for $\theta = 40^{o}$ (a) and $\theta = -40^{o}$ (b)

Angle (θ)	Measurement 1	Measurement 2	Measurement 3
-40º	54.83º	53º	55.83º
40º	-82.54º	80.38º	-82.8º

Table 6.19: Root-MUSIC angle estimation for $\theta = 40º$ and $\theta = -40º$

Results show highly inconsistent measurements for $\theta = 40º$, consequence of the erratic estimated angles off arrival calculated by the algorithm. Two of the measurements indicate that the arriving signal is positioned at $\theta = -82.5º$and the third shows a signal coming from $\theta = 80.38º$. The error associated with these results is very high, being the first result distantiated from the pre-determined angle by $122.5º$ and the second by $40.38º$, respectively. As for $\theta = -40º$, the results show a similar response by the algorithm, with an error of approximately $95º$ relative to the effective transmitter position.

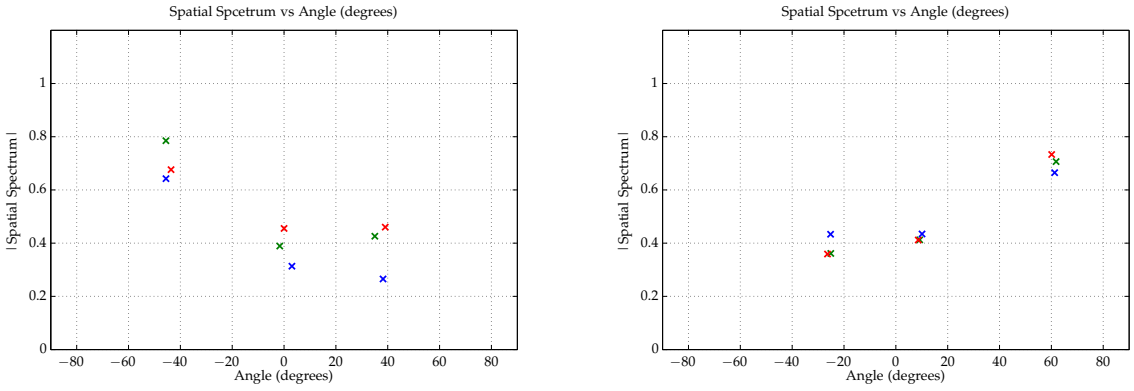

(a) (b)

Figure 6.27: Root-MUSIC roots for $\theta = 60º$ (a) and $\theta = -60º$ (b)

Angle (θ)	Measurement 1	Measurement 2	Measurement 3
-60º	60.1º	61.8º	61.3º
60º	-45.57º	-43.6º	-45.6º

Table 6.20: Root-MUSIC angle estimation for $\theta = 60º$ and $\theta = -60º$

The results obtained for $\theta = 60º$and $\theta = -60º$ demonstrate a similar problem to the previous measurement test regarding the inconsistency between the estimated angle of arrival an the effective location of the dipole antenna. For $\theta = 60º$ the Root-MUSIC algorithm estimates that the signal is being transmitted from approximately $\theta = -45º$, which in reality corresponds to an error of about $105º$. This behavior is also reflected for $\theta = -60º$, where the method determines that $\theta = 61º$ is the location from where the signal of interest is being transmitted, corresponding to a measurement error of about $121º$.

6.2.1.3 ESPRIT

The final DOA algorithm tested was ESPRIT, which estimates the position of a signal source by exploiting the rotational invariance created by any two arrays with a translational invariance structure.

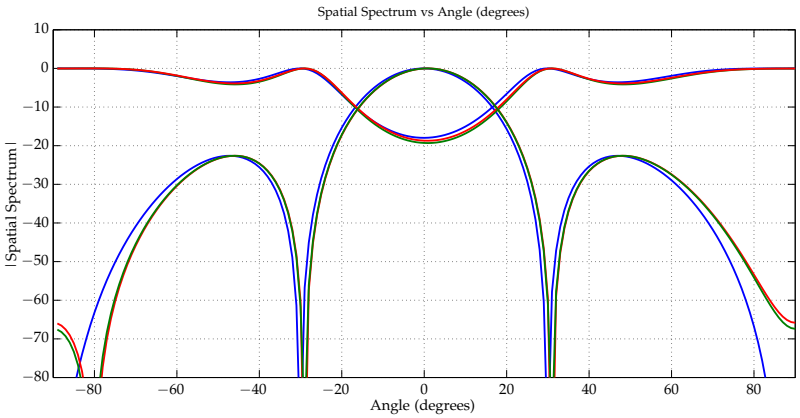

Figure 6.28: ESPRIT spatial spectrum for $\theta = 0^{o}$

Angle (θ)	Measurement 1	Measurement 2	Measurement 3
0^{o}	-0.09^{o}	0.83^{o}	0.75^{o}

Table 6.21: ESPRIT angle estimation for $\theta = 0^{o}$

Measurements show that the estimated positioning values provided by the ESPRIT algorithm are very similar to the real ones. The initial transmitter position, $\theta = 0^{o}$, resulted in an direction of arrival estimation very close to the defined one, resulting in a precise approximation with minimal errors.

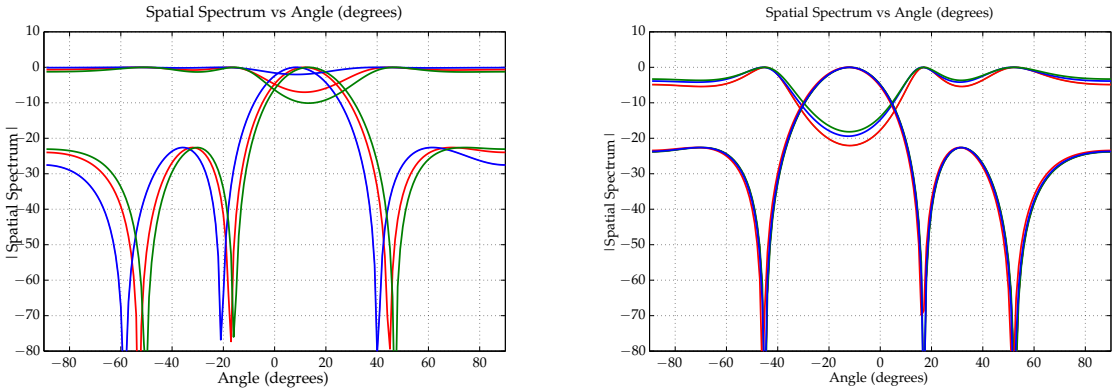

(a) (b)

Figure 6.29: ESPRIT spatial spectrum for $\theta = 10^{o}$ (a) and $\theta = -10^{o}$ (b)

Angle (θ)	Measurement 1	Measurement 2	Measurement 3
-10º	-12.72º	-12.1º	-12.2º
10º	8.9º	11.2º	13.1º

Table 6.22: ESPRIT angle estimation for $\theta = 10^{o}$ and $\theta = -10^{o}$

The measurement test for $\theta = 10^{o}$ and $\theta = -10^{o}$ also wielded satisfactory results. For each of the defined angles of arrival, the ESPRIT algorithm was capable of accurately determine the position of the signal's source with an error that it is not superior to 3^{o}.

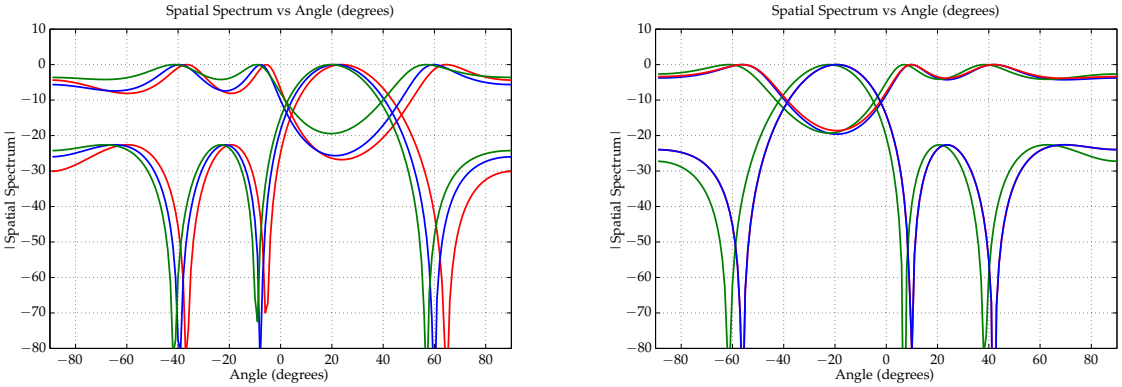

(a) (b)

Figure 6.30: ESPRIT spatial spectrum for $\theta = 20^{o}$ (a) and $\theta = -20^{o}$ (b)

Angle (θ)	Measurement 1	Measurement 2	Measurement 3
-20º	-19.29º	-22.24º	-19.31º
20º	19.67º	21.37º	21.71º

Table 6.23: ESPRIT angle estimation for $\theta = 20^{o}$ and $\theta = -20^{o}$

For $\theta = 20^{o}$, the angle calculated by the ESPRIT method was very similar to one determined, with a maximum inaccuracy of 1.71^{o}. Finally, for $\theta = -20^{o}$, the result computed by the algorithm was also very close to the actual position of the dipole antenna, with a maximum measurement error of 2.24^{o}.

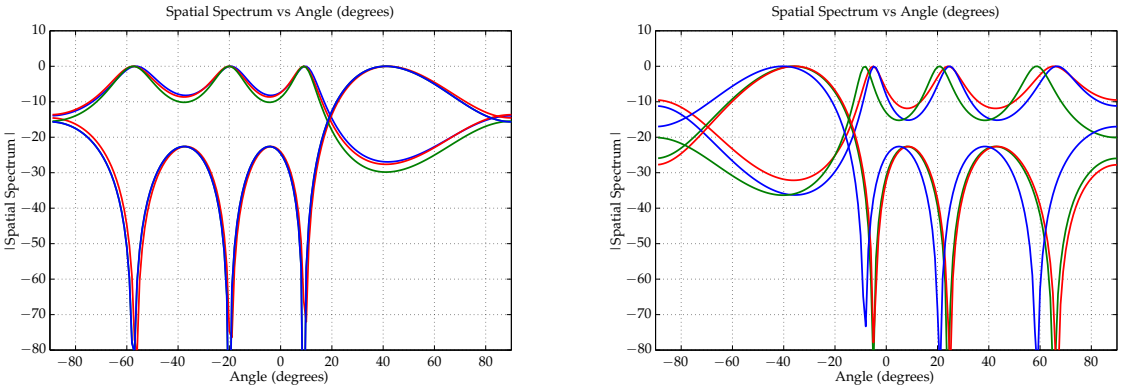

(a) (b)

Figure 6.31: ESPRIT spatial spectrum for $\theta = 40^{o}$ (a) and $\theta = -40^{o}$ (b)

Angle (θ)	Measurement 1	Measurement 2	Measurement 3
-40º	-34.8º	-32.42º	-37.66º
40º	39.67º	41.43º	40.56º

Table 6.24: ESPRIT angle estimation for $\theta = 40^{o}$ and $\theta = -40^{o}$

Results for $\theta = 40^{o}$ show that the algorithm correctly determined the angle of arrival of the signal of interest, only revealing a slight inaccuracy of 1^{o} maximum. As for $\theta = -40^{o}$, measured results demonstrate that a greater error was introduced during the angle calculation, estimating that the transmitter's position was about $\theta = -33^{o}$, corresponding to an error of approximately 7^{o}.

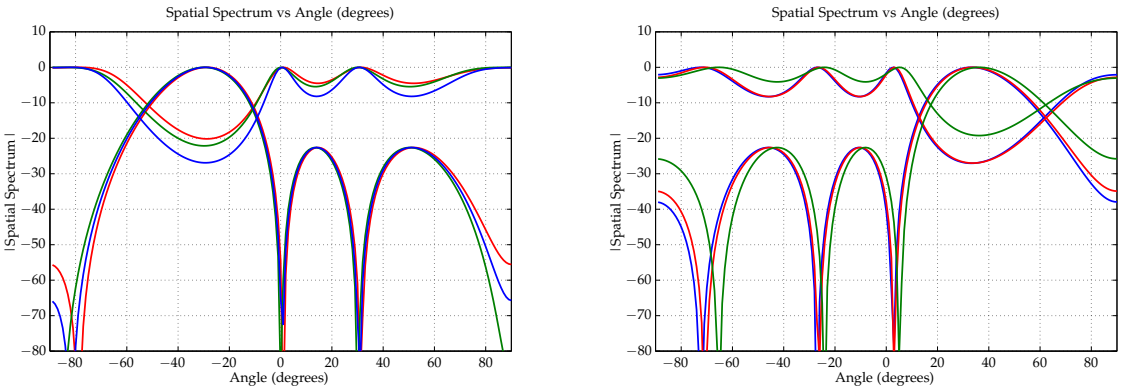

(a) (b)

Figure 6.32: ESPRIT spatial spectrum for $\theta = 60^{o}$ (a) and $\theta = -60^{o}$ (b)

Angle (θ)	Measurement 1	Measurement 2	Measurement 3
-60º	36.11º	33.77º	33.19º
60º	-33.11º	-33.78º	-33.19º

Table 6.25: ESPRIT angle estimation for $\theta = 60^{\circ}$ and $\theta = -60^{\circ}$

The final measurement test was realized for $\theta = 60^{\circ}$ and $\theta = -60^{\circ}$ and shows very inconsistent results. For $\theta = 60^{\circ}$ the ESPRIT method determined the probable position of the dipole antenna was approximately $\theta = 33^{\circ}$, thus not being able to accurately determine the correct angle from which the signal was being transmitted. The same behavior was reflected for $\theta = -60^{\circ}$, as the algorithm was incapable of discerning the correct position of the transmitter. Overall, this test outputted results that were approximately 90° off from the predefined angles.

6.2.2 Overview

This section focused on the study of the MUSIC, Root-MUSIC and ESPRIT algorithms and their ability to discern the angle of arrival of a given signal of interest. These DOA estimation methods function on the principle of modeling the incident signal as a plane wave, assuming that the propagation conditions do not change as the wave traverses the full extent of the antenna array.

The DOA measurement results presented throughout this section show that all three methods were capable of accurately estimate the angle of arrival of the signal of interest when its source was positioned at $\theta = 0^{\circ}$ and $\theta = \pm 10^{\circ}$. However, for the remaining angles, each algorithm presented different results.

The MUSIC algorithm, for $\theta = 0^{\circ}$ and $\theta = \pm 10^{\circ}$, correctly estimated the angle from which the signal's source was positioned, with a maximum error of 4°. The outputted spatial spectrum only displayed one peak for each of the angles, each centered at the estimated angle. For $\theta = \pm 20^{\circ}$, despite correctly determining the transmitter's position, the method outputted a spatial spectrum which contained two peaks, one positioned at the correct angle and other positioned at $\theta = -74^{\circ}$, for $\theta = 10^{\circ}$, and the second at $\theta = 78.2^{\circ}$, for $\theta = -10^{\circ}$. This behavior became more apparent for the $\theta = \pm 40^{\circ}$ and $\theta = \pm 60^{\circ}$ measurements, as the peaks became more pronounced, consequently impossibilitating, even though one of the peaks was correctly positioned within the determined spatial spectrum, a precise and definitive estimation of the signal of interest's angle of arrival.

The Root-MUSIC, on the other hand, was able to output only one estimated angle per measurement, with the disadvantage that the error of these estimations was more pronounced than those of MUSIC's. For $\theta = 0^{\circ}$ results showed a negligible maximum error of 3°. As for $\theta = \pm 10^{\circ}$, the error increased, now being of approximately 10° for each of the measurements. This behavior became even more apparent for $\theta = \pm 20^{\circ}$, failing to precisely estimating the angle of arrival by a margin of about 15° for each of the measurements taken. Finally, for $\theta = \pm 40^{\circ}$ and $\theta = \pm 60^{\circ}$, the algorithm outputted highly inconsistent results relative to the ones established. Here, the Root-MUSIC failed to estimate the direction from which the signal was being transmitted, outputting large measurement errors and completely failing to correctly estimate the origin of the received signal.

The ESPRIT method showed a more consistent behavior compared to the other two tested algorithms. For all established angles, the ESPRIT algorithm was able to correctly estimate all of the signal's positions, with a maximum error of 6°, except for $\theta = \pm 60^{\circ}$. In this

measurement the algorithm incorrectly estimated the direction from which the signal was being transmitted, failing in pinpointing the actual position of the transmitter.

The poorer performance of these algorithms may be due to multiple causes. The conducted measurement test was performed within a closed space, populated by tables, shelves and RF equipment, all contributing to the formation of multipath components of the transmitted signal. The phase variations captured by the antenna array due to the existence of multipath may have degraded the performance of the system and overloaded the array, leading to the failure of the angle of arrival estimation algorithms. In other words, the reflections produced within the array's surrounding environment created rays that arrived at the receiver at unknown angles, causing errors in the estimate of the direction of arrival of the known angle. Other possible cause for measurement errors is the mutual coupling effect between the array's elements.

Additionally, by utilizing an highly directive antenna array, the signal arriving from a source positioned from a steeper angle may have not be captured as well as a signal being transmitted from a more forward facing position. The array's radiation pattern, presented in Figure 5.15, gives an indication of which angles the array can best receive incoming signals. In accordance with the results presented in this tests, for angles ranging from [-10º 10º], the array is capable of receiving signals with a maximum attenuation of 3,13dB, corresponding to the maximum of the radiation pattern. This is coherent with results obtained for this range of angles, since minor errors were found for the estimated angles. For $\theta = \pm 20^{\text{º}}$, according to Figure 5.15, incoming signals experience a 15dB attenuation, possibly leading to an incorrect reading of the received signal, which is may be demonstrated by the multiple peak formation in the MUSIC's spatial spectrum or by the increased error measured by the Root-MUSIC algorithm. As for $\theta = \pm 40^{\text{º}}$ and $\theta = \pm 60^{\text{º}}$, the array's radiation pattern's measurements show an attenuation of approximately 22dB and 17dB, respectively, capable originating ambiguous angle estimations such as the ones measured by the three algorithms.

6.2.3 Combined Signal at the Receiver

The process of determining the angle of arrival of a determined signal is a complex process, vulnerable to various error inducing factors, produced the communication system's surrounding environment or by characteristics intrinsic to the algorithm or to the used antenna array, that may compromise the correct signal analysis by the receiver. Some of these factors were previously discussed, such as the presence of multipath components of the transmitted signal and the radiation properties of an highly directive antenna array, causing the receiver to capture random phase and amplitude fluctuations from the incoming signal. The unstable nature of such environments imposibilitate the receiver to properly discern the signal source's placement throughout the communication process and make the reading of the received composite signal a challenge when proper amplification stages are not properly implemented.

For a communication environment not afflicted by multipath, the behavior of the received signal can be studied when captured by an uniform linear array by the equation, presented in Chapter 1,

$$\triangle\Psi = 2\pi \frac{d \sin\theta_s}{\lambda} \tag{6.4}$$

being $\Delta\Psi$ the signal's phase shift present at each of the array's elements, d the distance between adjacent elements of the array, θ_s the angle from which the signal is being transmitted

and λ the signal's wavelength. For a 4-element ULA, with a spacing of 0.75λ between each of its elements, receiving a 922MHz signal from a given angle θ_s, Equation 6.4 can be rewritten as

$$\triangle\Psi = (N-1)2\pi\frac{0.75\lambda\sin\theta_s}{\lambda} \times \frac{180}{\pi} = (N-1)2 \times 0.75\sin\theta_s \times 180 \quad N = 1, 2, ..., N \quad (6.5)$$

where N is the number of elements that are present in the array.

The following test focused on the study of the behavior of the received signal, when each of its components are combined, relative to the angle from which the transmitter is broadcasting the signal, following the smart antenna's receiver architecture discussed in Chapter 1.

The setup for the measurement test had as a base the phase shifting board, shown in Chapter 5, which, via variations of the phase shifter's control voltage, introduced a shift in each channel's signal, emulating the response obtained if the array antenna would capture a signal of interest whose source would be located at θ_s. This setup, represented in Figure 6.33, is composed by a SMU200A vector signal generator, responsible for generating a 0dBm, 922MHz sinusoidal wave, linked to a ZN8PD1- 53-S+ power splitter. Each of the splitted signals were fed to the phase shifting board and were finally analyzed by a 20GHz DPO7000 digital phosphor oscilloscope.

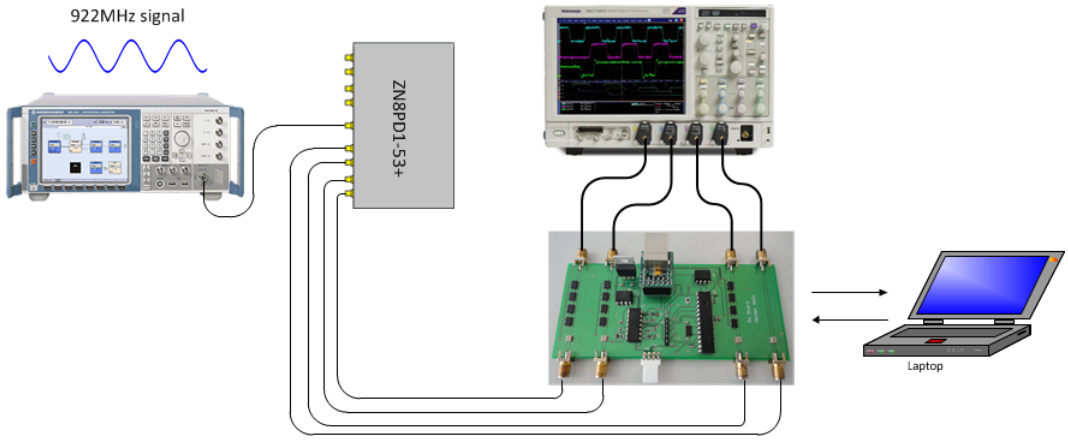

Figure 6.33: Measurement Setup

Each of the signal's amplitudes were first measured, as indicated by Table 6.26. Next, it as introduced in each signal a phase shift, in accordance to Equation 6.5, as to simulate the receiver's response to a source positioned at a given angle θ_s, and the sum of each component was performed. Results are shown below.

Amplitude(Ch1)	Amplitude(Ch2)	Amplitude(Ch3)	Amplitude(Ch4)
80.0mV	73.29mV	82.0mV	82.0mV

Table 6.26: Measured signal amplitude of each channel

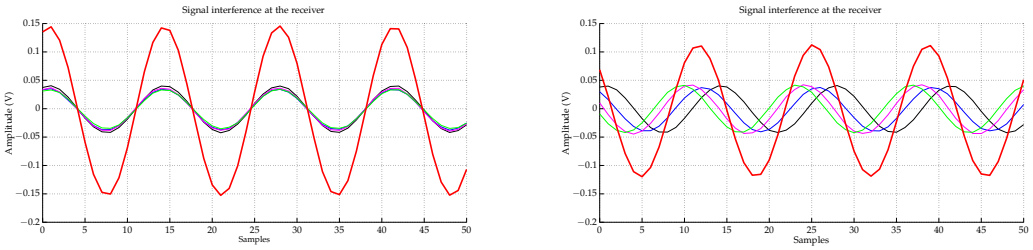

(a) (b)

Figure 6.34: Signal amplitude for $\theta = 0^{o}$ (a) and $\theta = 10^{o}$ (b)

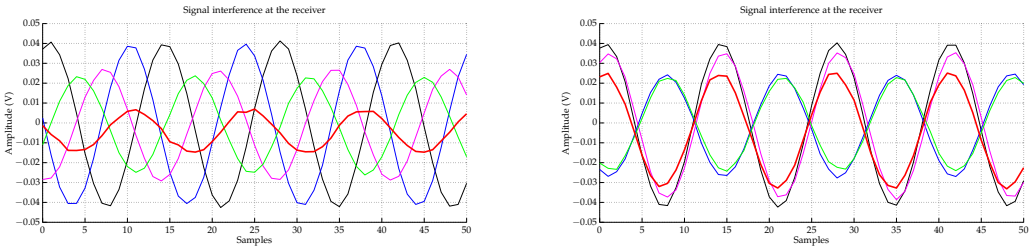

(a) (b)

Figure 6.35: Signal amplitude for $\theta = 20^{o}$ (a) and $\theta = 40^{o}$ (b)

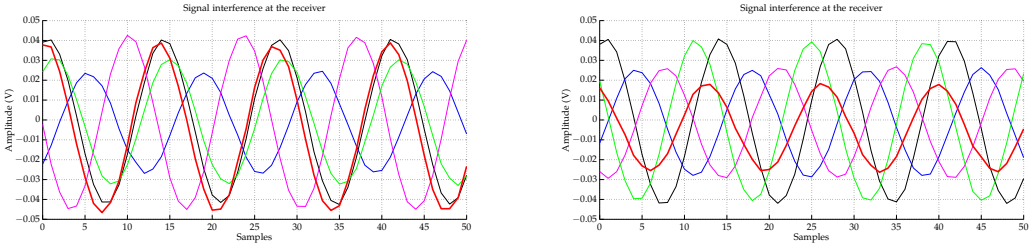

(a) (b)

Figure 6.36: Signal amplitude for $\theta = 60^{o}$ (a) and $\theta = 80^{o}$ (b)

	$\theta = 0^{o}$	$\theta = 10^{o}$	$\theta = 20^{o}$	$\theta = 40^{o}$	$\theta = 60^{o}$	$\theta = 80^{o}$
Phase(Ch2,Ch1)	2.747°	54.64°	107.6°	172.2°	-128.7°	-96.76°
Phase(Ch3,Ch1)	1.318°	94.96°	-171.3°	-13.61°	111.2°	177.7°
Phase(Ch4,Ch1)	1.244°	121.9°	-94.1°	163.5°	-17.43°	83.59°
Amplitude(Sum)	295.2mV	230.7mV	21.01mV	55.27mV	82.49mV	35.96mV

Table 6.27: Measured signal parameters for different angles of arrival

As expected, due to the constructive and destructive summation of the different signals, each corresponding to a phase shifted version of the signal of interest captured by an individual element of the array, the received signal experiences considerable amplitude changes depending

on the position of radiating source. For $\theta = 0^{o}$ and $\theta = 10^{o}$, the amplitude of the combined signals reaches a value close to the maximum one possible, since the shift in phase of the signals is in such a way that the sum of the signals creates more of a constructive behavior than of a destructive one. As for the remaining angles, it is visible a significant impact in the signal's amplitude due to destructive summation, as a consequence of phase opposition between the different signal's components. This reduced amplitude may cause incorrect readings from receivers employing uniform linear arrays, if proper measures to deal with this issue are not employed. Smart antenna systems, by employing spatial filtering via beam forming, can overcome the destructive summation effects originated when the array receives signals from positions at steeper angles relative to the receiver.

Chapter 7

Conclusion and Future Work

7.1 Summary and Conclusions

The worked developed in this thesis consisted on the creation of a system capable of performing beam steering and direction of arrival estimation tasks, using a four element uniformly spaced linear antenna array as medium, developed and tested to operate at a working frequency of 922MHz.

The antenna developed, given its particular radiation and polarization characteristics, was subjected to various simulations in order to achieve better gain and efficiency, always taking into account how these changes would affect its radiation pattern's directivity.

The first phase of this project was based on the study of microstrip antennas, in particular about simple microstrip patch antenna design and feeding methods, complemented with an increase in proficiency using electromagnetic simulator software, namely HFFS and ADS. Structure and feeding methods were compared, being the coaxial-probe feeding method ultimately selected by its more simplistic and appropriate implementation and better radiation characteristics.

Next it was imposed right-hand polarization into the antenna, by changing the structure of the patch (chanfering two opposite corners of the antenna) and adjusting, via multiple simulations, in order to achieve good axial ratio values. The microstrip antenna was developed to have an optimal polarization and radiation properties for a working frequency of 915MHz, contained within the american RFID frequency band. Variable dielectric constant values posed a challenge, since a reliable way to achieve optimum impedance matching became difficult and uncertain. For this reason various prototypes were fabricated and tested. The final microstrip antenna model had good impedance matching and polarization characteristics for a frequency of 922MHz.

Once the tests of the single antenna element were finished, an uniform linear array comprised of four antennas was designed and simulated. By varying the spacing between the array's elements it was possible to determine the best morphology to achieve optimum directivity and circular polarization characteristics. The results relative to the radiation pattern and polarization were close to the ones intended and, as such, the antenna array was constructed.

Parallel to the development phase of the antenna, a smart antenna based system was being considered. The system would estimate de direction from which a transmitter was emitting a signal and would calculate the weights necessary to insert onto the antenna array in order to

generate a radiation pattern where the main lobe is steered towards the point of interest.

A prototype board, composed by an control module and a phase shifting module was created as an initial functional scheme, that would later be enhanced in order to achieve better transmission and reception results.

Various algorithms specialized in weight calculation were available, being selected for this work only four: Least-Mean Squares, Recursive Mean-Squares, Constant Modulus and Least Square Constant Modulus. The Least-Mean Squares algorithm presented an initial overview of the basic beamforming principles, since it is a robust, low-complexity technique that is widely used by several communication systems. Although simple, the convergence speed of the algorithm when performing more complex tasks, like null steering, was slow. The Recursive Mean-Squares, although capable of performing complex beamforming operations in less time, entails a larger computational load, required by superior number of complex multiplications needed. The two constant modulus based algorithms were developed in order to provide a testing ground for multi-signal applications and were especially useful in systems employing frequency and/or phase modulation. The multipath suppression capability was tested in order to determine its usefulness for applications that require active RFID tags, granting an added layer of quality to the communication scheme employed by offering superior noise cancellation and spectral efficiency.

All these techniques presented beamforming outputs very similar to each other. The only parameter that differentiated these algorithms was the necessary iteration span until the computed weights could become stable, thus marking the convergence of the algorithm. Measurements showed that between the Least-Squares based algorithms the one that achieved convergence faster was the LMS method, for the one and two beam steering tests, ans the RLS for the single beam and null steering. A for the constant modulus based algorithms, the LSCM consistently demonstrated that could achieve faster convergence speeds than the CM method, using similar step size parameters, being even able to achieve convergence almost instantly for the defined angles. On the other hand the LSCM algorithm when used to steer a single maximum had difficulties in stabilizing its weights. As for CM algorithm, the convergence speed of this method was the worst among all the ones studied. It took about all the algorithm's iteration span to achieve convergence, thus not being the most suitable for high-speed dynamic environments. Additionally, the circular polarization characteristic of the antenna array was analyzed when the system was performing beamforming. It was shown that this polarization property did not displayed a consistent behaviour, as for different angles the antenna array demosntrated axial ratio values greater than the maximum one recommended.

Subspace-based algorithms for direction of arrival estimation were also studied and implemented, being them MUSIC, Root-MUSIC and ESPRIT. The performance of each of these techniques was analyzed and compared. From all of these methods, ESPRIT was the most consistent, as it pinpointed the direction of arrival of the signal's source with the least associated error. The MUSIC method also was capable of determining the correct position of transmitter, although its computed spatial spectrum showed additional non-existing transmission angles via the creation of additional peaks. Finally, the Root-MUSIC algorithm was capable of limiting the angle estimation to a single angle of arrival, much like the ESPRIT method, but it was the method that most was affected by measurement errors, computing the direction of arrival of incoming signal from an angle up to 15° deviated from the original source.

Finally shifts in each of receiver's channels were introduced in order to better understand the behavior of the signal of interest signal when when transmitted from various angles. The

results obtained show that depending on the location of the signal's source, the amplitude of the signal resulting from the summation of different components of the transmitted signal varies greatly, underlying the importance of both amplification and phase shifting stages on receivers in order to better read the signal of interest.

7.2 Future Work

The worked developed throughout this thesis can benefit from several enhancements, being some of them:

- Improvement of the antenna array, namely to reduce the number of secondary lobes, enhance directionality and achieve better circular polarization characteristics. One such way to achieve these objectives would be to increase the number of elements that constitute the array.
- Creation of an array using a substrate with better dielectric constant characteristics, in order to create a more reliable and robust antenna. Also, creating an array of dipole antennas in order to compare beamforming output values with a directive antenna arrays.
- Constructing an unified circuit capable of performing beamforming tasks autonomously while being capable of receiving and transmitting UHF signals independently.

Bibliography

[1] Constantine A. Balanis and Panayiotis I. Ioannides. Introduction to smart antennas. 2(1):1–175.

[2] Gabriele Manganaro and Domine Leenaerts. Wireless infrastructure. In *Advances in Analog and Rf Ic Design for Wireless Communication Systems*, pages 1–6. Elsevier.

[3] Constantine A Balanis. *Antenna theory: analysis and design.* Wiley Interscience.

[4] Classification of polarization.

[5] History of RFID.

[6] Klaus Finkenzeller. *RFID handbook: fundamentals & applications in contactless smart cards & identification.* Wiley-Blackwell.

[7] V. Daniel Hunt, Albert Puglia, and Mike Puglia. *RFID: a guide to radio frequency identification.* Wiley-Interscience.

[8] Stuart J Allen, David L Brock, and Edmund W Schuster. *Global RFID the value of the EPCglobal network for supply chain management ; with 8 tables.* Springer.

[9] Kecia Lynn. With this device, employees' RFID badges really aren't safe.

[10] Via verde.

[11] Active RFID tags - active RFID tags exporter, manufacturer, distributor & supplier, mumbai, india.

[12] Paul Sanghera. *How to cheat at deploying and securing RFID.* Syngress Pub.

[13] RFID standards :: Radio-electronics.com.

[14] Jari-Pascal Curty. *Design and Optimization of Passive UHF RFID Systems.* Springer.

[15] Lal Chand Godara. *Smart antennas.* CRC Press.

[16] Robert P. Neuman and Roland Cavanagh. *Smart Antennas for Wireless Communication.* McGraw Hill Professional.

[17] Jeffrey Foutz, Andreas Spanias, and Mahesh K. Banavar. Narrowband direction of arrival estimation for antenna arrays. 3(1):1–76.

[18] Antenna polarization | polarisation basics tutorial | radio-electronics.com.

[19] Nemai Chandra Karmakar. *Handbook of smart antennas for RFID systems.* Wiley.

[20] Syed Ahson and Mohammad Ilyas. *RFID handbook: applications, technology, security, and privacy.* CRC Press.

[21] James B Ayers. *Handbook of supply chain management.* Auerbach Publications.

[22] *RFID security.* Syngress.

[23] Daniel Mark Dobkin. *The RF in RFID passive UHF RFID in practice.* Elsevier / Newnes.

[24] Albert Lozano-Nieto. *RFID: design fundamentals and applications.* CRC Press.

[25] Klaus Finkenzeller. *RFID handbook fundamentals and applications in contactless smart cards and identification.* Wiley.

[26] Link budgets.

[27] P.V. Nikitin and K.V.S. Rao. LabVIEW-based UHF RFID tag test and measurement system. 56(7):2374–2381.

Attachments

Prototype Control Module Schematic

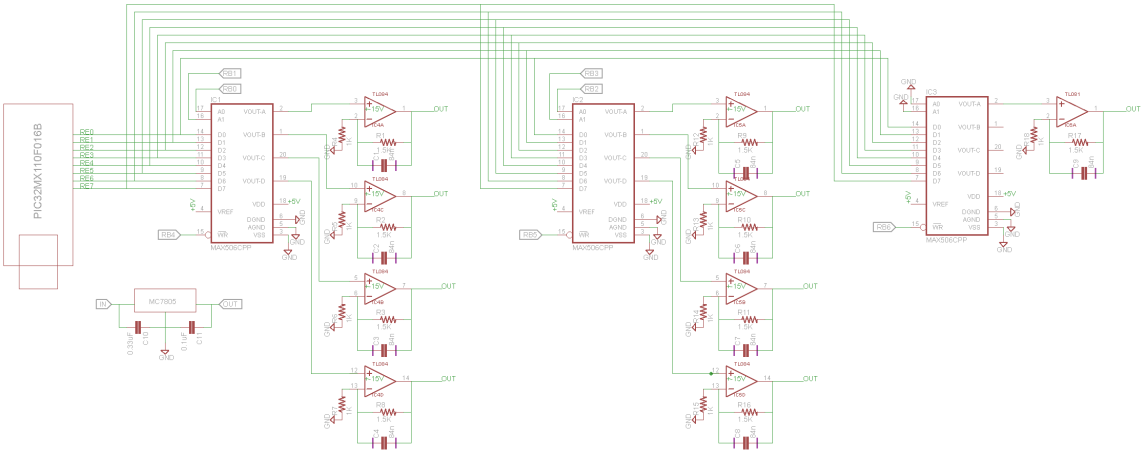

Figure 7.1: Initial circuit schematic of the control module

Prototype Phase Shifting board layout

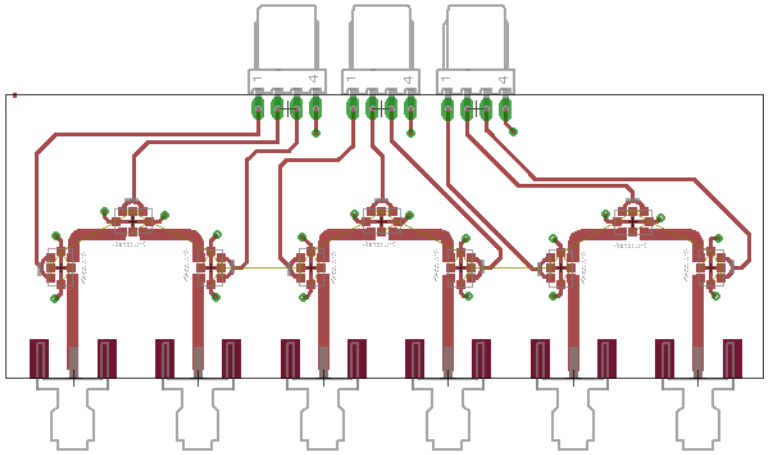

Figure 7.2: Layout of the phase-shifting section of the circuit

Final Board PCB layout

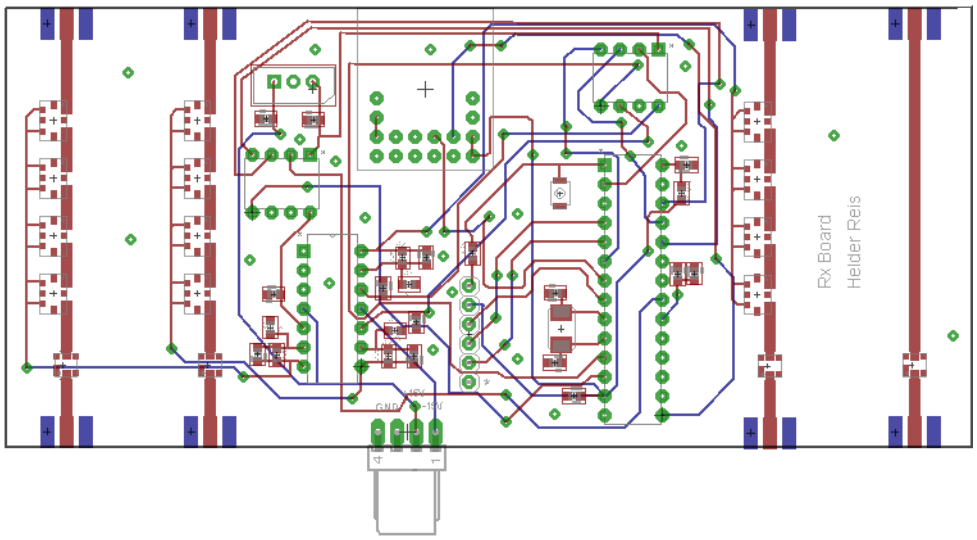

Figure 7.3: Receiver board PCB layout

Beamforming results

Least Mean-Squares

Measurement for $\theta_{SOI} = 0^{\mathbf{o}}$

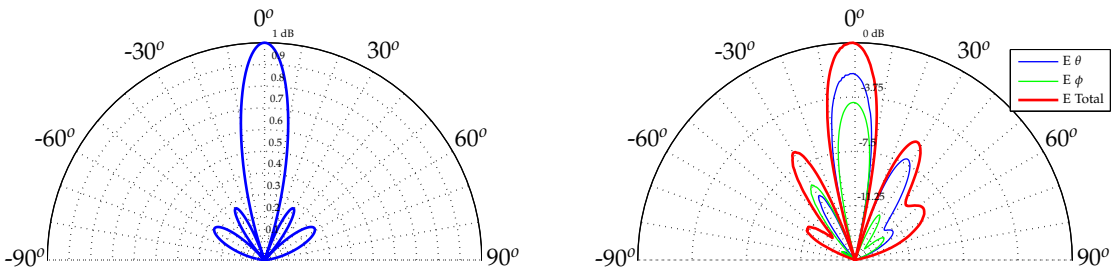

(a) (b)

Figure 7.4: Simulated (a) and measured (b) beam steering for $\theta = 0^{\mathrm{o}}$

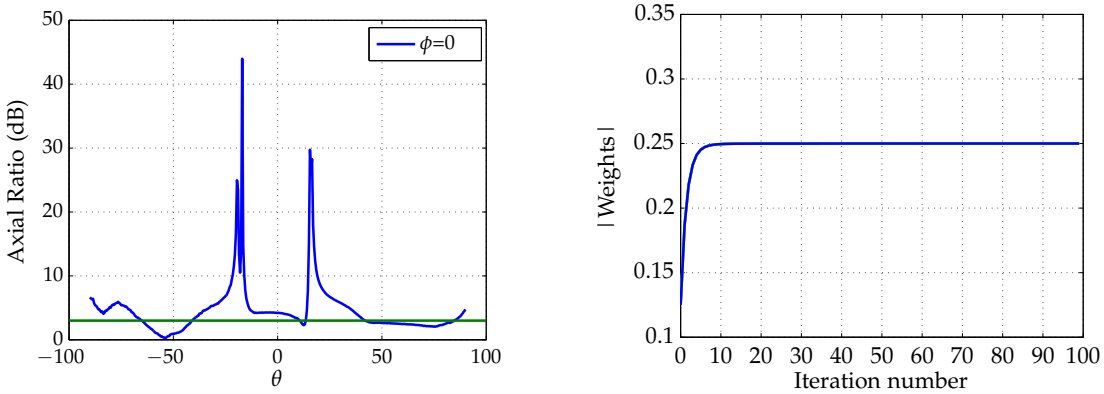

(a) (b)

Figure 7.5: Axial Ratio (a) and weights progression (b) for $\theta_{SOI} = 0^{\text{o}}$

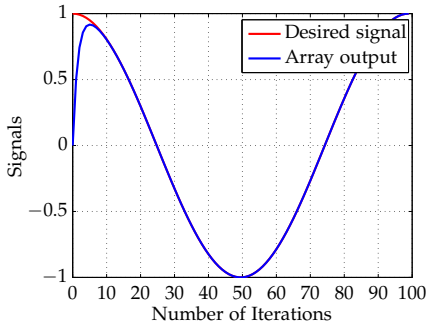

Figure 7.6: $\theta_{SOI} = 0^{\text{o}}$

Measurement for $\theta_{SOI} = 30^{\text{o}}$

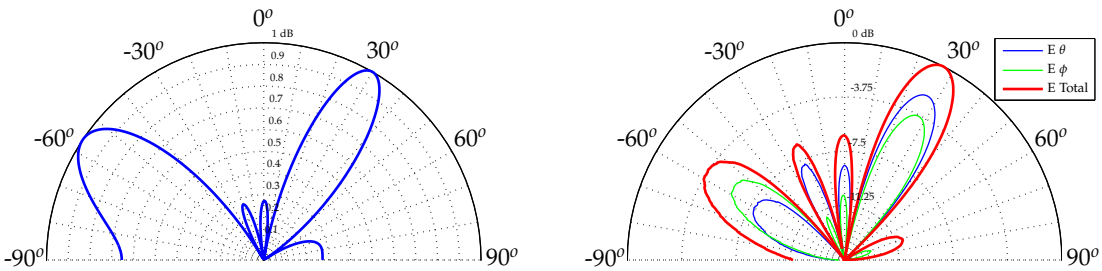

(a) (b)

Figure 7.7: Simulated (a) and measured (b) beam steering for $\theta = 30^{\text{o}}$

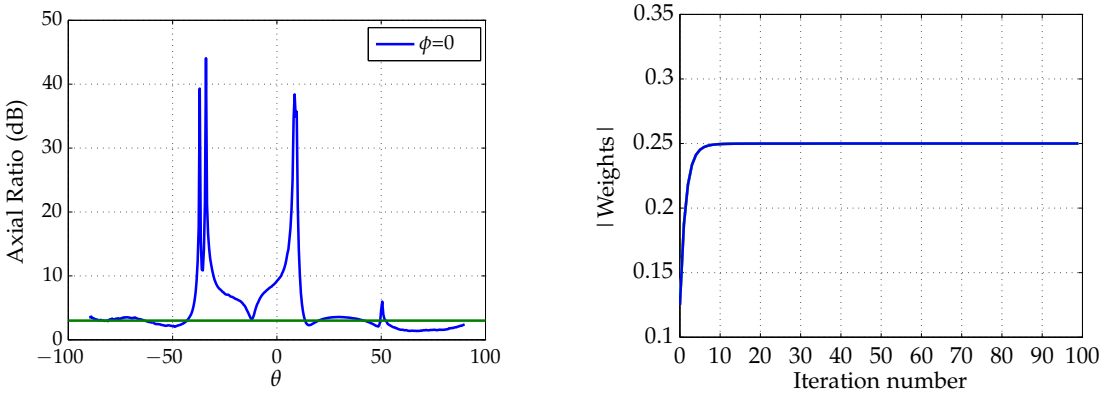

(a) (b)

Figure 7.8: Axial Ratio (a) and weights progression (b) for $\theta_{SOI} = 30^{\mathrm{o}}$

Measurement for $\theta_{SOI} = -30^{\mathrm{o}}$

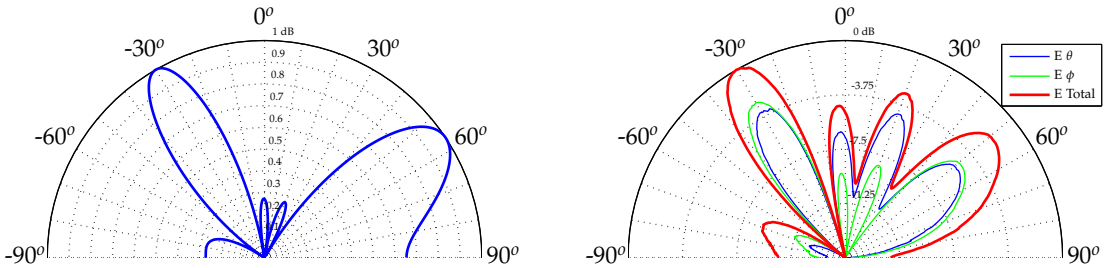

(a) (b)

Figure 7.9: Simulated (a) and measured (b) beam steering for $\theta = -30^{\mathrm{o}}$

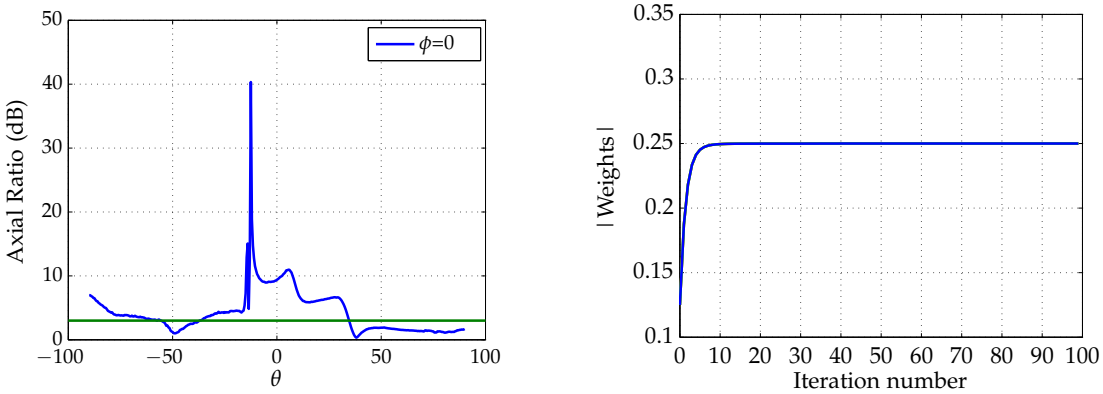

(a) (b)

Figure 7.10: Axial Ratio (a) and weights progression (b) for $\theta_{SOI} = -30^{\text{o}}$

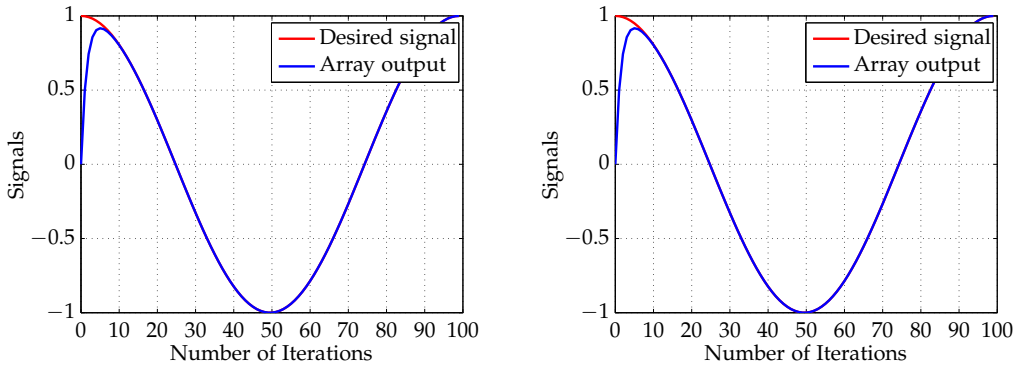

(a) (b)

Figure 7.11: $\theta_{SOI} = 30^{\text{o}}$ (a) and $\theta_{SOI} = -30^{\text{o}}$ (b)

Measurement for $\theta_{SOI} = 45^{\mathbf{o}}$ and $\theta_{SNOI} = -30^{\mathbf{o}}$

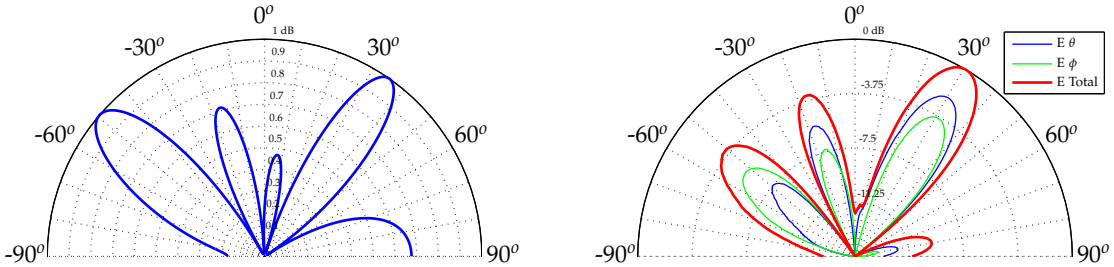

(a) (b)

Figure 7.12: Simulated (a) and measured (b) beam steering for $\theta_{SOI} = 45^{\mathrm{o}}$ and $\theta_{SNOI} = -30^{\mathrm{o}}$

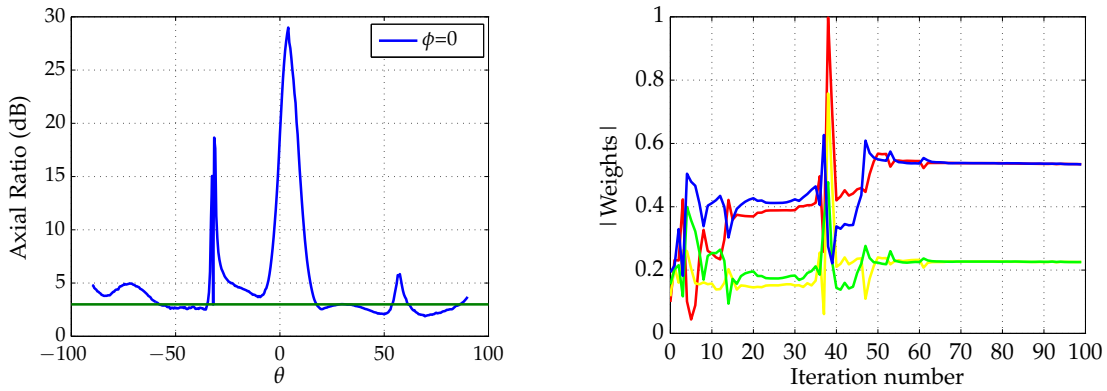

(a) (b)

Figure 7.13: Axial Ratio (a) and weights progression (b) for $\theta_{SOI} = 45^{\mathrm{o}}$ and $\theta_{SNOI} = -30^{\mathrm{o}}$

Measurement for $\theta = -45^{\mathbf{o}}$ and $\theta_{SNOI} = 30^{\mathbf{o}}$

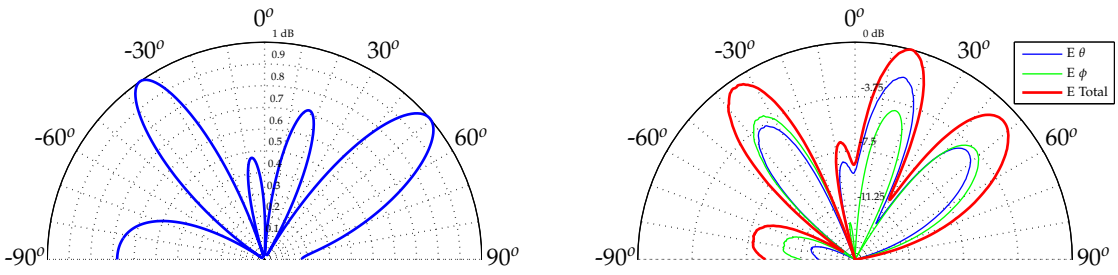

(a) (b)

Figure 7.14: Simulated (a) and measured beam steering for$\theta_{SOI} = -45^{\mathrm{o}}$ and $\theta_{SNOI} = 30^{\mathrm{o}}$

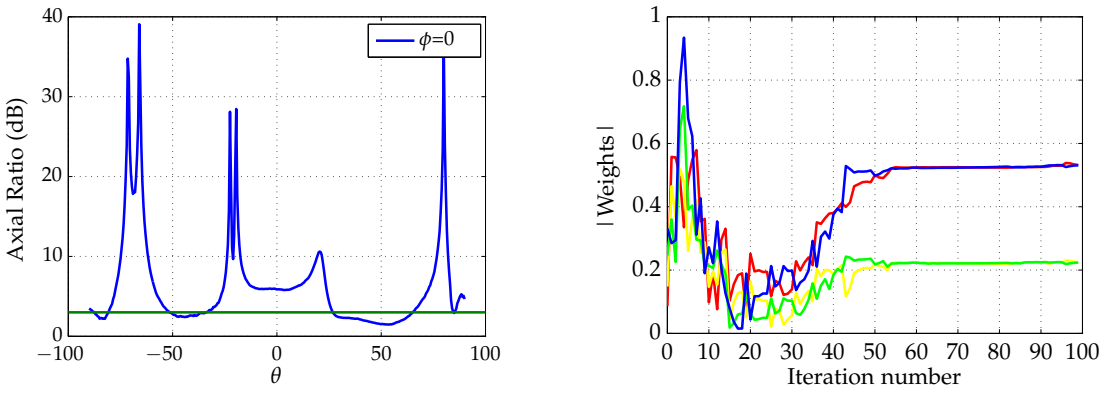

(a) (b)

Figure 7.15: Axial Ratio (a) and weights progression (b) for $\theta_{SOI} = 60^{\mathrm{o}}$ and $\theta_{SNOI} = 80^{\mathrm{o}}$

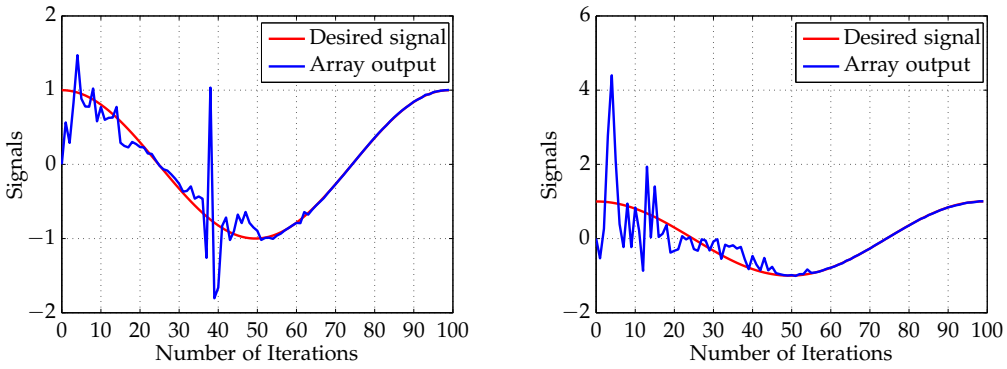

Figure 7.16: $\theta_{SOI} = 45^{\text{o}}/\theta_{SNOI} = -30^{\text{o}}$ (a) and $\theta_{SOI} = -45^{\text{o}}/\theta_{SNOI} = 30^{\text{o}}$ (b)

Measurement for $\theta_{SOI} = 60^{\text{o}}$ and $\theta_{SNOI} = 80^{\text{o}}$

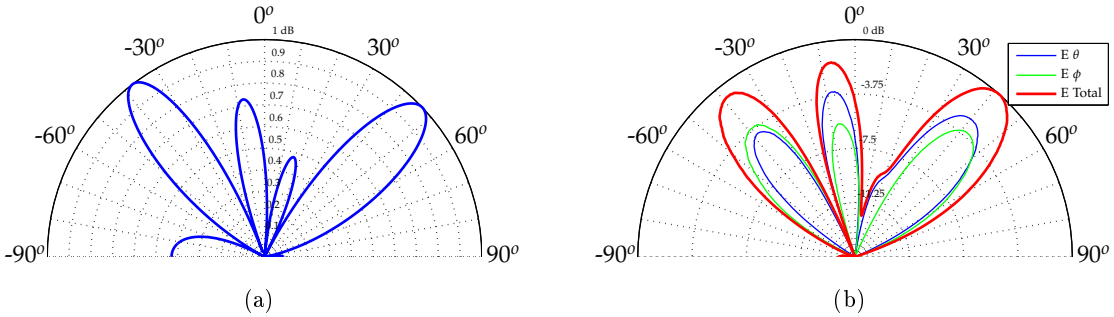

Figure 7.17: Simulated (a) and measured (b) beam steering for $\theta_{SOI} = 60^{\text{o}}$ and $\theta_{SNOI} = 80^{\text{o}}$

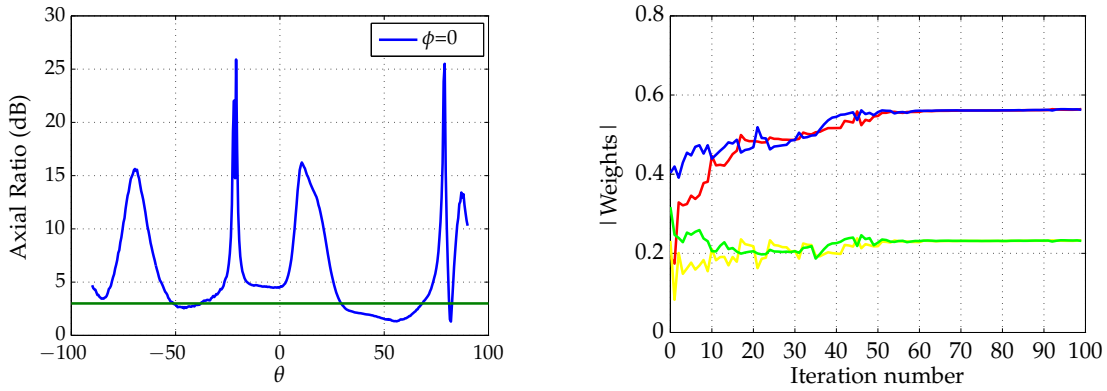

(a) (b)

Figure 7.18: Axial Ratio (a) and weights progression (b) for $\theta_{SOI} = 60^{\underline{o}}$ and $\theta_{SNOI} = 80^{\underline{o}}$

Measurement for $\theta_{SOI} = -60^{\underline{o}}$ and $\theta_{SNOI} = -80^{\underline{o}}$

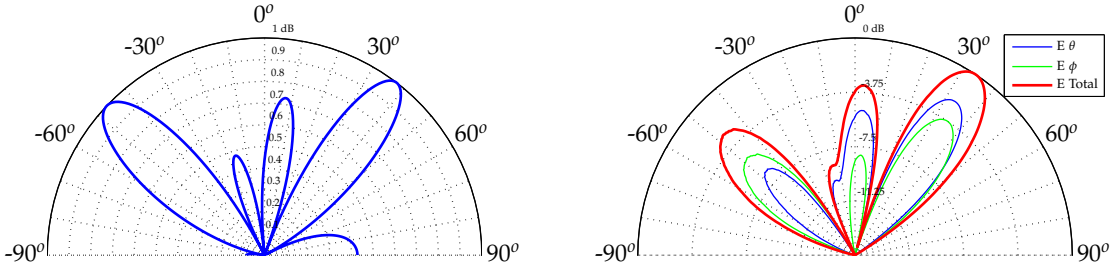

(a) (b)

Figure 7.19: Simulated (a) and measure (b) beam steering for $\theta_{SOI} = -60^{\underline{o}}$ and $\theta_{SNOI} = -80^{\underline{o}}$

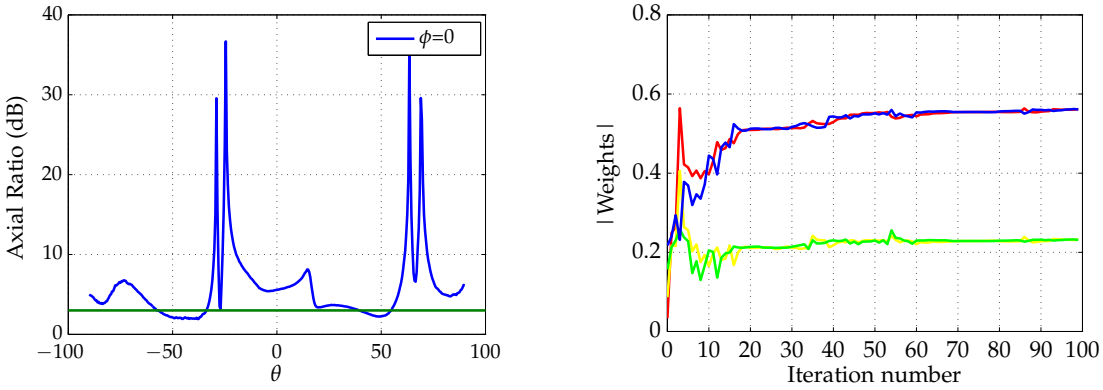

(a) (b)

Figure 7.20: Axial Ratio (a) and weights progression (b) for $\theta_{SOI} = -60^{o}$ and $\theta_{SNOI} = -80^{o}$

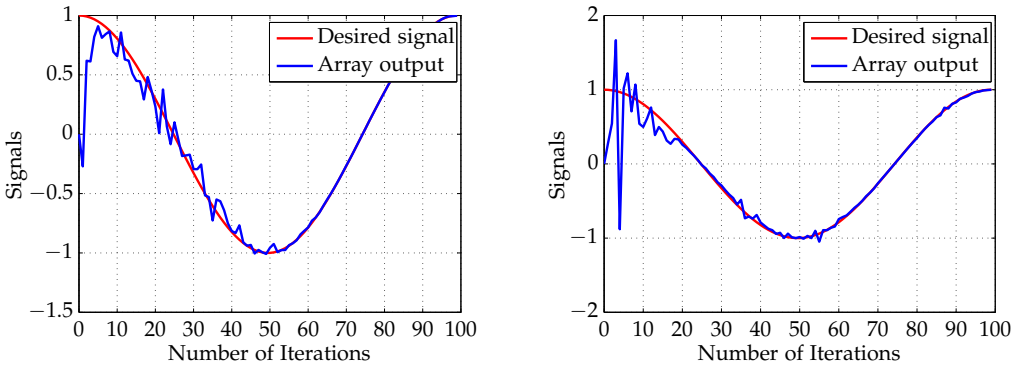

(a) (b)

Figure 7.21: $\theta_{SOI} = 60^{o}/\theta_{SNOI} = 80^{o}$ (a) and $\theta_{SOI} = -60^{o}/\theta_{SNOI} = -80^{o}$ (b)

Measurement for $\theta_{SOI} = 20^{\mathbf{o}}$ and $\theta_{SOI} = 60^{\mathbf{o}}$

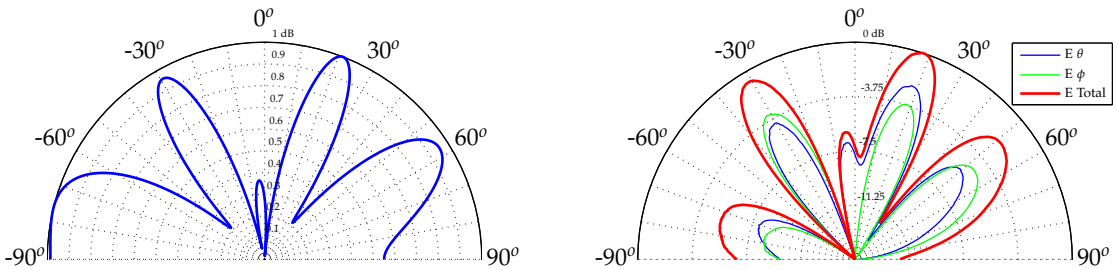

(a) (b)

Figure 7.22: Simulated (a) and measured (b) beam steering for $\theta_{SOI} = 20^{\mathrm{o}}$ and $\theta_{SNOI} = 60^{\mathrm{o}}$

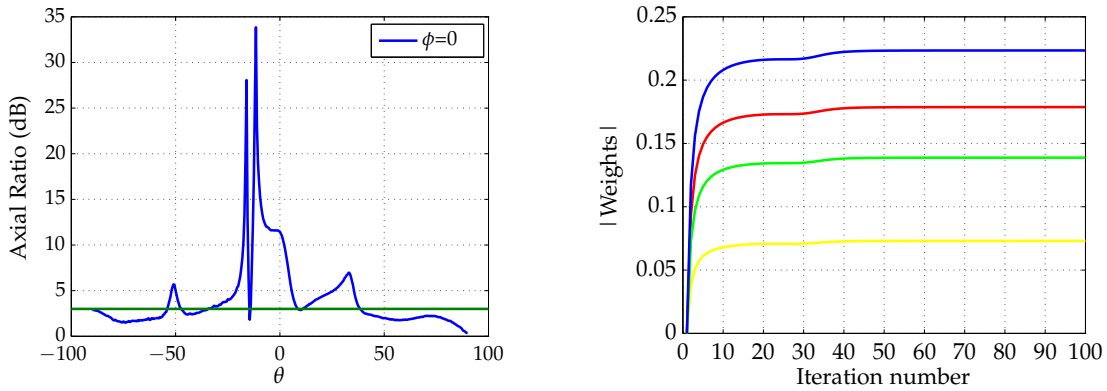

(a) (b)

Figure 7.23: Axial Ratio (a) and weights progression (b) for $\theta_{SOI} = 20^{\mathrm{o}}$ and $\theta_{SOI} = 60^{\mathrm{o}}$

Measurement for $\theta_{SOI} = 60^{\mathbf{o}}$ and $\theta_{SOI} = -60^{\mathbf{o}}$

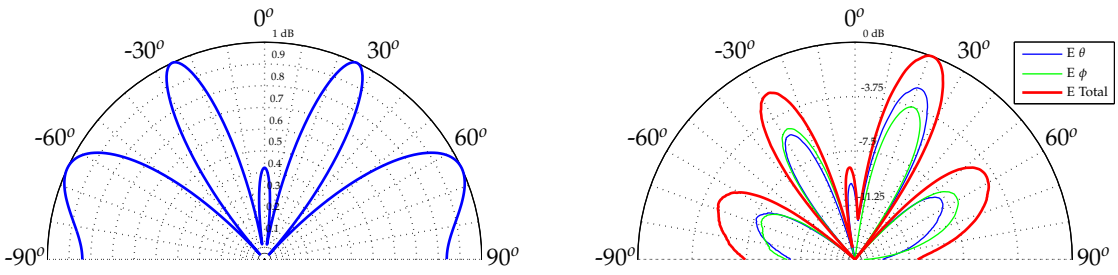

Figure 7.24: Simulated (a) and measured (b) beam steering for$\theta_{SOI} = 60^{\mathrm{o}}$ and $\theta_{SOI} = -60^{\mathrm{o}}$

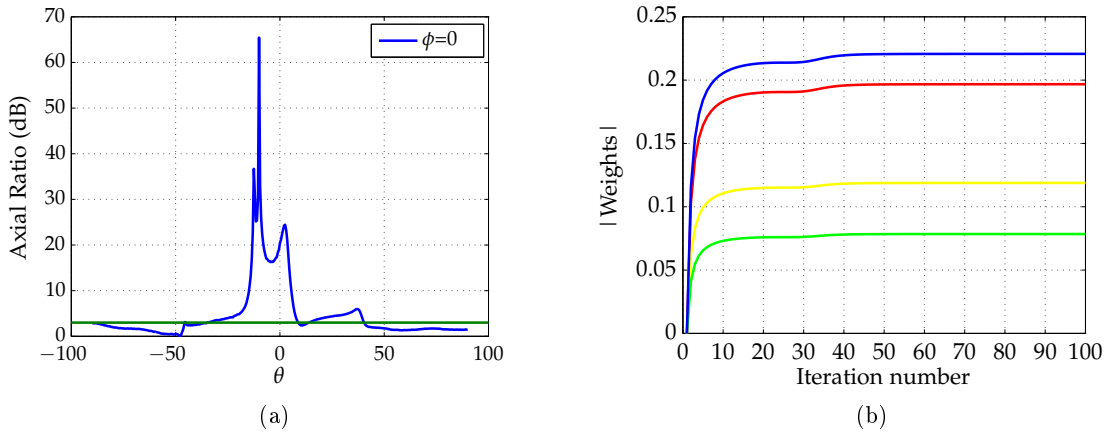

Figure 7.25: Axial Ratio (a) and weights progression (b) for $\theta_{SOI} = 60^{\mathrm{o}}$ and $\theta_{SOI} = -60^{\mathrm{o}}$

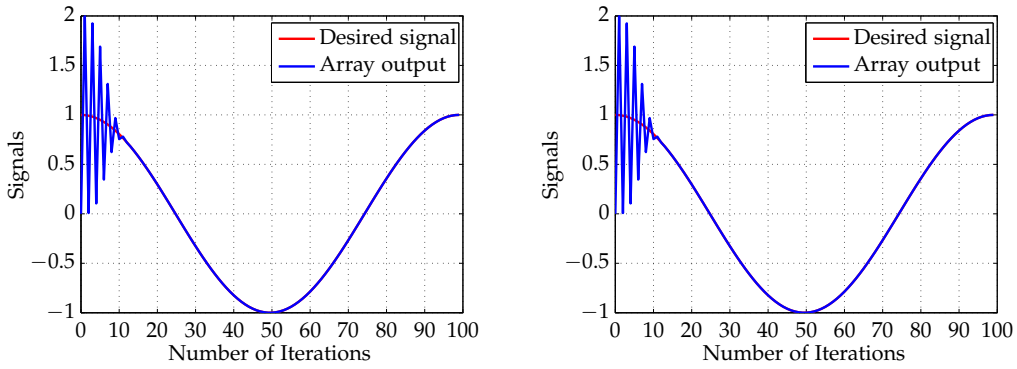

(a) (b)

Figure 7.26: $\theta_{SOI} = 20^{\text{o}}/\theta_{SOI} = 60^{\text{o}}$ (a) and $\theta_{SOI} = 60^{\text{o}}/\theta_{SOI} = -60^{\text{o}}$ (b)

Measurement for $\theta_{SOI} = 0^{\text{o}}$ and $\theta_{SOI} = 45^{\text{o}}$

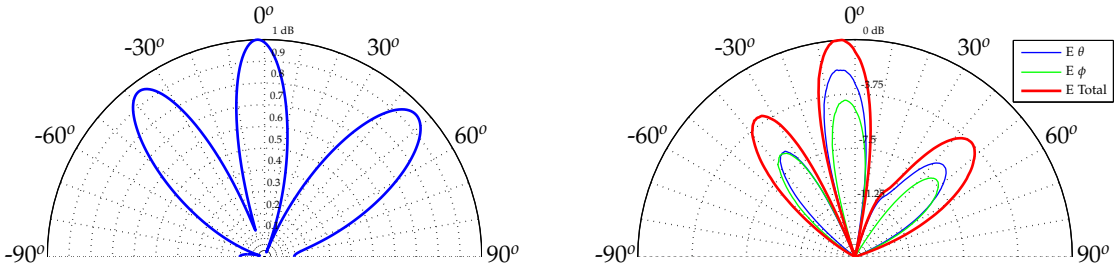

(a) (b)

Figure 7.27: Simulated (a) and measured (b) beam steering for $\theta_{SOI} = 0^{\text{o}}$ and $\theta_{SOI} = 45^{\text{o}}$

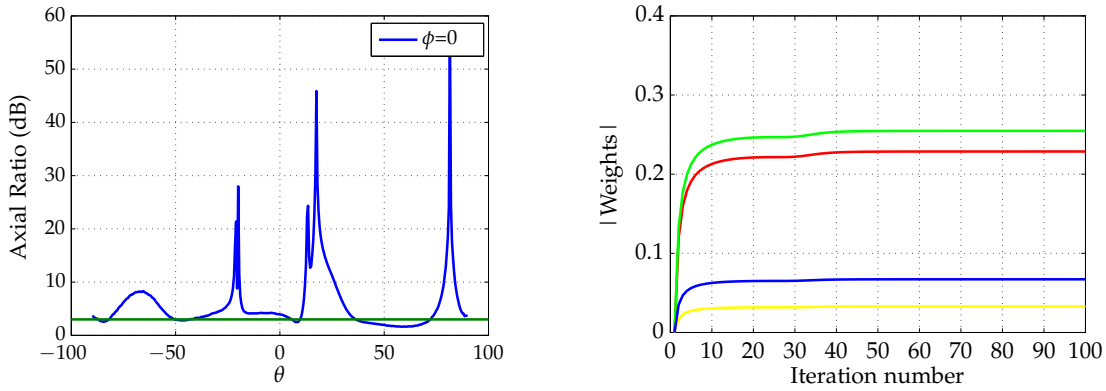

(a) (b)

Figure 7.28: Axial Ratio (a) and weights progression (b) for $\theta_{SOI} = 0^{\text{o}}$ and $\theta_{SOI} = 45^{\text{o}}$

Measurement for $\theta_{SOI} = -20^{\text{o}}$ and $\theta_{SOI} = -80^{\text{o}}$

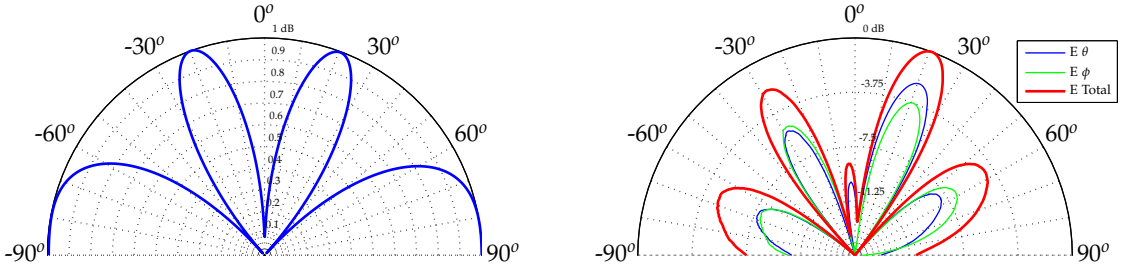

(a) (b)

Figure 7.29: Simulated (a) and measured (b) beam steering for $\theta_{SOI} = 20^{\text{o}}$ and $\theta_{SOI} = -80^{\text{o}}$

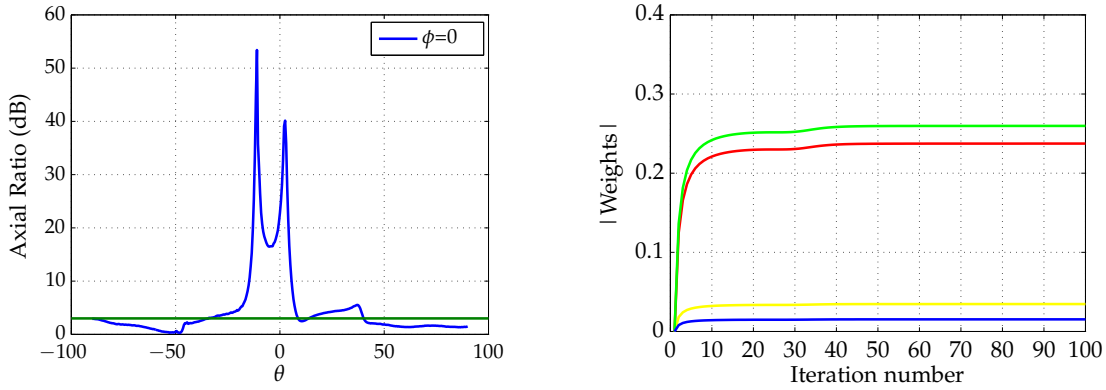

(a) (b)

Figure 7.30: Axial Ratio (a) and weights progression (b) for $\theta_{SOI} = 20^{o}$ and $\theta_{SOI} = -80^{o}$

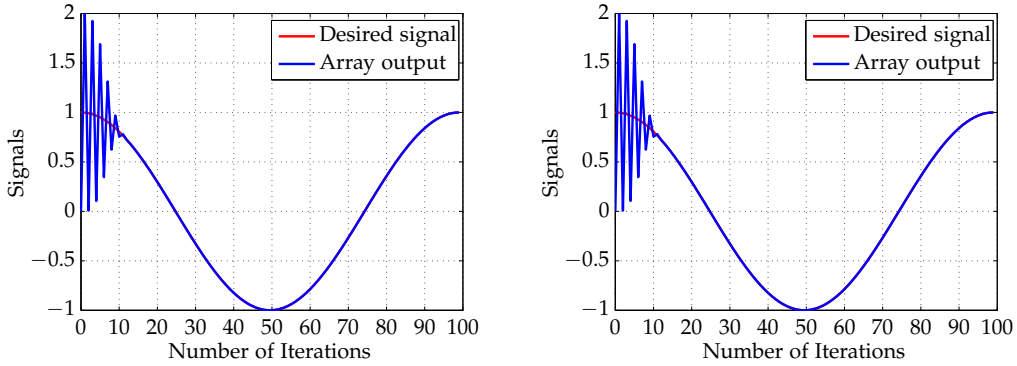

(a) (b)

Figure 7.31: $\theta_{SOI} = 0^{o}/\theta_{SOI} = 45^{o}$ (a) and $\theta_{SOI} = -20^{o}/\theta_{SOI} = -80^{o}$ (b)

Recursive Least-Squares

Measurement for $\theta_{SOI} = 0^{\underline{o}}$

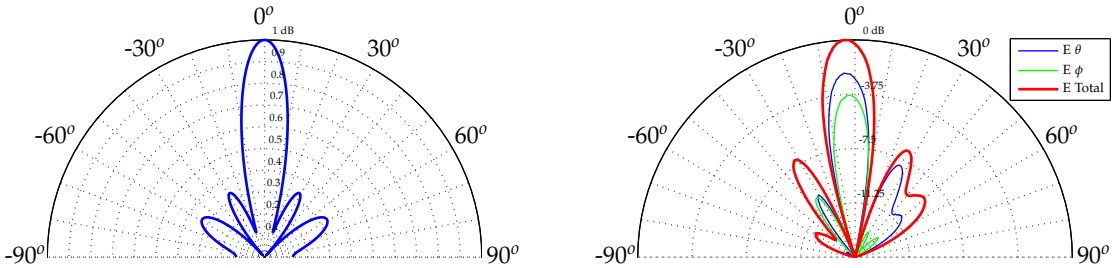

(a) (b)

Figure 7.32: Simulated (a) and measured (b) beam steering for $\theta = 0^{\underline{o}}$

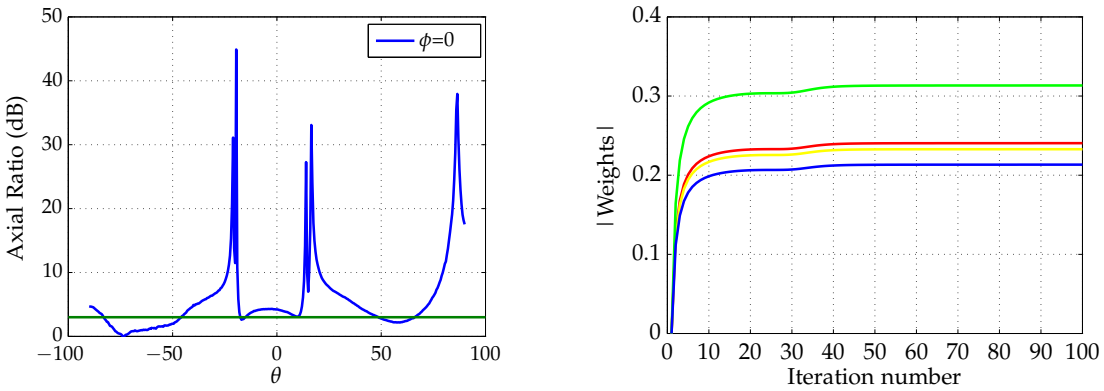

(a) (b)

Figure 7.33: Axial Ratio (a) and weights progression (b) for $\theta = 0^{\underline{o}}$

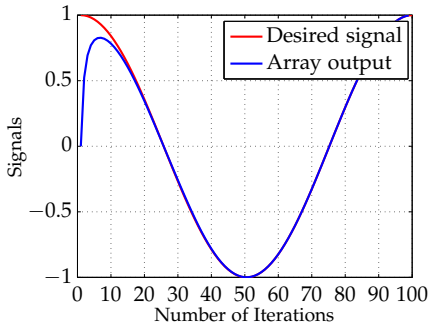

Figure 7.34: $\theta_{SOI} = 0^{\underline{o}}$

Measurement for $\theta_{SOI} = 30^{\mathrm{o}}$

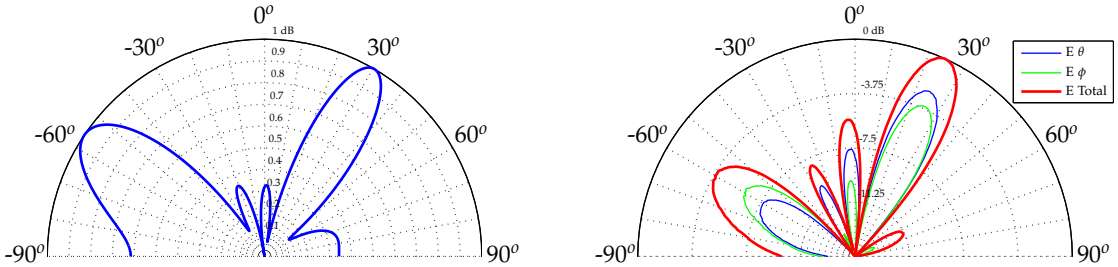

(a) (b)

Figure 7.35: Simulated (a) and measured (b) beam steering for $\theta = 30^{\mathrm{o}}$

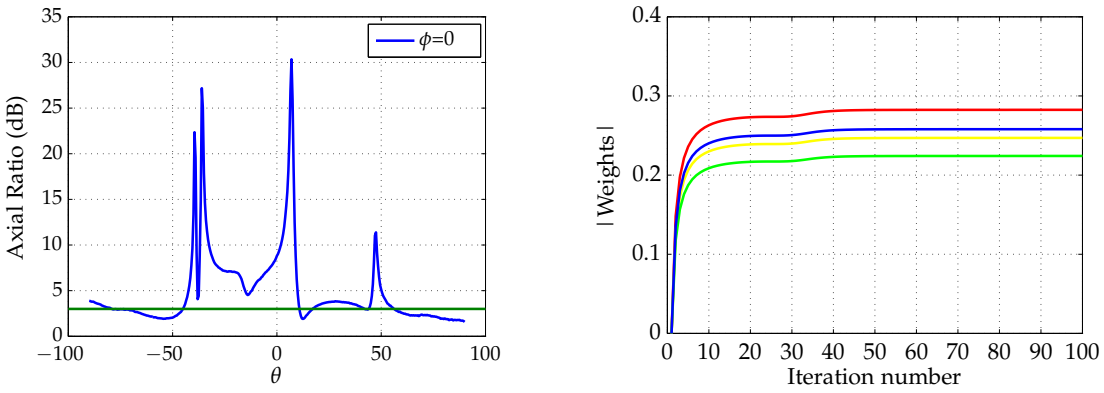

(a) (b)

Figure 7.36: Axial Ratio (a) and weights progression (b) for $\theta = 30^{\mathrm{o}}$

Measurement for $\theta_{SOI} = -30^{o}$

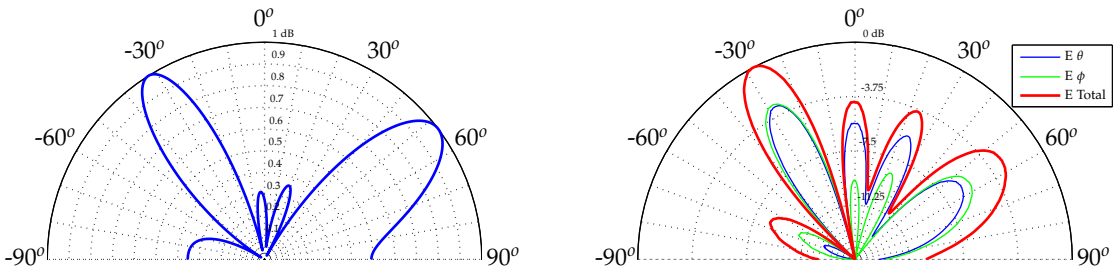

(a) (b)

Figure 7.37: Simulated beam steering for $\theta = -30^{o}$

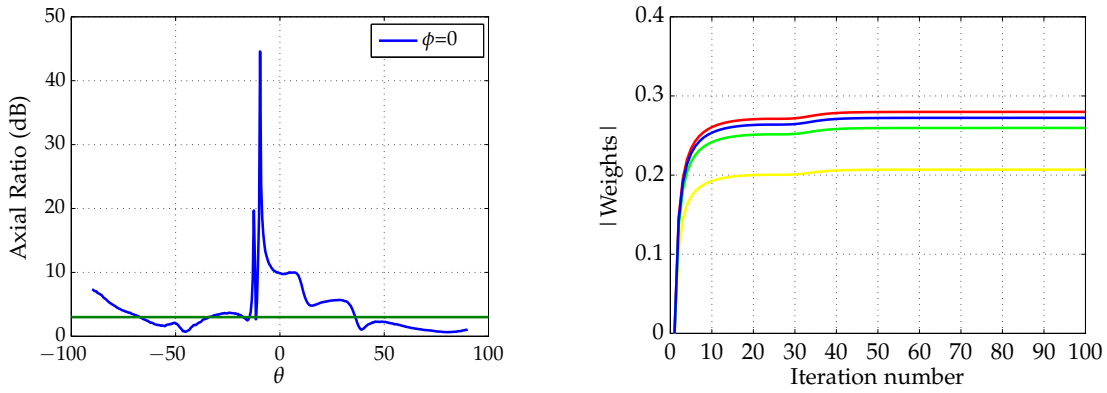

(a) (b)

Figure 7.38: Axial Ratio (a) and weights progression (b) for $\theta = -30^{o}$

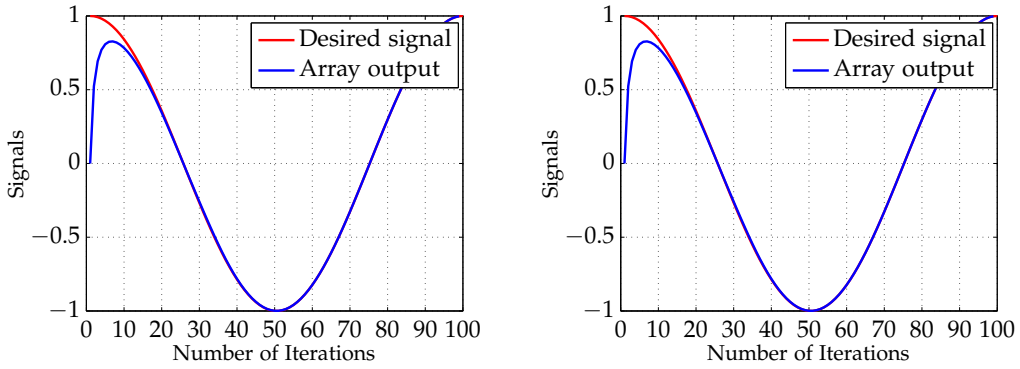

(a) (b)

Figure 7.39: $\theta_{SOI} = 30^{\text{o}}$ (a) and $\theta_{SOI} = -30^{\text{o}}$ (b)

Measurement for $\theta_{SOI} = 45^{\text{o}}$ and $\theta_{SNOI} = -30^{\text{o}}$

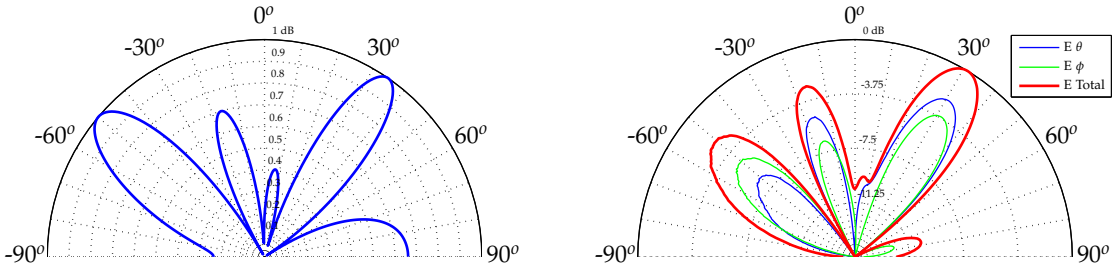

(a) (b)

Figure 7.40: Simulated (a) and measured (b) beam steering for $\theta_{SOI} = 45^{\text{o}}$ and $\theta_{SNOI} = -30^{\text{o}}$

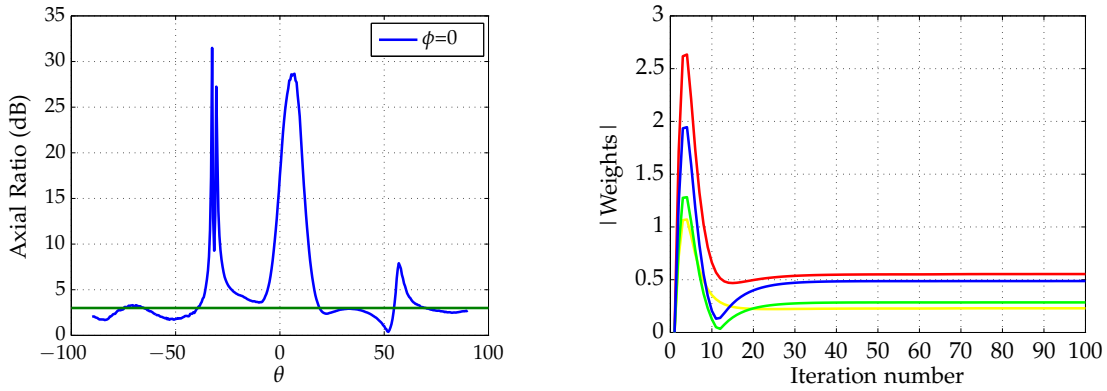

(a) (b)

Figure 7.41: Axial Ratio (a) and weights progression (b) for $\theta_{SOI} = 45^{o}$ and $\theta_{SNOI} = -30^{o}$

Measurement for $\theta_{SOI} = -45^{o}$ and $\theta_{SNOI} = 30^{o}$

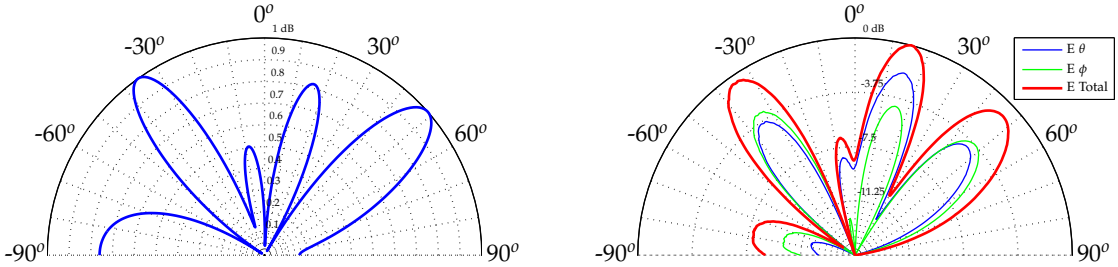

(a) (b)

Figure 7.42: Simulated (a) and measured (b) beam steering for$\theta_{SOI} = -45^{o}$ and $\theta_{SNOI} = 30^{o}$

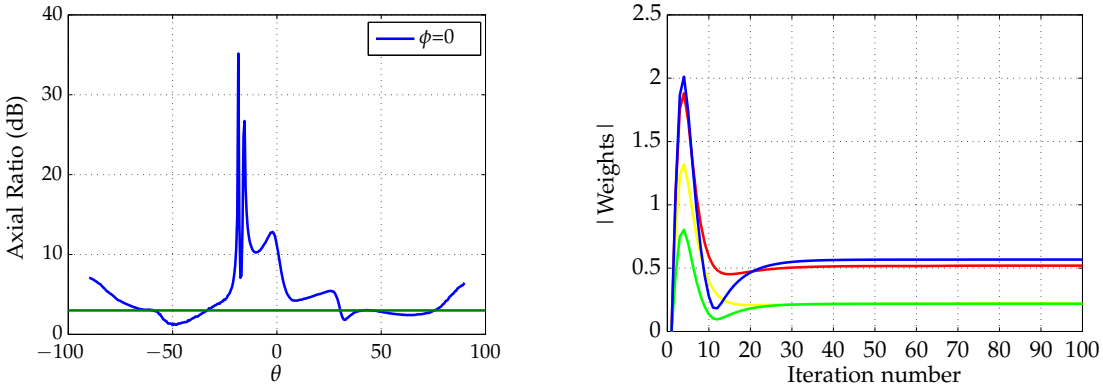

(a) (b)

Figure 7.43: Axial Ratio (a) and weights progression (b) for $\theta_{SOI} = -45^{o}$ and $\theta_{SNOI} = 30^{o}$

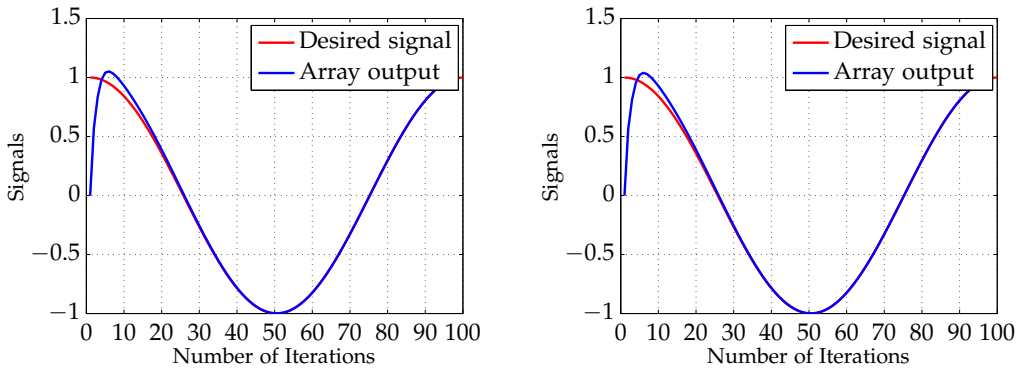

(a) (b)

Figure 7.44: $\theta_{SOI} = 45^{o}/\theta_{SNOI} = -30^{o}$ (a) and $\theta_{SOI} = -45^{o}/\theta_{SNOI} = 30^{o}$ (b)

Measurement for $\theta_{SOI} = 60^{\underline{o}}$ and $\theta_{SNOI} = 80^{\underline{o}}$

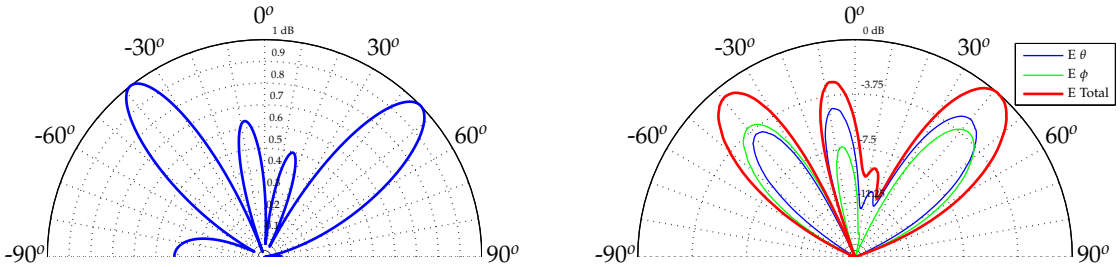

Figure 7.45: Simulated (a) and measured beam steering for $\theta_{SOI} = 60^{\underline{o}}$ and $\theta_{SNOI} = 80^{\underline{o}}$

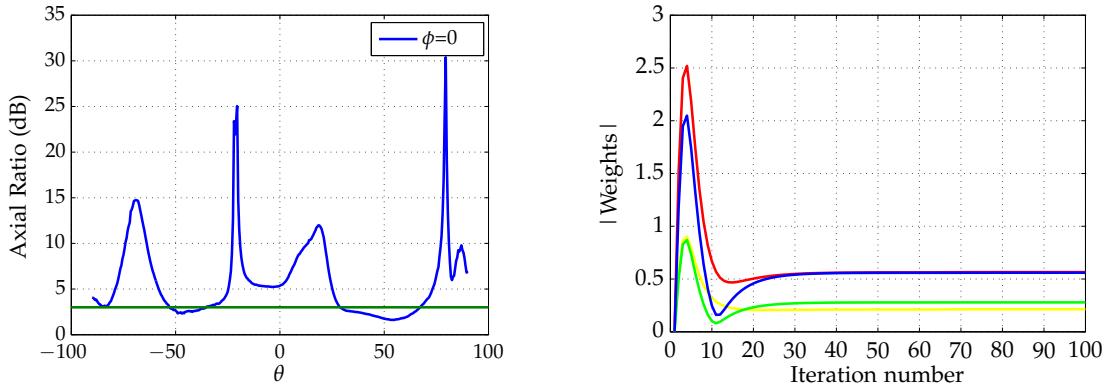

Figure 7.46: Axial Ratio (a) and weights progression (b) for $\theta_{SOI} = 60^{\underline{o}}$ and $\theta_{SNOI} = 80^{\underline{o}}$

Measurement for $\theta_{SOI} = -60^{\mathbf{o}}$ and $\theta_{SNOI} = -80^{\mathbf{o}}$

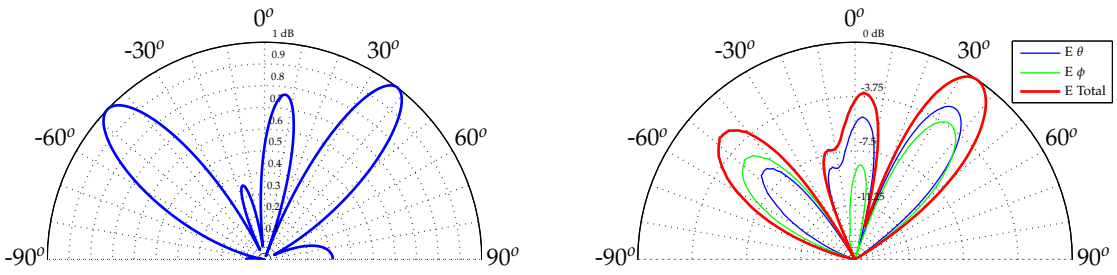

Figure 7.47: Simulated (a) and measured (b) beam steering for $\theta_{SOI} = -60^{\mathrm{o}}$ and $\theta_{SNOI} = -80^{\mathrm{o}}$

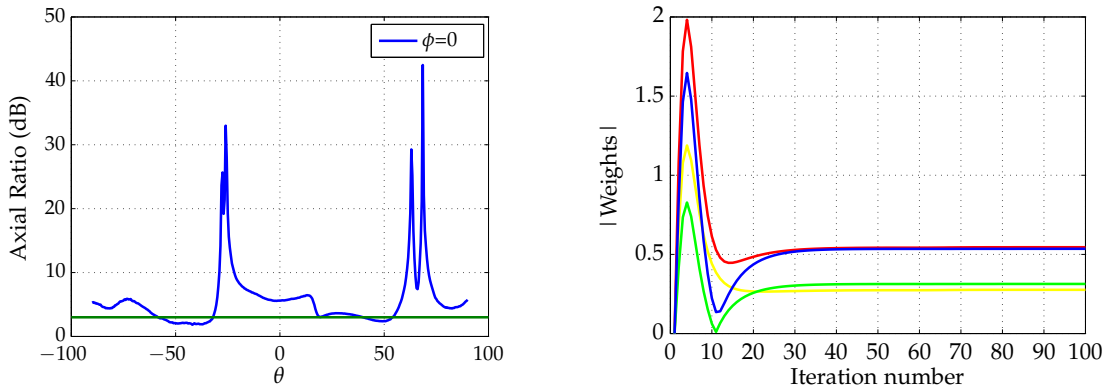

Figure 7.48: Axial Ratio (a) and weights progression (b) for $\theta_{SOI} = -60^{\mathrm{o}}$ and $\theta_{SNOI} = -80^{\mathrm{o}}$

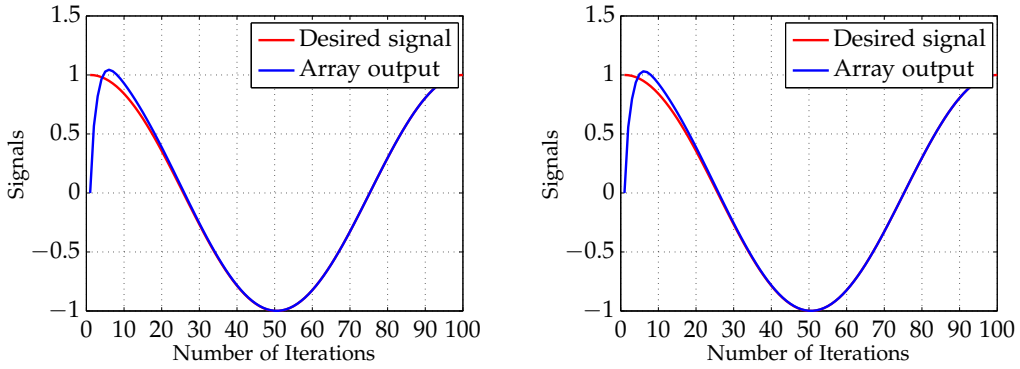

Figure 7.49: $\theta_{SOI} = 60^{\text{o}}/\theta_{SNOI} = 80^{\text{o}}$ (a) and $\theta_{SOI} = -60^{\text{o}}/\theta_{SNOI} = -80^{\text{o}}$ (b)

Measurement for $\theta_{SOI} = 20^{\text{o}}$ and $\theta_{SOI} = 60^{\text{o}}$

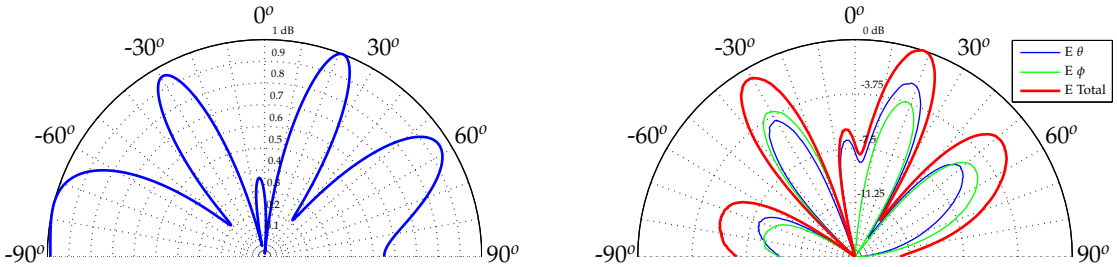

Figure 7.50: Simulated (a) and measured (b) beam steering for $\theta_{SOI} = 20^{\text{o}}$ and $\theta_{SNOI} = 60^{\text{o}}$

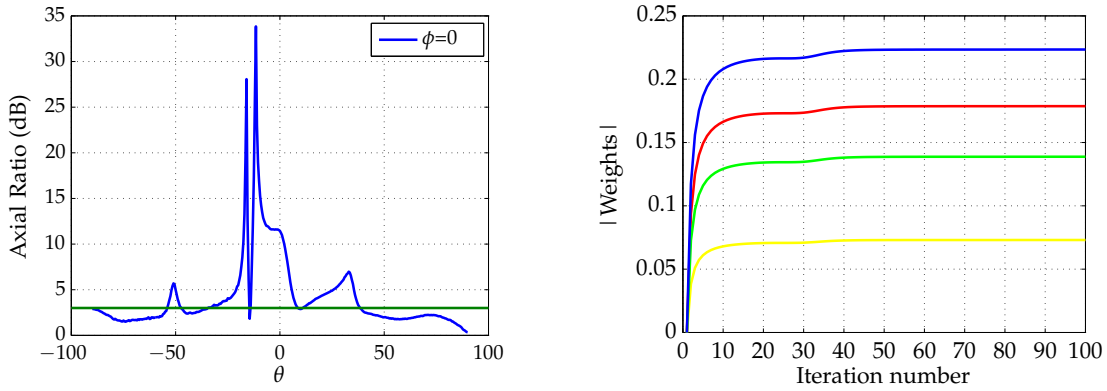

(a) (b)

Figure 7.51: Axial Ratio (a) and weights progression (b) for $\theta_{SOI} = 20^{o}$ and $\theta_{SOI} = 60^{o}$

Measurement for $\theta_{SOI} = 60^{o}$ and $\theta_{SOI} = -60^{o}$

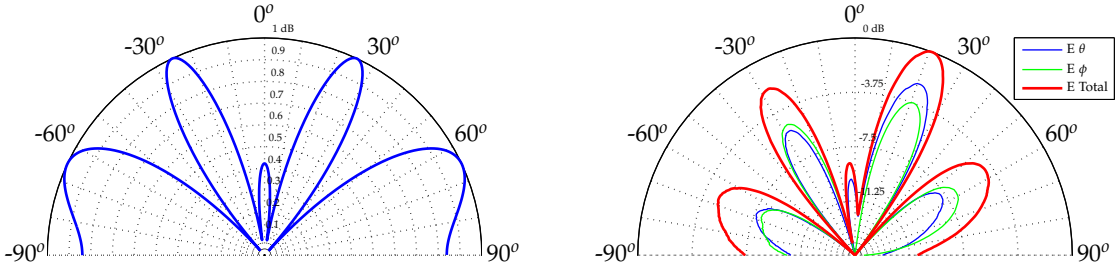

(a) (b)

Figure 7.52: Simulated (a) and measured (b) beam steering for$\theta_{SOI} = 60^{o}$ and $\theta_{SOI} = -60^{o}$

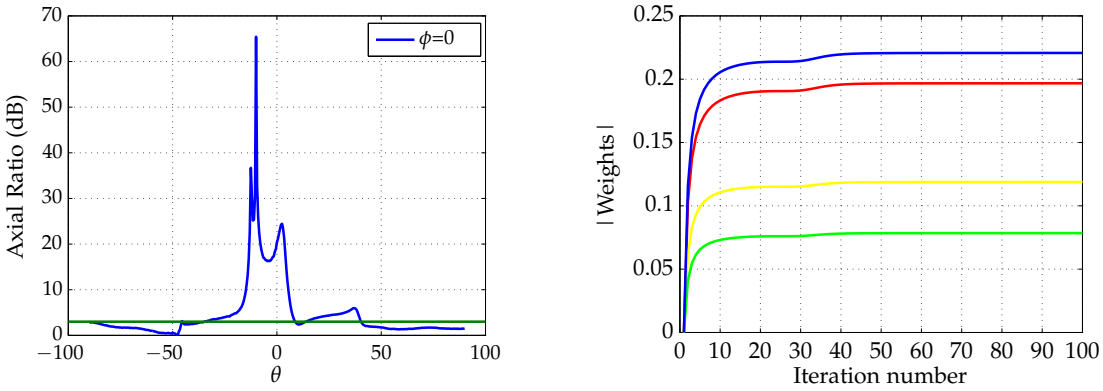

(a) (b)

Figure 7.53: Axial Ratio (a) and weights progression (b) for $\theta_{SOI} = 60^{o}$ and $\theta_{SOI} = -60^{o}$

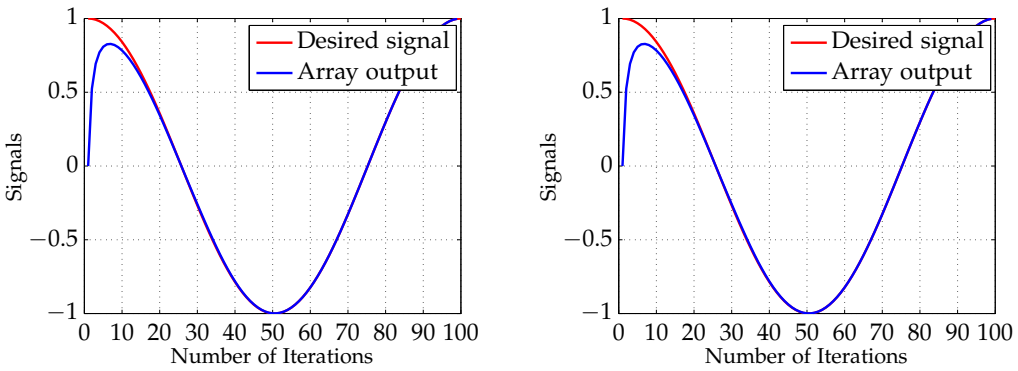

(a) (b)

Figure 7.54: $\theta_{SOI} = 20^{o}/\theta_{SOI} = 60^{o}$ (a) and $\theta_{SOI} = 60^{o}/\theta_{SOI} = -60^{o}$ (b)

Measurement for $\theta_{SOI} = 0^{\mathbf{o}}$ and $\theta_{SOI} = 45^{\mathbf{o}}$

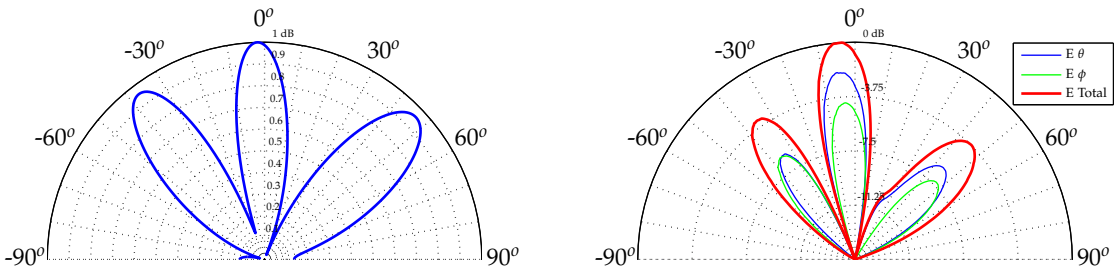

(a) (b)

Figure 7.55: Simulated (a) and measured (b) beam steering for $\theta_{SOI} = 0^{\mathrm{o}}$ and $\theta_{SOI} = 45^{\mathrm{o}}$

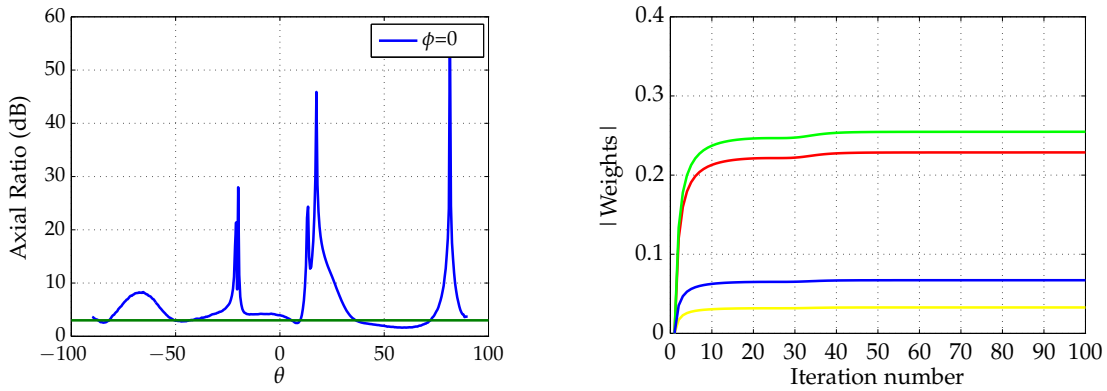

(a) (b)

Figure 7.56: Axial Ratio (a) and weights progression (b) for $\theta_{SOI} = 0^{\mathrm{o}}$ and $\theta_{SOI} = 45^{\mathrm{o}}$

Measurement for $\theta_{SOI} = -20^{\mathbf{o}}$ and $\theta_{SOI} = -80^{\mathbf{o}}$

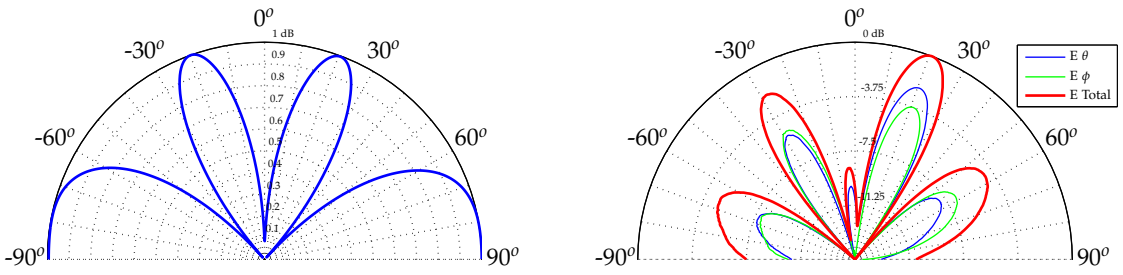

(a) (b)

Figure 7.57: Simulated (a) and measured (b) beam steering for $\theta_{SOI} = 20^{\mathrm{o}}$ and $\theta_{SOI} = -80^{\mathrm{o}}$

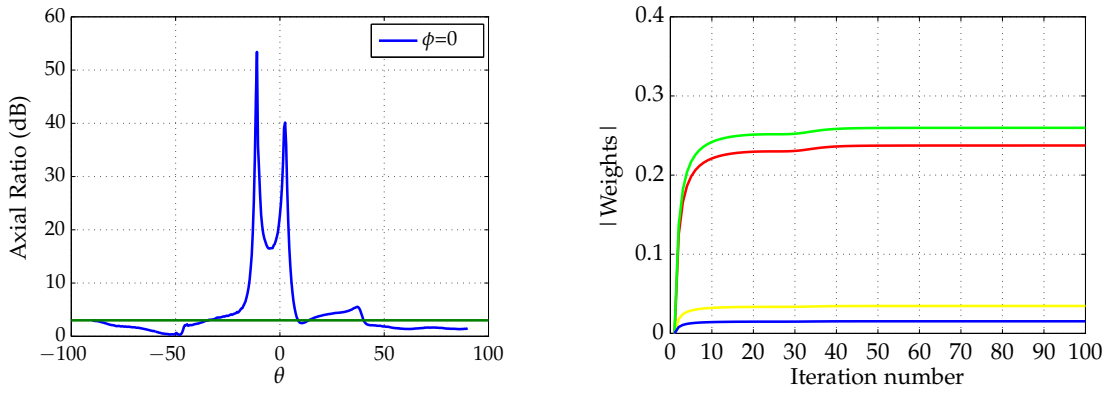

(a) (b)

Figure 7.58: Axial Ratio (a) and weights progression (b) for $\theta_{SOI} = 20^{\mathrm{o}}$ and $\theta_{SOI} = -80^{\mathrm{o}}$

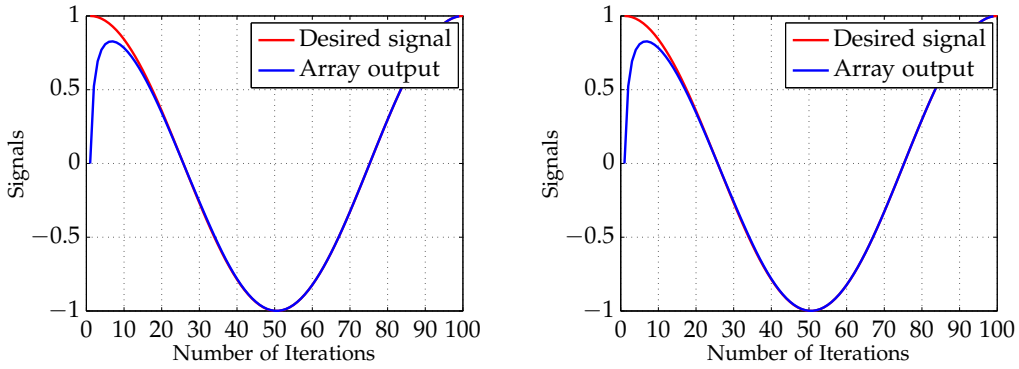

(a) (b)

Figure 7.59: $\theta_{SOI} = 0^{\text{o}}/\theta_{SOI} = 45^{\text{o}}$ (a) and $\theta_{SOI} = -20^{\text{o}}/\theta_{SOI} = -80^{\text{o}}$ (b)

Constant Modulus

Measurement for $\theta_{SOI} = 0^{\text{o}}$

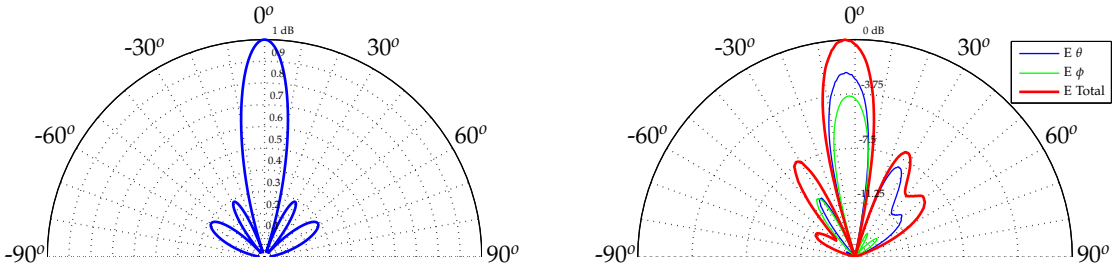

(a) (b)

Figure 7.60: Simulated (a) and measured (b) beam steering for $\theta = 0^{\text{o}}$

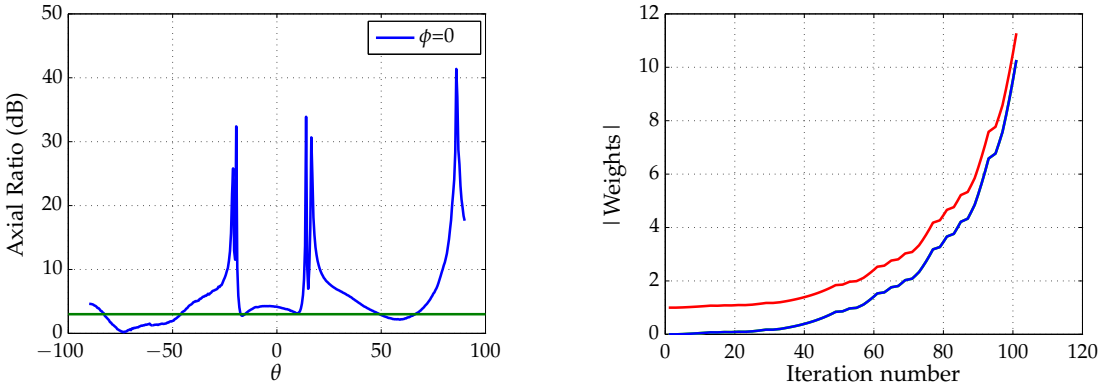

(a) (b)

Figure 7.61: Axial Ratio (a) and weights progression (b) for $\theta_{SOI} = 0^{\text{o}}$

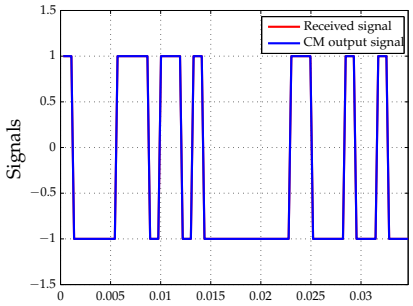

Figure 7.62: $\theta_{SOI} = 0^{\text{o}}$

Measurement for $\theta_{SOI} = 30^{\text{o}}$

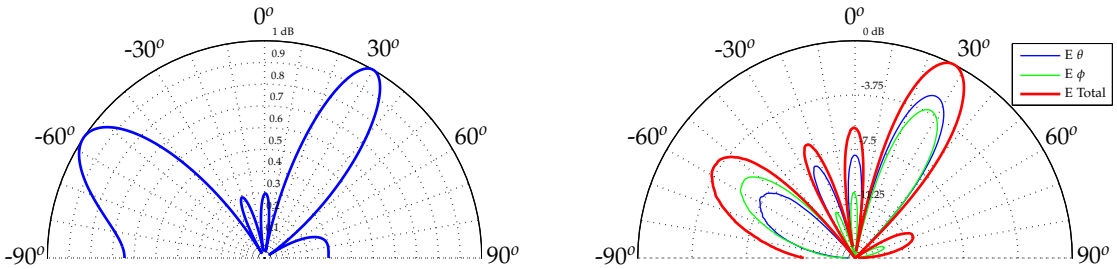

(a) (b)

Figure 7.63: Simulated (a) and measured (b) beam steering for $\theta = 30^{\text{o}}$

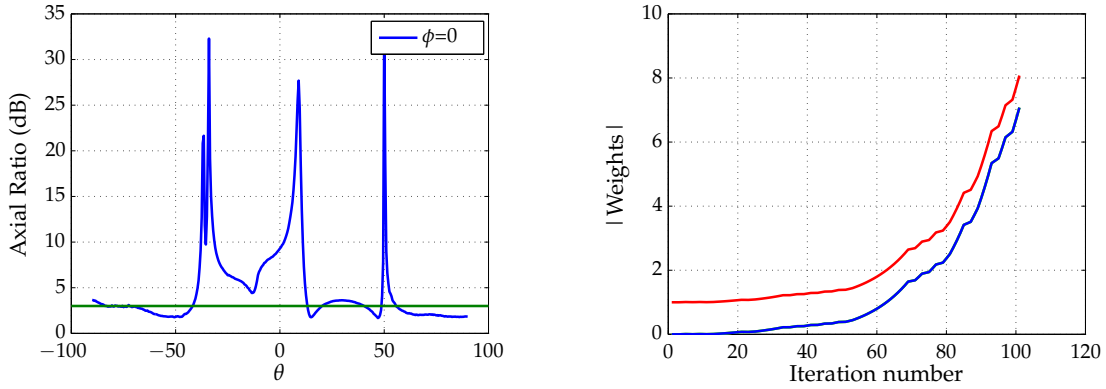

(a) (b)

Figure 7.64: Axial Ratio (a) and weights progression (b) for $\theta_{SOI} = 30^{o}$

Measurement for $\theta_{SOI} = -30^{o}$

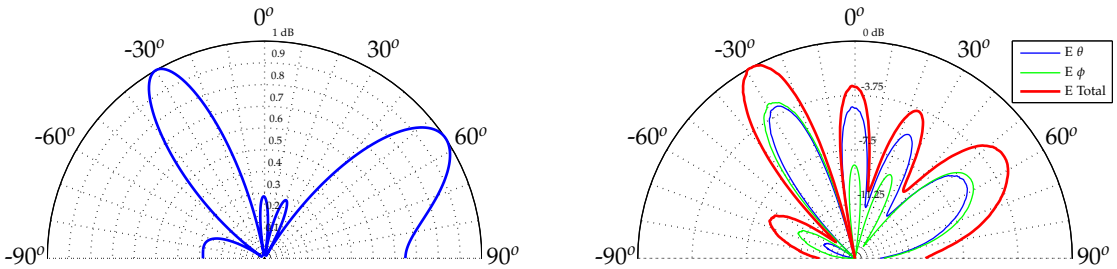

(a) (b)

Figure 7.65: Simulated (a) and measured (b) beam steering for $\theta = -30^{o}$

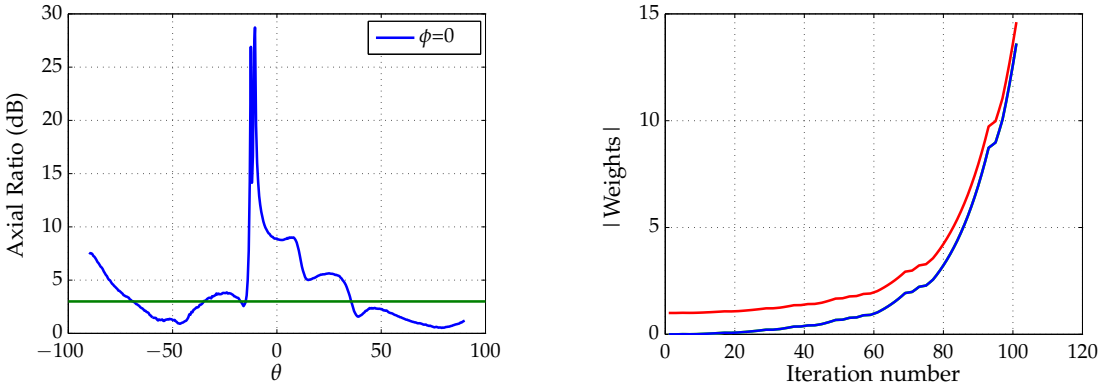

(a) (b)

Figure 7.66: Axial Ratio (a) and weights progression (b) for $\theta_{SOI} = -30^{\text{o}}$

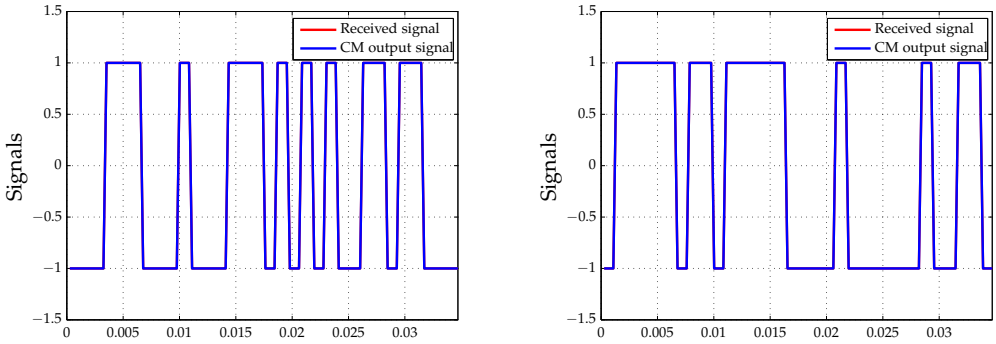

(a) (b)

Figure 7.67: $\theta_{SOI} = 30^{\text{o}}$ (a) and $\theta_{SOI} = -30^{\text{o}}$ (b)

Measurement for $\theta_{SOI} = 60^{\underline{o}}$ with multipath components at $\theta = 45^{\underline{o}}$ and $\theta = 80^{\underline{o}}$

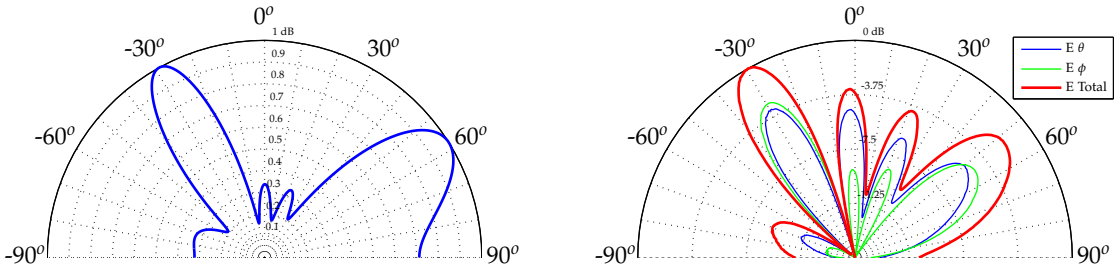

(a) (b)

Figure 7.68: Simulated (a) and measured (b) beam steering for $\theta_{SOI} = 60^{\underline{o}}$ and multipath at $\theta = 45^{\underline{o}}$ and $\theta = 80^{\underline{o}}$

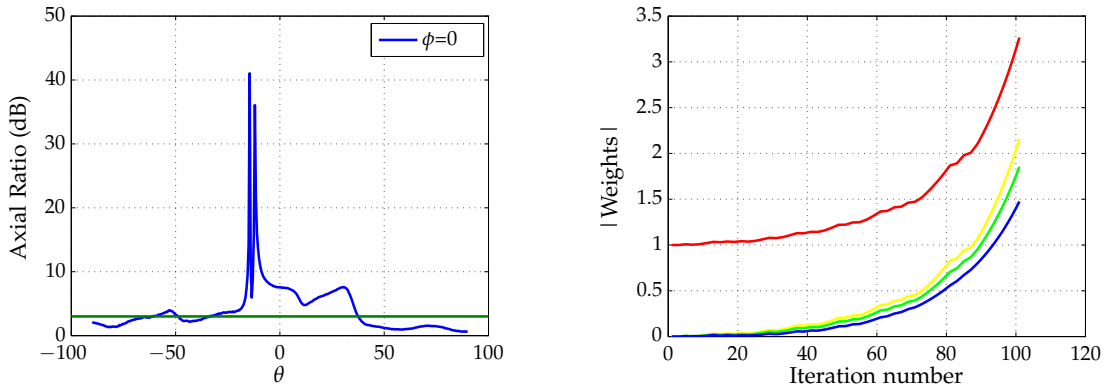

(a) (b)

Figure 7.69: Axial Ratio (a) and weights progression (b) for $\theta_{SOI} = 60^{\underline{o}}$ and multipath at $\theta = 45^{\underline{o}}$ and $\theta = 80^{\underline{o}}$

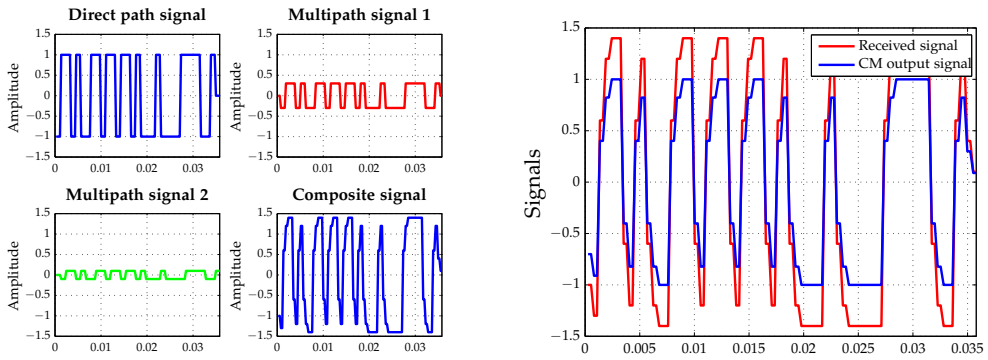

(a) (b)

Figure 7.70: Received composite signal (a) and array output (b) for $\theta_{SOI} = 60^{\text{o}}$ and multipath at $\theta = 45^{\text{o}}$ and $\theta = 80^{\text{o}}$

Measurement for $\theta_{SOI} = -45^{\text{o}}$ with multipath components at $\theta = -30^{\text{o}}$ and $\theta = -60^{\text{o}}$

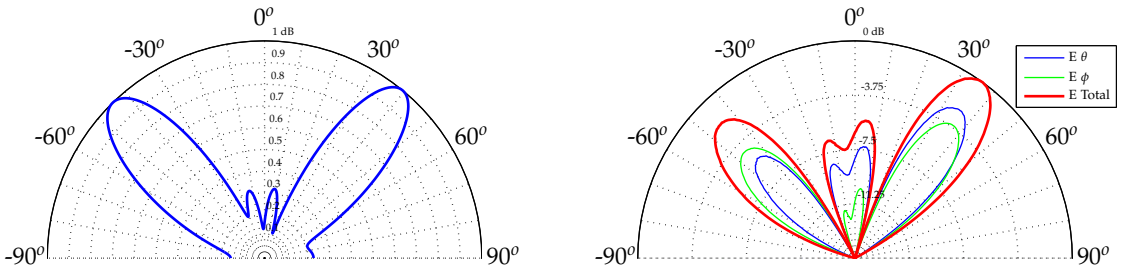

(a) (b)

Figure 7.71: Simulated (a) and measured (b) beam steering for $\theta_{SOI} = -45^{\text{o}}$ and multipath at $\theta = -30^{\text{o}}$ and $\theta = -60^{\text{o}}$

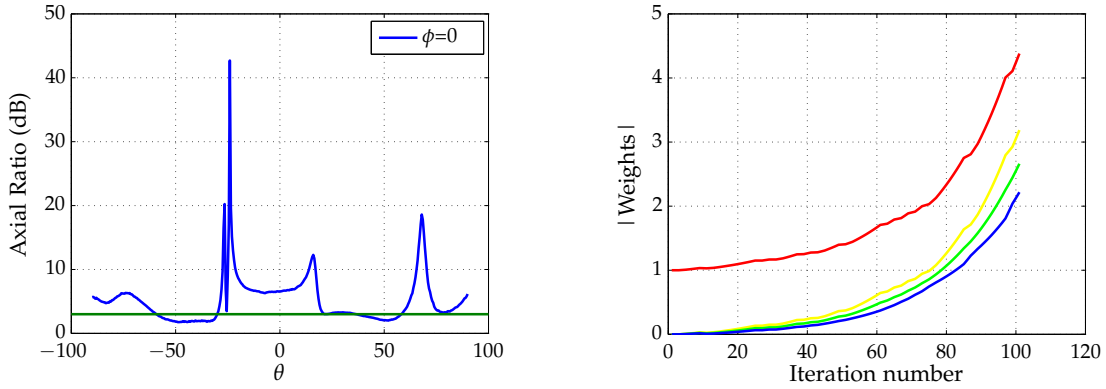

(a) (b)

Figure 7.72: Axial Ratio (a) and weights progression (b) for $\theta_{SOI} = -45^{o}$ and multipath at $\theta = -30^{o}$ and $\theta = -60^{o}$

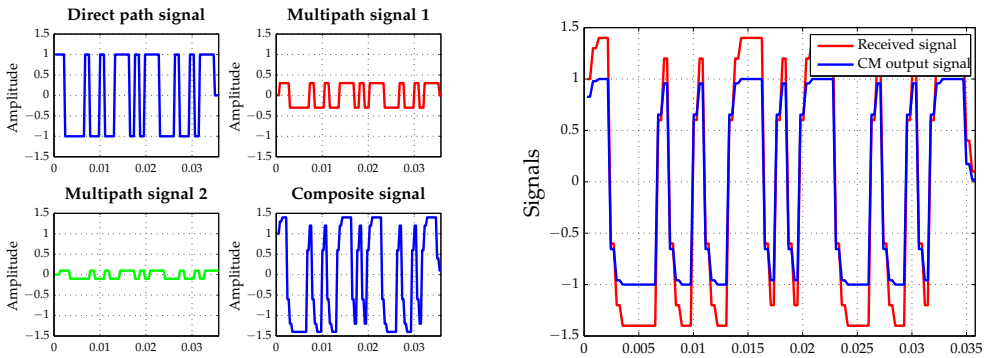

(a) (b)

Figure 7.73: Received composite signal (a) and array output (b) for $\theta_{SOI} = -45^{o}$ and multipath at $\theta = -30^{o}$ and $\theta = -60^{o}$

Measurement for $\theta_{SOI} = -20^{\mathrm{o}}$ with multipath components at $\theta = 30^{\mathrm{o}}$ and $\theta = 45^{\mathrm{o}}$

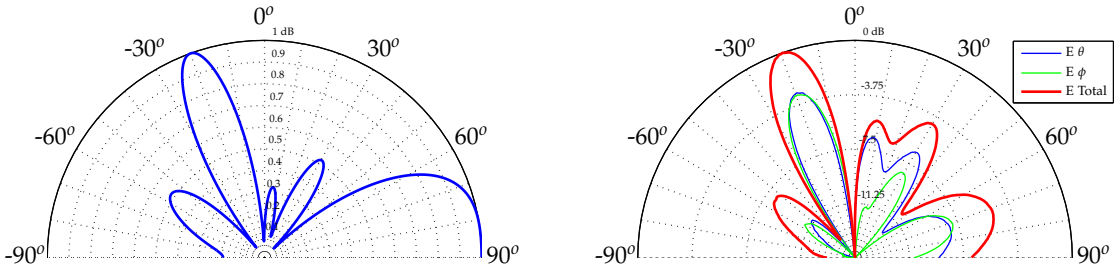

(a) (b)

Figure 7.74: Simulated (a) and measured (b) beam steering for $\theta_{SOI} = -20^{\mathrm{o}}$ and multipath at $\theta = 30^{\mathrm{o}}$ and $\theta = 45^{\mathrm{o}}$

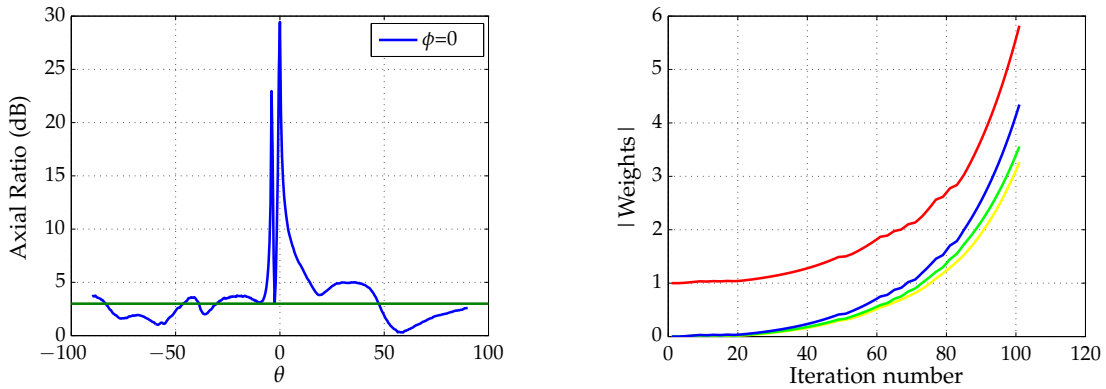

(a) (b)

Figure 7.75: Axial Ratio (a) and weights progression (b) for $\theta_{SOI} = -20^{\mathrm{o}}$ and multipath at $\theta = 30^{\mathrm{o}}$ and $\theta = 45^{\mathrm{o}}$

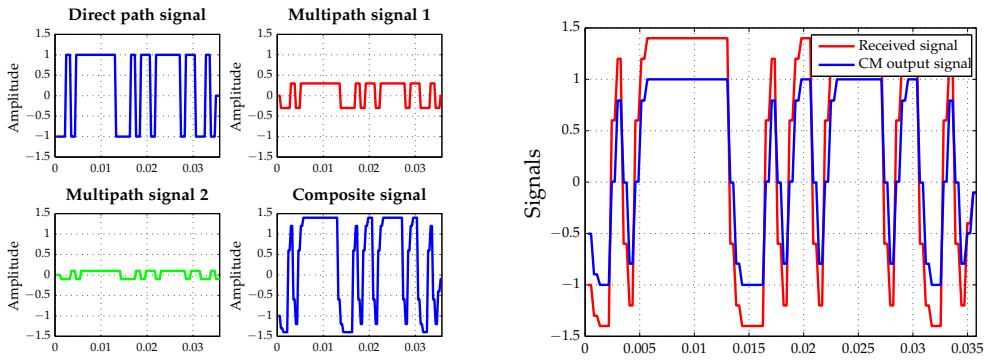

(a) (b)

Figure 7.76: Received composite signal (a) and array output (b) for $\theta_{SOI} = -20^{\text{o}}$ and multipath at $\theta = 30^{\text{o}}$ and $\theta = 45^{\text{o}}$

Measurement for $\theta_{SOI} = 20^{\text{o}}$ with multipath components at $\theta = -30^{\text{o}}$ and $\theta = -45^{\text{o}}$

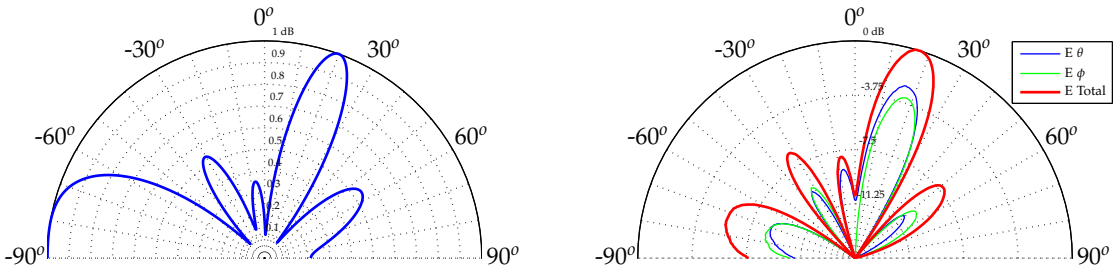

(a) (b)

Figure 7.77: Simulated (a) and measured (b) beam steering for $\theta_{SOI} = 20^{\text{o}}$ and multipath at $\theta = -30^{\text{o}}$ and $\theta = -45^{\text{o}}$

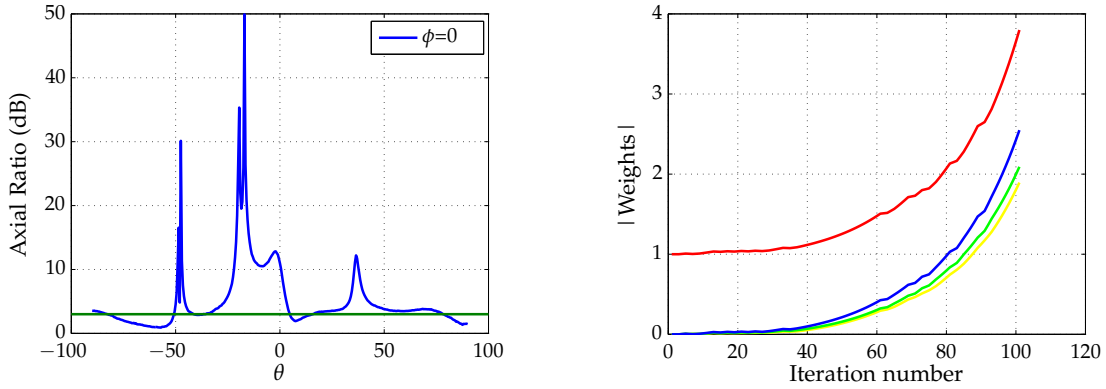

(a) (b)

Figure 7.78: Axial Ratio (a) and weights progression (b) for $\theta_{SOI} = 20^{o}$ and multipath at $\theta = -30^{o}$ and $\theta = -45^{o}$

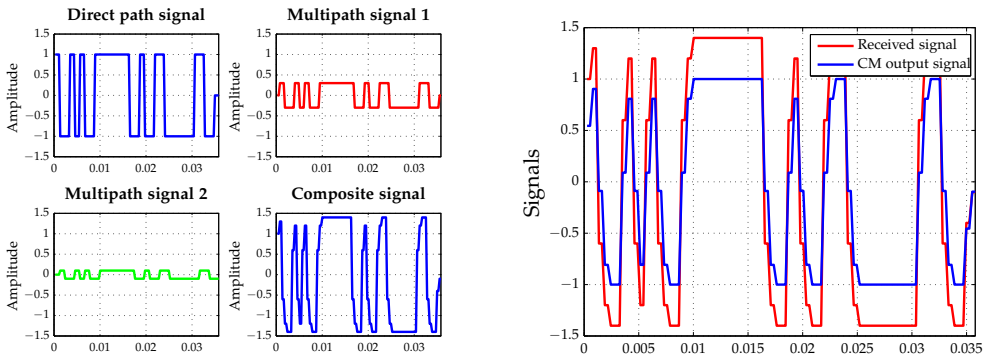

(a) (b)

Figure 7.79: Received composite signal (a) and array output (b) for $\theta_{SOI} = 20^{o}$ and multipath at $\theta = -30^{o}$ and $\theta = -45^{o}$

Least Square Constant Modulus

Measurement for $\theta_{SOI} = 0^{\underline{o}}$

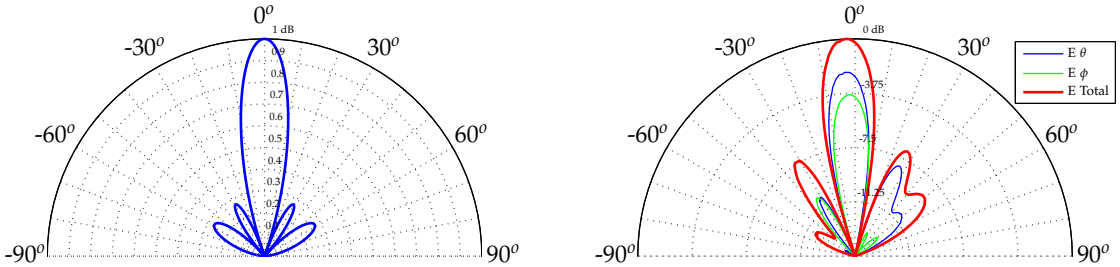

(a) (b)

Figure 7.80: Simulated (a) and measured (b) beam steering for $\theta = 0^{\underline{o}}$

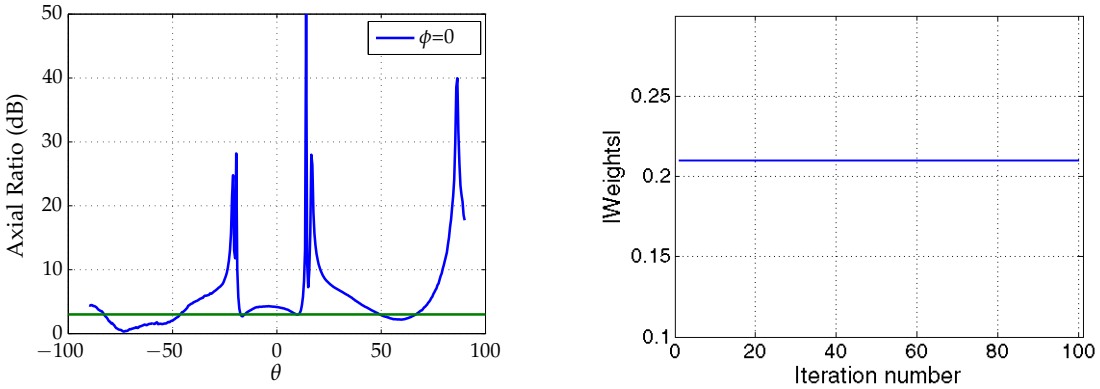

(a) (b)

Figure 7.81: Axial Ratio (a) and weights progression (b) for $\theta_{SOI} = -30^{\underline{o}}$

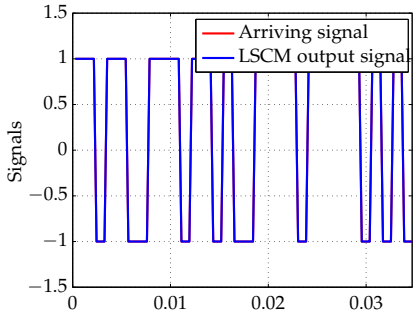

Figure 7.82: $\theta_{SOI} = 0^{\underline{o}}$

Measurement for $\theta_{SOI} = 30^{\mathrm{o}}$

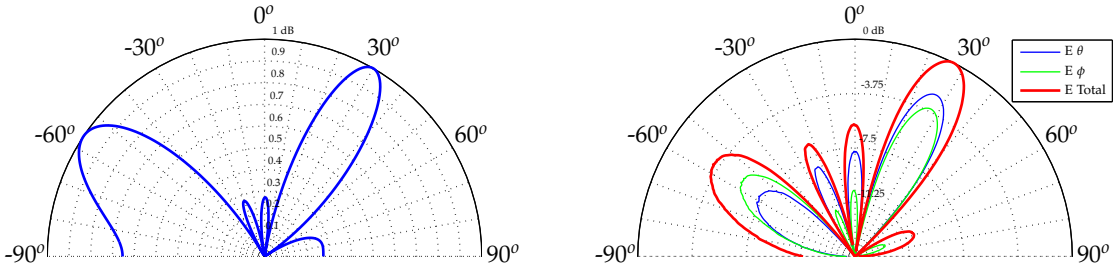

(a) (b)

Figure 7.83: Simulated (a) and measured beam steering for $\theta = 30^{\mathrm{o}}$

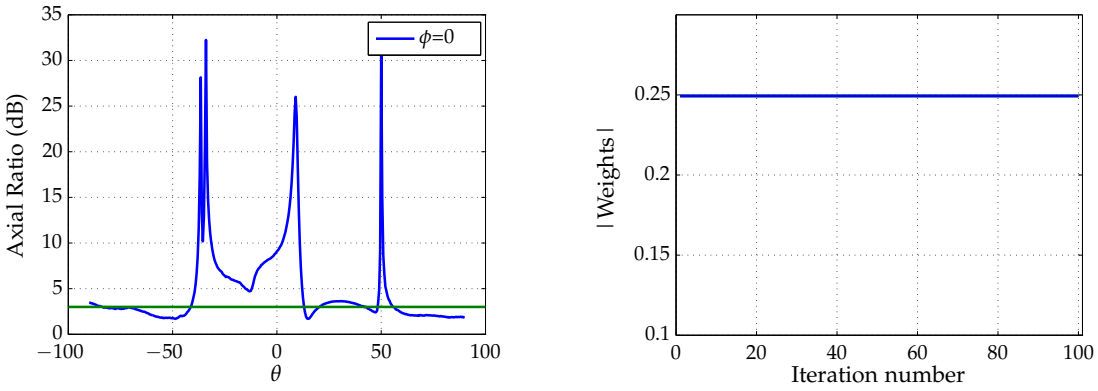

(a) (b)

Figure 7.84: Axial Ratio (a) and weights progression (b) for $\theta_{SOI} = -30^{\mathrm{o}}$

Measurement for $\theta_{SOI} = -30^{o}$

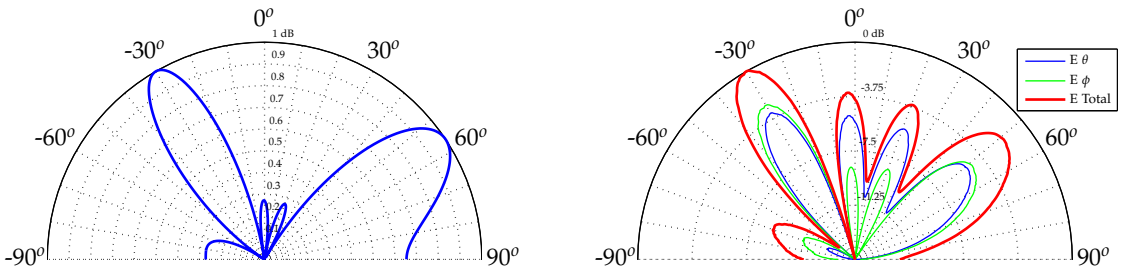

(a) (b)

Figure 7.85: Simulated (a) and measured (b) beam steering for $\theta = -30^{o}$

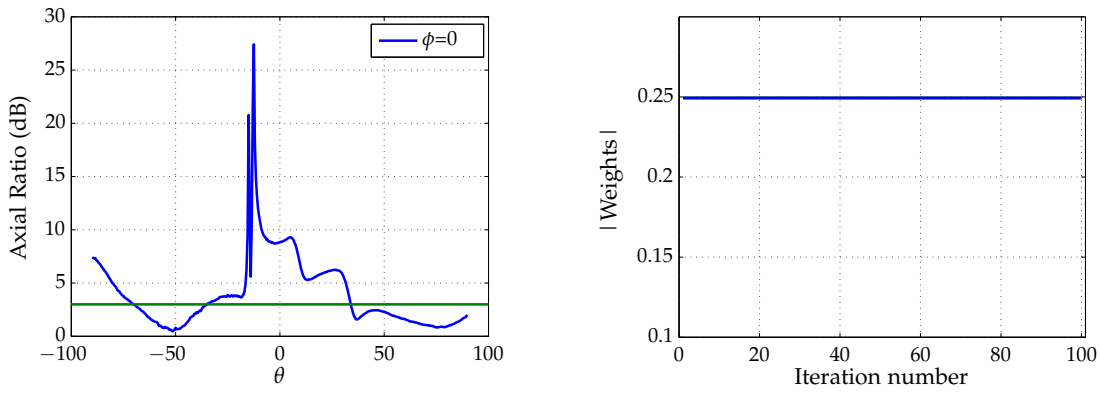

(a) (b)

Figure 7.86: Axial Ratio (a) and weights progression (b) for $\theta_{SOI} = -30^{o}$

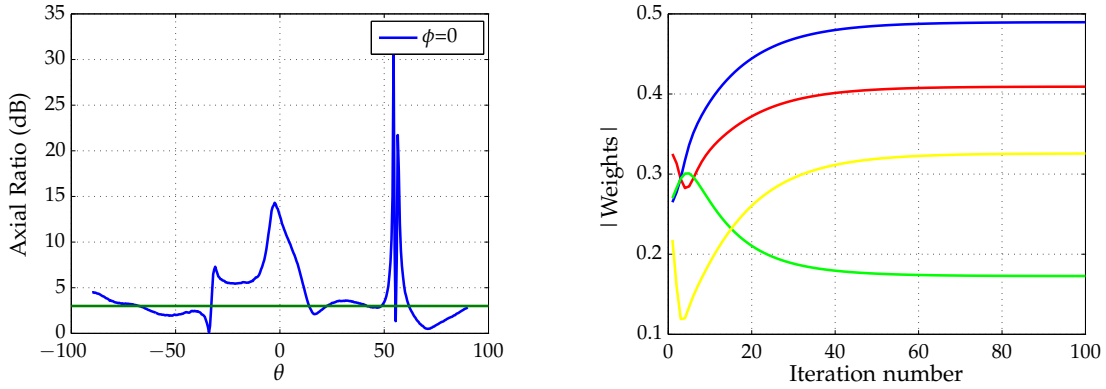

(a) (b)

Figure 7.87: Axial Ratio (a) and weights progression (b) for $\theta_{SOI} = 20^{\text{o}}$ and multipath at $\theta = -30^{\text{o}}$ and $\theta = -45^{\text{o}}$

Measurement for $\theta_{SOI} = 60^{\text{o}}$ with multipath components at $\theta = 45^{\text{o}}$ and $\theta = 80^{\text{o}}$

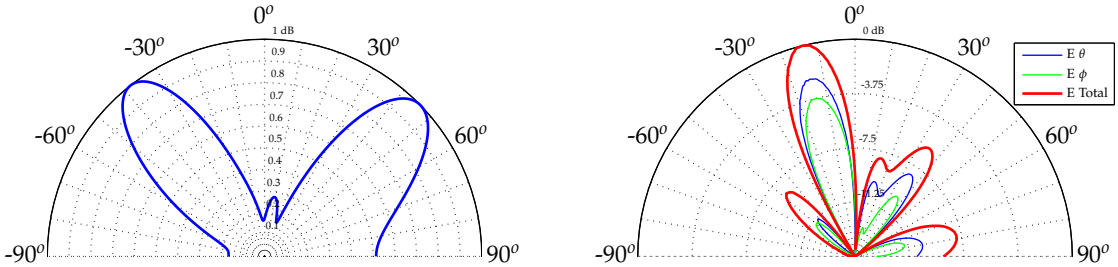

(a) (b)

Figure 7.88: Simulated (a) and measured (b) beam steering for $\theta_{SOI} = 60^{\text{o}}$ and multipath at $\theta = 45^{\text{o}}$ and $\theta = 80^{\text{o}}$

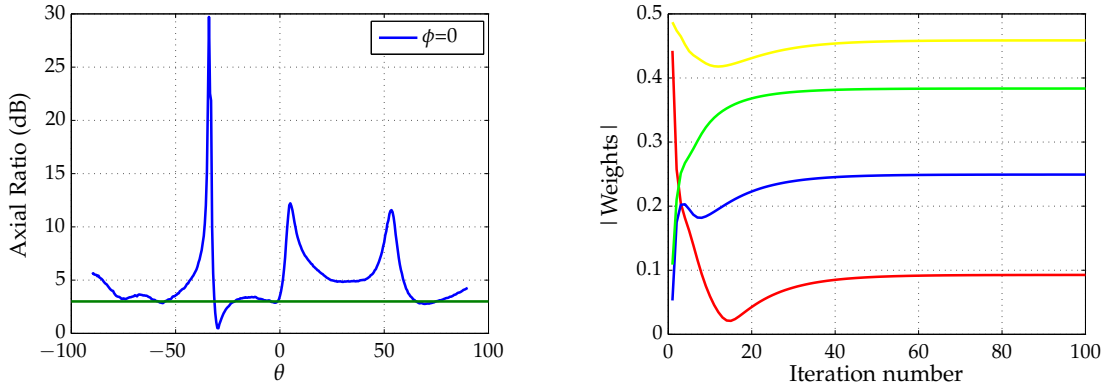

(a) (b)

Figure 7.89: Axial Ratio (a) and weights progression (b) for $\theta_{SOI} = 60^{o}$ and multipath at $\theta = 45^{o}$ and $\theta = 80^{o}$

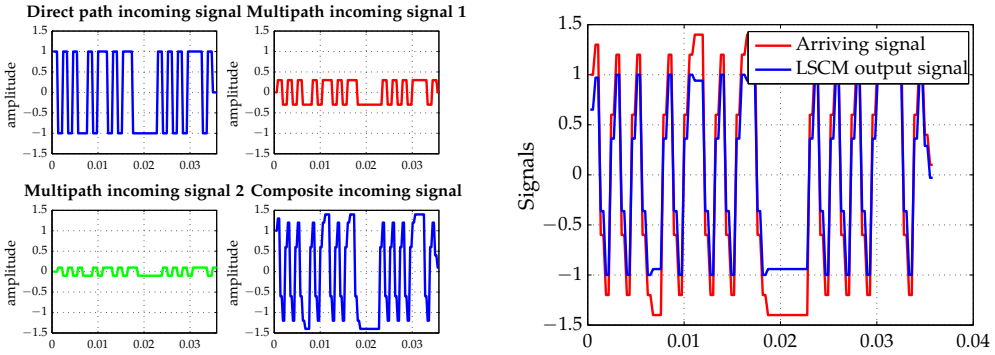

(a) (b)

Figure 7.90: Received composite signal (a) and array output (b) for $\theta_{SOI} = 60^{o}$ and multipath at $\theta = 45^{o}$ and $\theta = 80^{o}$

Measurement for $\theta_{SOI} = -45^{o}$ with multipath components at $\theta = -30^{o}$ and $\theta = -60^{o}$

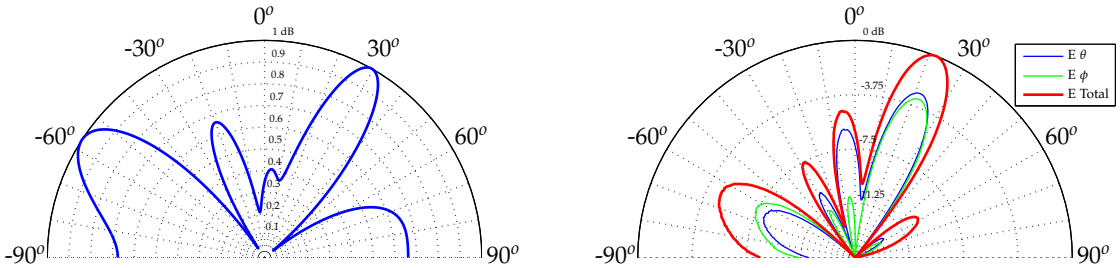

(a) (b)

Figure 7.91: Simulated (a) and measured (b) beam steering for $\theta_{SOI} = -45^{o}$ and multipath at $\theta = -30^{o}$ and $\theta = -60^{o}$

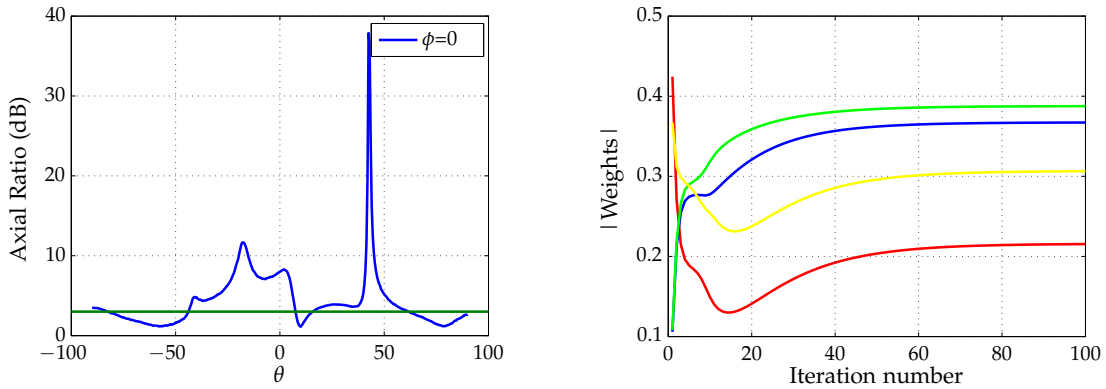

(a) (b)

Figure 7.92: Axial Ratio (a) and weights progression (b) for $\theta_{SOI} = -45^{o}$ and multipath at $\theta = -30^{o}$ and $\theta = -60^{o}$

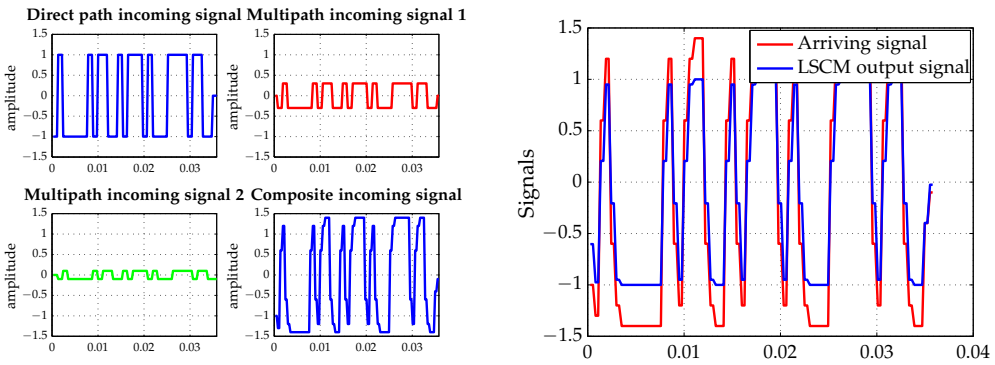

(a) (b)

Figure 7.93: Received composite signal (a) and array output (b) for $\theta_{SOI} = -45^{\text{o}}$ and multipath at $\theta = -30^{\text{o}}$ and $\theta = -60^{\text{o}}$

Measurement for $\theta_{SOI} = -20^{\text{o}}$ with multipath components at $\theta = 30^{\text{o}}$ and $\theta = 45^{\text{o}}$

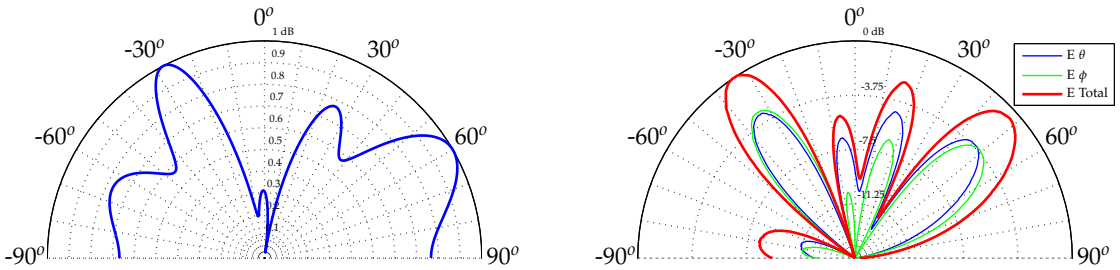

(a) (b)

Figure 7.94: Simulated (a) and measured (b) beam steering for $\theta_{SOI} = -20^{\text{o}}$ and multipath at $\theta = 30^{\text{o}}$ and $\theta = 45^{\text{o}}$

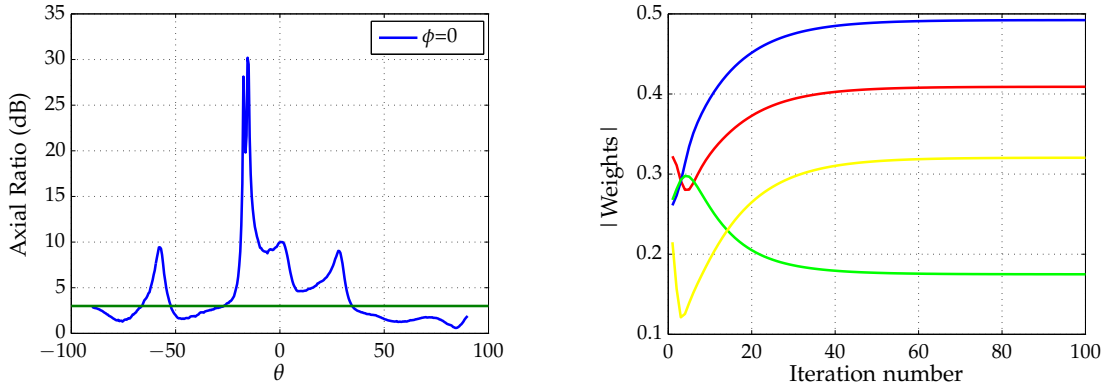

(a) (b)

Figure 7.95: Axial Ratio (a) and weights progression (b) for $\theta_{SOI} = -20^{o}$ and multipath at $\theta = 30^{o}$ and $\theta = 45^{o}$

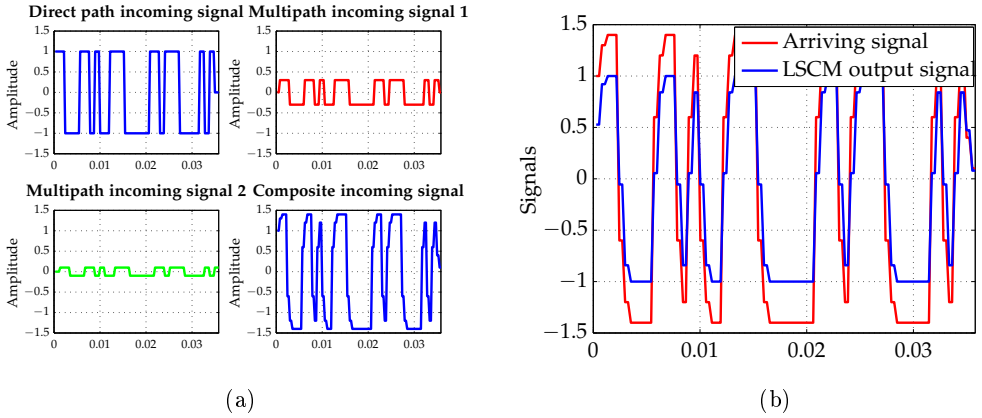

(a) (b)

Figure 7.96: Received composite signal (a) and array output (b) for $\theta_{SOI} = -20^{o}$ and multipath at $\theta = 30^{o}$ and $\theta = 45^{o}$

Measurement for $\theta = 20^{\mathrm{o}}$ with multipath components at $\theta = -30^{\mathrm{o}}$ and $\theta = -45^{\mathrm{o}}$

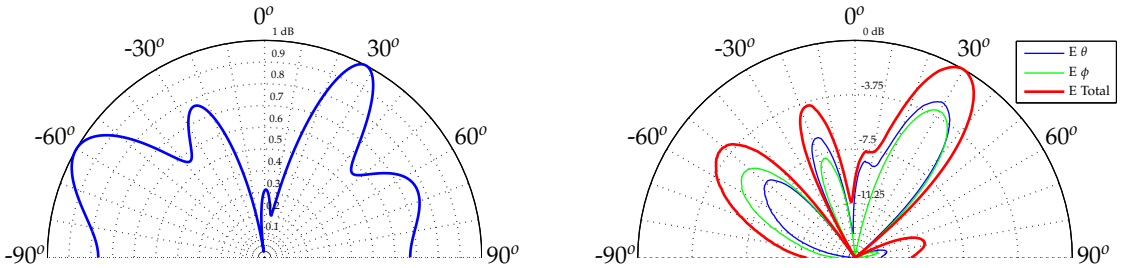

(a) (b)

Figure 7.97: Simulated (a) and measured (b) beam steering for $\theta_{SOI} = 20^{\mathrm{o}}$ and multipath at $\theta = -30^{\mathrm{o}}$ and $\theta = -45^{\mathrm{o}}$

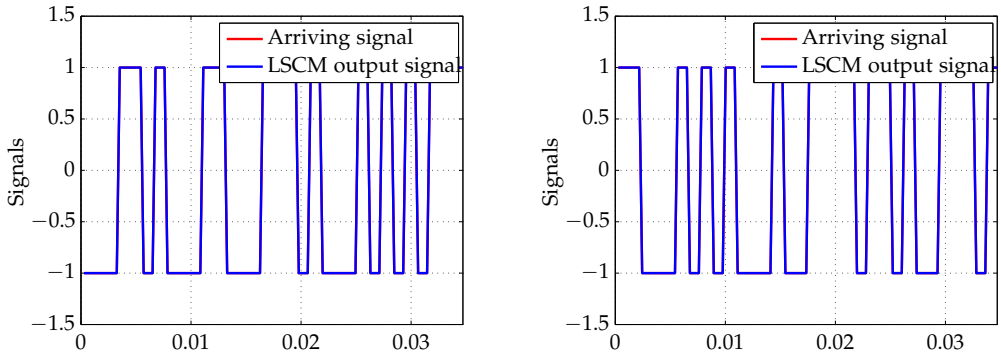

(a) (b)

Figure 7.98: $\theta_{SOI} = 30^{\mathrm{o}}$ (a) and $\theta_{SOI} = -30^{\mathrm{o}}$ (b)

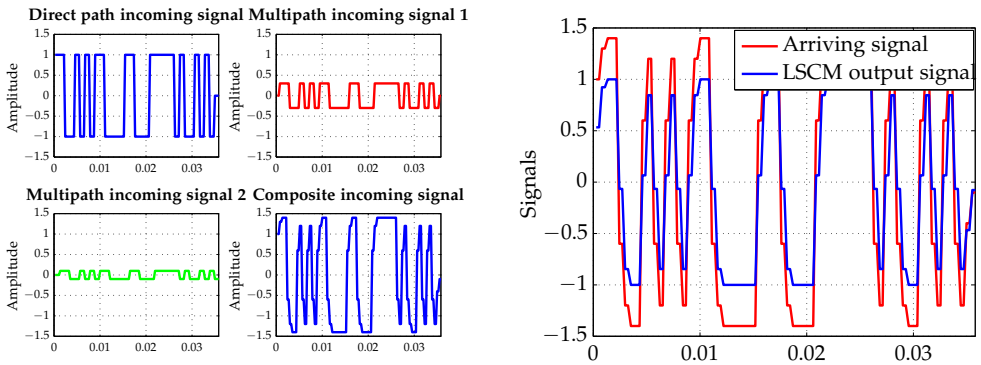

(a) (b)

Figure 7.99: Received composite signal (a) and array output (b) for $\theta_{SOI} = 20^{\text{o}}$ and multipath at $\theta = -30^{\text{o}}$ and $\theta = -45^{\text{o}}$